Forschungszentrum Karlsruhe

Technik und Umwelt

Wissenschaftliche Berichte

FZKA 6314

Spatially-Resolved X-Ray Spectroscopy at CAMD

N. Mölders*), H.O. Moser, V. Saile, P.J. Schilling

Institut für Mikrostrukturtechnik

*) von der Fakultät für Maschinenbau der
Universität Karlsruhe genehmigte Dissertation

Forschungszentrum Karlsruhe GmbH, Karlsruhe

1999

Spatially-Resolved X-Ray Spectroscopy at CAMD

Abstract

The intent to perform spatially-resolved x-ray absorption near-edge structure spectroscopy at the sulfur K-edge on a radiation-sensitive polymer such as poly(hexadiene-1,3 sulfone) (PHS) initiated the design and installation of the Center for Advanced Microstructures and Devices (CAMD) and Argonne National Laboratory (ANL) beamline as well as the microprobe end-station at CAMD, Baton Rouge. Hence, a double crystal monochromator was installed, which provides monochromatic x-rays in the range of ~ 2100 eV to 12000 eV for the x-ray absorption spectroscopy experiment. The main components of the microprobe end-station consist of a kinematic table, an achromatic Kirkpatrick-Baez mirror focusing system, x-ray detectors, and a helium enclosure. The Kirkpatrick-Baez focusing system focuses the incident x-ray beam to a horizontal and vertical focal spot size (σ_{xF}, σ_{zF}) of 18.8 µm x 7.0 µm, respectively. The x-ray detectors and the Kirkpatrick-Baez focusing system are located inside a helium enclosure, which when purged with helium, enables the performance of x-ray absorption near-edge structure (XANES) spectroscopy experiments at lower photon energies (e.g. at the sulfur K-edge XANES spectroscopy at 2472 eV). The helium enclosure is mounted on a kinematic table, which can be vertically translated. This movement compensates for the vertical offset when switching from monochromatic to white beam. For beamline control and data acquisition a new graphical user interface was developed.

The installation of hardware and software at the CAMD/ANL beamline provides the ability to perform spatially-resolved x-ray absorption spectroscopy or micro-spectroscopy in the low energy region between 2100 eV and 5000 eV. Thus, spatially-resolved x-ray absorption near-edge structure (XANES) spectroscopy at the sulfur K-edge was conducted on x-ray exposed poly(hexadiene-1,3 sulfone) to investigate the radiation-induced degradation. Various sulfur functional groups were identified by sulfur K-edge fingerprinting. Moreover, the quantitative analysis of the sulfur K-edge XANES spectra showed that the radiation-induced production of sulfur functional groups can be controlled to some extent by varying the incident exposure spectrum. A surface oxidation effect, evidenced by highly oxidized sulfur species at the poly(hexadiene-1,3 sulfone) surface was observed, indicating the usefulness of sulfur K-edge micro-spectroscopy.

Ortsaufgelöste Röntgenspektroskopie am CAMD

Übersicht

Das Ziel dieser Arbeit ist die ortsaufgelöste Untersuchung eines strahlungsempfindlichen Polymers - Poly(hexadiene-1,3 sulfone) (PHS) - mittels Röntgenabsorptionsnahkanten-spektroskopie an der Schwefel K-Kante. Aus diesem Grund wurden im Rahmen dieser Arbeit eine Strahlführung und ein Experiment zur ortsaufgelösten Röntgenabsorptionsspektroskopie aufgebaut. Hierzu wurde ein Doppelkristallmonochromator, der die Aufnahme von Röntgenabsorptionsspektren in einem Energiebereich von ~ 2100 eV bis 12000 eV ermöglicht, installiert. Die Fokussierung der Röntgenstrahlung wurde durch eine achromatische Spiegeloptik in Kirkpatrick-Baez Anordnung erzielt. Diese erlaubt es, sowohl den weißen als auch den monochromatischen Röntgenstrahl zu fokussieren und erreicht eine horizontale und vertikale Fokusgröße (σ_{xF}, σ_{zF}) von 18.8 µm x 7.0 µm. Um Luftabsorption im Energiebereich von 2000 eV bis 5000 eV zu reduzieren und somit die Aufnahme von Röntgenabsorptionsspektren an der Schwefel K-Kante zu ermöglichen, wurde im Rahmen dieser Arbeit eine Kammer gebaut, die für Messungen im nieder-energetischen Bereich mit Helium geflutet werden kann. In der Heliumkammer befinden sich das Kirkpatrick-Baez System, die Positioniereinheiten zum Verfahren der Probe und die Röntgendetektoren. Der komplette Versuchsaufbau befindet sich auf einem schwingungsgedämpften Positioniertisch, der vertikal verfahren werden kann, um sowohl den weißen als auch den monochromatischen Röntgenstrahl am Experiment nutzen zu können. Für die Datenerfassung und die Steuerung der verschiedenen Positioniereinheiten in der Strahlführung und des Versuchsaufbaus wurde eine graphische Benutzeroberfläche entwickelt.

Die Installation von Hardware und Software an der CAMD/ANL-Strahlführung ermöglichte die erstmalige Durchführung von ortsaufgelöster Röntgenabsorptionsspektroskopie oder Röntgenabsorptionsmikrospektroskopie im Energiebereich von 2100 eV bis 5000 eV. Dies wurde am Beispiel der ortsaufgelösten Schwefel K-Nahkanten-Röntgenabsorptions-mikrospektroskopie (S K-Kante micro-XANES) an belichtetem Poly(hexadiene-1,3 sulfone) gezeigt. Weiterhin wurde die qualitative und quantitative strahlungsinduzierte Entstehung von funktionellen Schwefelgruppen in Poly(hexadiene-1,3 sulfone) in Abhängigkeit von der deponierten Dosis und dem Belichtungsspektrum untersucht. Die Ergebnisse zeigen u.a., daß verschiedene funktionelle Schwefelgruppen anhand von Schwefel K-Kante XANES „fingerprinting" identifiziert werden können. Die quantitative Analyse der Schwefel K-Kante XANES Spektren zeigt, daß die strahlungsinduzierte Produktion von funktionellen Schwefelgruppen durch die Wahl des Belichtungsspektrums gesteuert werden kann. Zusätzlich wurde eine Oxidation der Polymeroberfläche beobachtet, die aus der strahlungsinduzierten Entstehung von hoch-oxidiertem Schwefel in Poly(hexadiene-1,3 sulfone) resultiert. Dieser Effekt konnte mittels Schwefel K-Kante micro-XANES Spektroskopie beobachtet werden und demonstriert somit den Nutzen von Schwefel K-Kante micro-XANES Spektroskopie.

Table of Contents

1 Introduction

The lithography process as it is used in manufacturing semiconductor as well as micro-machining devices relies heavily on transferring a mask pattern into a radiation-sensitive polymer system or resist. There are two groups of radiation-sensitive resists, positive and negative , which are classified according to their chemical response to the incident radiation. In the case of a negative resist, the polymer starts to cross-link upon exposure, thereby increasing the molecular weight and becoming insoluble for the developer. On the other hand, in a positive resist, main polymer chain scission is the predominant effect of radiation energy deposited. Hence, the sensitivity or G(s) value[1] of a resist is very important for the efficiency of the lithography process.

Extensive fundamental research has been conducted on PMMA, a positive resist, to characterize the fragmentation and sensitivity caused by the exposure process [1, 2]. However, PMMA has a moderate chain scission efficiency G(s) and therefore, various efforts have been undertaken to create new x-ray resists [1, 3, 4]. Poly(hexadiene-1,3)sulfone, or PHS, has been proposed based on its high sensitivity, good film-forming capabilities and high glass transition temperature (T_g) as a potential x-ray resist for applications in micro-machining [5].

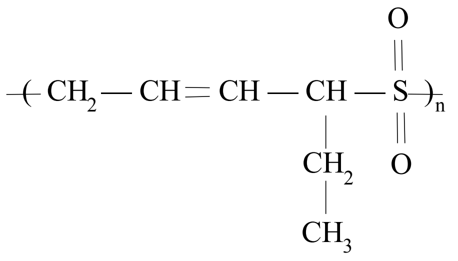

$$-\!\left(CH_2 - CH = CH - \underset{\substack{|\\ CH_2\\ |\\ CH_3}}{CH} - \overset{\substack{O\\ \|}}{\underset{\substack{\|\\ O}}{S}} \right)_n$$

Figure 1. The structure of poly(hexadiene-1,3 sulfone) (PHS).

In PHS, sulfur is the element with the highest atomic number. It will absorb the predominant amount of dose deposited provided the energy of incident photons exceeds ~ 2500 eV. Hence, the sulfur cites in PHS are of particular interest in the exposure process. To study the change of the local sulfur environment in PHS upon exposure, x-ray absorption near-edge structure (XANES) at the sulfur K absorption edge has been applied. XANES has proven itself to be a very powerful tool for the non-destructive and quantitative analysis of the structural and chemical surrounding of the absorbing sulfur atom [6-13]. An initial surface sensitive study of irradiated PHS via S K-edge XANES revealed the strong changes in sulfur functional groups upon exposure dosage [14]. These results initiated more detailed studies of the correlation between radiation-induced degradation of PHS and the dose-depth deposition.

During this work, it is shown that upon radiation exposure, the sulfur functional groups of sulfide, sulfoxide, sulfone, and sulfonate are generated in PHS. The production of these functional groups can be controlled to some extent by varying the incident exposure spectrum. In particular, the radiation-induced production of sulfide can be associated with the exposure spectrum. Furthermore, it is established that the radiation-induced production of sulfonate is limited to the surface region of PHS and can be related to a surface oxidation effect. To perform these experiments, spatially-resolved x-ray absorption spectroscopy or

---

[1] Main scission efficiency, G(s), gives the number of main scissions per 100eV of energy deposited.

micro-spectroscopy at the S K-edge (2472 eV) was applied and a beamline with a microprobe end-station had to be designed.

Based on the advent of new synchrotron radiation sources with higher brilliance and growing interest in non-destructive microscopy, the field of x-ray microscopy has lately developed considerably. There are scanning x-ray microprobes working in the soft and hard x-ray region, which employ various focusing techniques and achieving focal spot sizes smaller than 1 µm [15-18]. Imaging x-ray microscopy, on the other hand, generally uses Fresnel-Zone plates, obtaining a resolution of tens of nanometer [19].

Two factors contributed to the design and installation of a microprobe end-station, which was built to conduct micro-spectroscopy at lower photon energies, e.g. micro-XANES at the S K-edge. The first factor is that the spectral intensity distribution of the CAMD storage is optimized for the energy region of 1000 eV to 4000 eV ($E_c \sim 1660$ eV). Secondly, until now none of the above focusing systems operate in this spectral region. As a result, the CAMD/ANL beamline with a double crystal monochromator was commissioned and the microprobe end-station with an achromatic Kirkpatrick-Baez mirror focusing system and a helium enclosure were installed. To our knowledge, this is the first reported work on micro-XANES in the energy region of 2000 eV to 4000 eV, showing the example of sulfur K-edge (2472 eV) micro-XANES on a potential x-ray resist poly(hexadiene-1,3 sulfone).

Chapter 2 presents a general introduction to x-ray absorption spectroscopy (XAS), followed by a brief description of x-ray absorption fine structure (XAFS). X-ray absorption near-edge structure spectroscopy (XANES) is qualitatively depicted on the example of sulfur K-edge XANES spectroscopy. A general description of the experimental requirements for XAS is shown in the last part of this chapter.

In chapter 3 the CAMD/ANL beamline and the Brazilian double crystal monochromator from the Laboratório Nacional de Luz Síncrotron (LNLS) are introduced. In particular, the energy resolution as well as some mechanical modifications to the LNLS double crystal monochromator are discussed, which are very important to perform x-ray absorption spectroscopy in the energy region of 2000 eV to 4000 eV.

Chapter 4 depicts the microprobe end-station with the kinematic table, the scanning stage, the detectors and the helium enclosure. The hardware set-up for the data acquisition as well as a brief introduction to the graphical user interface, which controls the experiment, can also be found in this chapter.

Chapter 5 deals with the centerpiece of the microprobe end-station, the Kirkpatrick-Baez mirror focusing system. It discusses important performance parameters such as the focusing properties of the mirror, which are afterwards illustrated by ray-tracing calculations. The primary experimental results documenting the good performance of the focusing system, presenting focal spot sizes and photon flux at the sample are also shown.

Chapter 6 describes the experimental work such as the co-polymerization of poly(hexadiene-1,3 sulfone) (PHS), its thin film preparation by spinning and lift off technique, and the exposure procedure. Furthermore, a description of the data collection in the microprobe end-station is shown.

In chapter 7, the main results on the sulfur K-edge micro-XANES are described and discussed. It is shown that the effect of exposure can be controlled to some extent by varying the spectrum of the incident radiation. In particular, formation of sulfide, indicative of main scission, is more frequent when the radiation spectrum is closer to the sulfur K-edge. The summary of the results is presented in chapter 8.

2 X-ray absorption spectroscopy (XAS)

This chapter will give a general introduction to x-ray absorption spectroscopy (XAS), which is a powerful, non-destructive, element-specific method to probe the local structure around the specific absorbing element. XAS yields information such as bond distance, number, and type of nearest neighbors, while being applicable to most elements in the periodic table in various phases (crystalline or amorphous solids, liquids and gases). In addition, electronic structure and bond geometry can also be extracted from the spectra. With the advent of high brilliance synchrotron radiation sources combined with x-ray focusing optics, it is now possible to create small focused x-ray beams (< 20 μm) with sufficient intensity to get the previous information in a spatially-resolved manner. This technique is usually referred to as micro-spectroscopy.

Firstly, the energy dependency of the linear absorption coefficient μ is shown. This is followed by the description of the x-ray absorption fine structure in section 2.2. A qualitative discussion of the x-ray absorption near-edge structure (XANES) is shown in section 2.3, with specific reference to the identification of sulfur functional groups using sulfur K-edge XANES. The experimental requirements to perform XAS are outlined in section 2.4.

2.1 The energy dependency of the linear absorption coefficient μ

When a collimated beam of monochromatic x-rays passes through matter, it loses some of its initial intensity due to the fact that it interacts with matter. The loss in monochromatic intensity can be described as follows

$$I = I_0 \cdot e^{-\mu \cdot d_t}. \qquad (1)$$

This equation is known as Lambert-Beer's law, where I_0 and I are the initial and transmitted intensity of the monochromatic beam, d_t is the thickness of the material and μ is the linear absorption coefficient, which is a function of the photon energy.

As the photon energy E_{Photon} of the incident x-ray beam is gradually increased, the linear absorption coefficient μ generally decreases. This behavior changes abruptly when certain critical energies are reached, at which the linear absorption coefficient μ increases. These discontinuities in the linear absorption coefficient μ arise when the photon energy is high enough to eject core electrons of the next deeper shell. They are called the absorption edges. Figure 2 shows the linear absorption coefficient μ for sulfur in the energy region between 100 eV and 20000 eV. Here the absorption edges of K and L shells can be seen at the energies of 2472 eV and 163 eV, respectively.

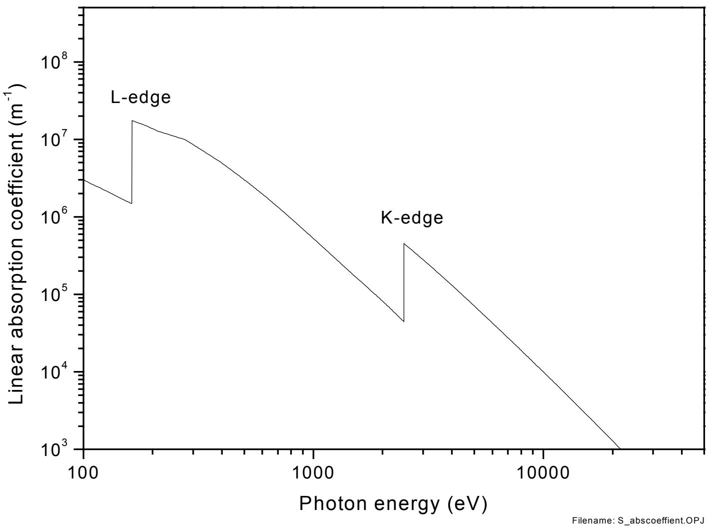

Figure 2. The linear absorption coefficient μ of sulfur in the energy range of 100 eV to 20000 eV.

It can be observed in the double logarithmic scale of Figure 2 that the linear absorption coefficient of sulfur is approximately proportional to E_{Photon}^{-3}. The function can be fitted by the empirical Victoreen formula [20, 21] over a large energy range in terms of the wavelength λ as

$$\frac{\mu}{\rho_i}\left(\frac{cm^2}{g}\right) = C(Z)\cdot\lambda(\text{Å})^3 - D(Z)\cdot\lambda(\text{Å})^4 + \sigma_e\cdot N_A\cdot\frac{Z}{A_i}. \qquad (2)$$

In this energy region the values of D(Z=16) and σ_e are very small compared to C(Z=16) (for the wavelength λ in Angstroms, $\mathrm{C(16)} = 29.49\,\mathrm{cm}^2/(\text{Å}^3\cdot\mathrm{g})$, $\mathrm{D(16)} = 2.538\,cm^2/(\text{Å}^4\cdot\mathrm{g})$, and $\sigma_e\cdot N_A \approx 0.4\ \mathrm{cm}^2$ [20]), leading to the cubic relationship mentioned above. C(Z) and D(Z) are functions of the atomic number Z and the atomic weight A_i, and change abruptly at the absorption edges. N_A is the Avogadro number, σ_e is the Klein-Nishina scattering coefficient, and ρ_i and A_i are the density and the atomic weight of the element i.

2.2 The x-ray absorption fine structure (XAFS)

In the vicinity of the absorption edge of an element, oscillations in the linear absorption coefficient μ are observed, which are called the x-ray absorption fine structure (XAFS). The energy region of the XAFS is subdivided into the x-ray absorption near-edge structure (XANES) and the extended x-ray absorption fine structure (EXAFS) as shown in Figure 3.

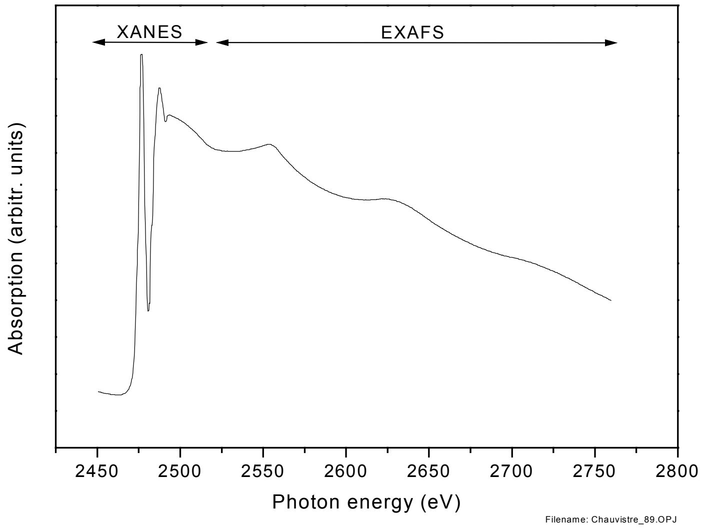

Figure 3. S K-edge EXAFS spectrum of C_2S_2 taken from Chauvistré [22] indicating the EXAFS as well as the XANES region.

XANES is historically known as Kossel structure [23] and is caused by the production of low-energy photoelectrons, which then undergo multiple scattering. Conversely, EXAFS, or Kronig structure [24], can be explained in terms of single scattering of high-energy photoelectrons from neighboring atoms (refer to Figure 4).

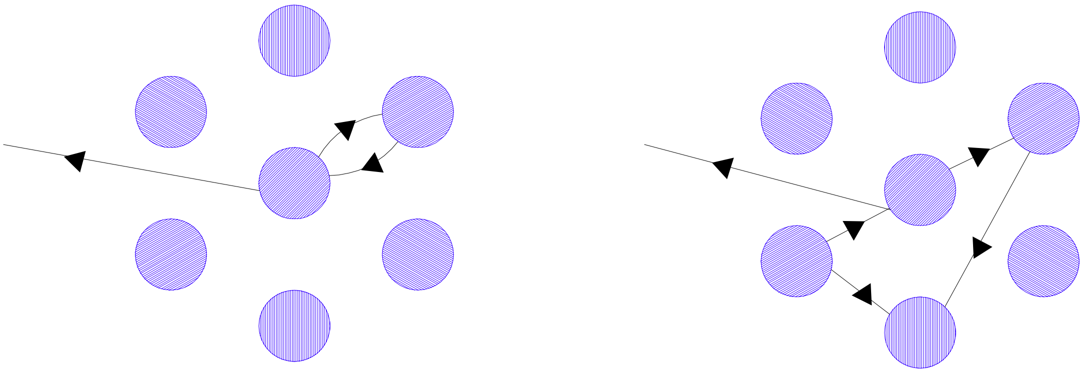

Figure 4. Single scattering process (left) in the EXAFS region and the multiple-scattering (right) process in the XANES region.

As a rule of thumb, one usually expects the XANES to cover a range up to 50 eV beyond the absorption edge. A more precise theoretical energy limit can be given in terms of the photoelectron wavelength λ_e. The single scattering theory of EXAFS is not valid when the photoelectron wavelength λ_e is larger than the interatomic distance d_i. The expected low energy limit of multiple scattering may be defined as

$$E_{Photon}(eV) < \frac{151(\text{Å} \cdot \text{eV})}{d(\text{Å})_i^2} - V_F(eV), \tag{3}$$

where V_F represents the interatomic potential at the Fermi level [25].

The extended x-ray absorption fine structure occurs because of scattering of the photoelectron with the nearest neighboring atoms, leading to constructive or destructive interference (as shown in Figure 5). This causes oscillations in the linear absorption coefficient μ.

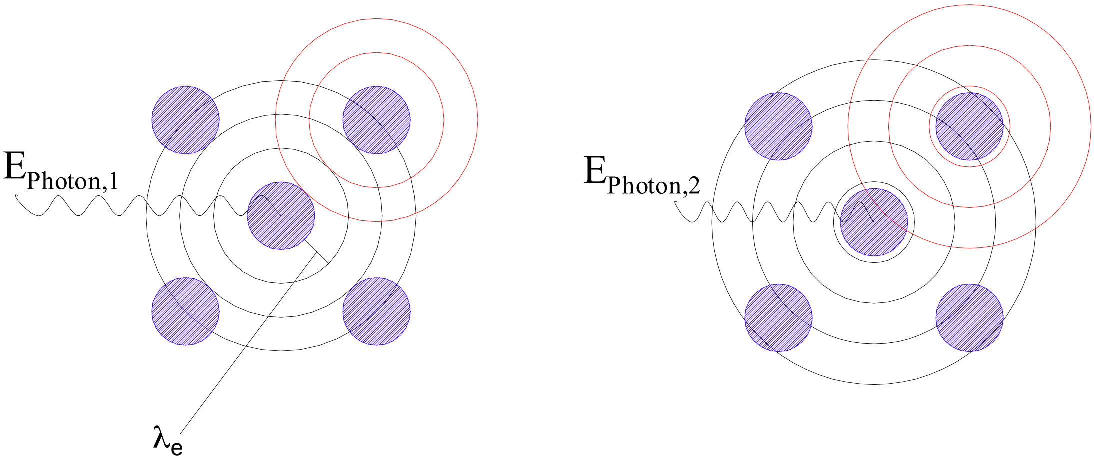

Figure 5. Schematic of the outgoing electron wave with wavelength λ_e and the backscattered electron wave from the nearest neighbors for 2 photon energies. This results in constructive (left) and destructive interference (right), which is reflected in the modulation of the linear absorption coefficient μ.

The successful development of the one-electron, single scattering, short-range order theory due to Sayers, Stern, and Lytle, made EXAFS a very powerful analytical tool [26-28]. The "standard" EXAFS equation can be given as

$$\chi(k) = \sum_j N_j S_i(k) F_j(k) e^{-M \cdot k^2} e^{\frac{-2r_j}{\lambda_j(k)}} \frac{\sin(2kr_j + \Phi_{ij}(k))}{kr_j^2}, \tag{4}$$

in which N_j is the number of atoms in the *j*th shell, $S_i(k)$ is the amplitude reduction factor due to many-body effects at the central atom, $F_j(k)$ is the backscattering amplitude, $e^{-M \cdot k^2}$ is the Debye-Waller factor, r_j is the distance to the *j*th shell, λ_j is the electron mean free path and Φ_{ij} is the phase shift. The data analysis has been the topic of many review articles, in which a detailed description of the data analysis can be found [29-31].

2.3 Qualitative description of the x-ray absorption near-edge structure (XANES)

Figure 6 presents the sulfur K-edge XANES spectrum of poly(hexadiene-1,3 sulfone) in the energy region of 2460 eV to 2520 eV. The spectrum can be divided in the pre-edge region and the post-edge region above the absorption edge.

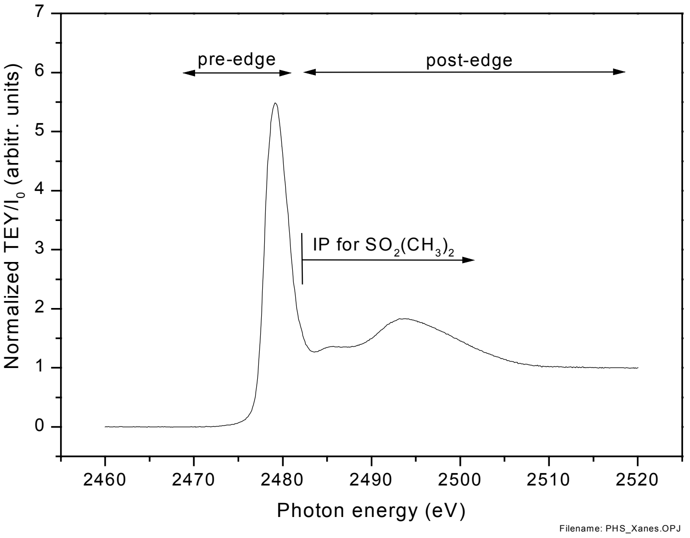

Figure 6. S K-edge XANES spectrum of unexposed poly(hexadiene-1,3 sulfone) depicting the pre-edge and post-edge region. The ionization potential (IP) of $SO_2(CH_3)_2$ at 2482.5 eV was taken from Hitchcock et al. [32] to give an estimate of the IP of PHS.

The features appearing in the pre-edge region result from transitions from a core level to the lowest energy, unoccupied or partially unoccupied level, which have to follow the dipole selection rules. These transitions are considered to be localized and involve atomic or molecular orbital energy levels. The intensities of the pre-edge features, indicating the transition probabilities, are in part determined by the symmetry of the ligands surrounding the absorber. The “white line” is a strong well-resolved feature that is situated in the case of sulfur 6 eV to 8 eV below the continuum threshold.

The post-edge region extends from a few eV to ~ 50 eV beyond the edge. Here, resonances can be found that are due to multiple scattering of the excited low energy photoelectron from the surrounding neighbors. This process often extends beyond the first neighbor shell of ligands and therefore, the transition is not localized [29].

Since the excitation process in XANES involves multi-electron and multiple-scattering effects, the data analysis is not as straightforward as in the XAFS data analysis, but is instead rather difficult. There are two main approaches to the XANES analysis, ab-initio molecular orbital theory and multiple-scattering theory. The molecular orbital theory in condensed systems employs one-electron approximations based on Hartree, Hartree-Fock and local density approximations, applied to molecular systems like a finite cluster of atoms surrounding the absorbing atom [33]. On the other hand the multiple-scattering theory tries to solve the one-electron Schrödinger equation of the finite cluster [34].

For analytical purposes, S K-edge XANES spectroscopy has been used extensively to identify various forms of sulfur in heavy petroleum and coal [10-12, 35-37]. Moreover, S K-edge XANES spectroscopy using “fingerprinting” found further applications in fields of research such as in charging and discharging of disulfide redox cathodes [38, 39] and in sulfur determination in biological systems in vivo [8]. For sulfur, the “fingerprinting” technique is based on the fact that when a valence electron is removed from an atom, screening of core electrons provided by the valence electrons is reduced, and the core levels become more tightly bound. Hence, it requires more initial photon energy to remove the core electron from its energy level, resulting in an energy shift of the XANES spectrum. This shift is known as the chemical shift, which can be correlated to the difference in oxidation state for an element [29]. This fact is detailed in Figure 7 which shows the S K-edge XANES spectra for methionine sulfide and poly(sodium 4-styrenesulfonate). In this specific case, the energy shift between the sulfide and sulfonate functional groups, in the formal oxidation states of –2 and +6, respectively is ~ 9 eV.

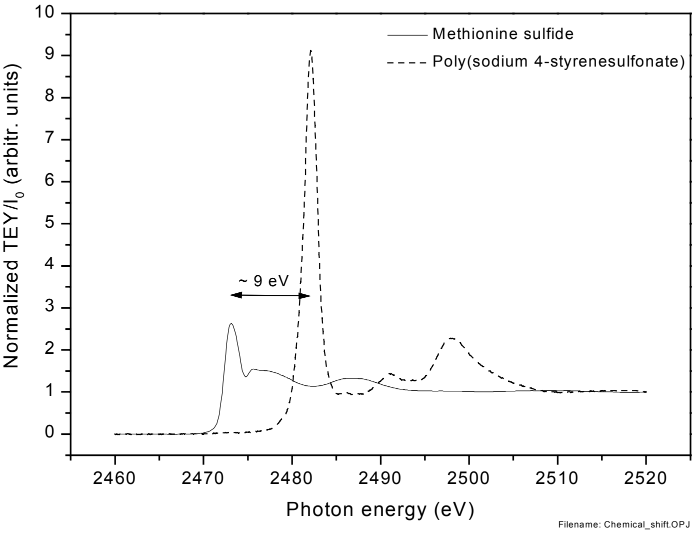

Figure 7. S K-edge XANES spectra of methionine sulfide and poly(sodium 4-styrenesulfonate). The chemical shift between the sulfur functional groups of sulfide (-2) and sulfonate (+6) is ~ 9 eV.

Furthermore, quantitative information on the sulfur functional groups being present in a sample can be obtained by performing nonlinear least squares fits using S K-edge XANES spectra of reference compounds. Waldo et al. developed this technique for the quantification of different sulfur functional groups in heavy petroleum [10]. Since then, it has been applied similarly for the quantification of sulfur functional groups in heavy petroleum and coal [11, 36], marine sediments [40], and humic substances [13].

2.4 Experimental requirements for x-ray absorption spectroscopy (XAS)

X-ray absorption spectroscopy (XAS) requires a continuous and intense x-ray source covering a broad range of photon energies, a tunable monochromator with which to select the incident photon energy, and appropriate x-ray detectors, which are typically ionization chambers or photo-diodes. A schematic of the spatially-resolved x-ray absorption spectroscopy set-up in transmission mode at the Center for Advanced Microstructures and Device (CAMD) at Louisiana State University is depicted in Figure 8.

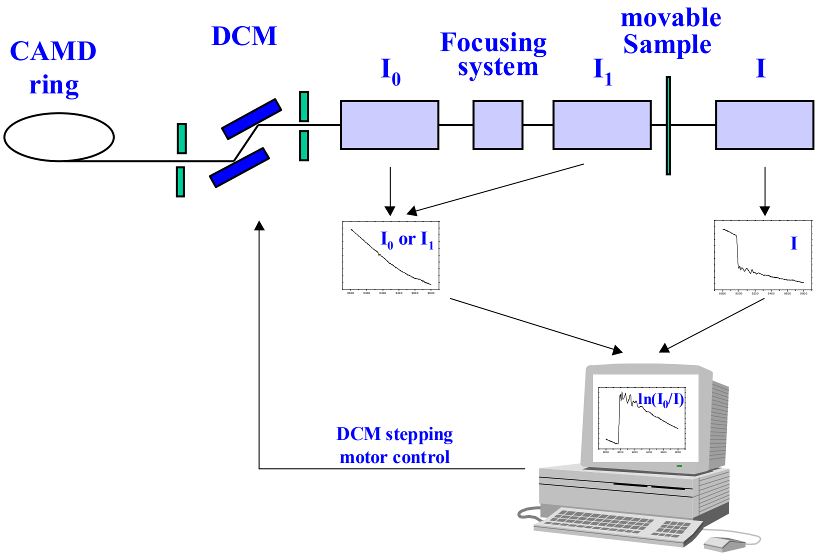

Figure 8. Schematic of the spatially-resolved x-ray absorption spectroscopy set-up in transmission mode at the Center for Advanced Microstructures and Device (CAMD) at Louisiana State University.

A continuous energy spectrum of x-rays can either be obtained by the bremsstrahlung output of a rotation anode source or from a storage ring emitting synchrotron radiation. Characteristics of synchrotron radiation such as high intensity and high collimation in the forward direction of the x-ray beam favor the choice of a storage ring as the source of x-rays for spatially-resolved x-ray absorption spectroscopy experiments. Synchrotron radiation is emitted as the major loss mechanism from charged particles such as electrons or positrons in a circular motion at relativistic energies. The properties of synchrotron radiation have been measured by Elder et al. [41]. The important characteristics of synchrotron radiation for x-ray absorption spectroscopy may be summarized as follows and were previously reported by Koch et al [42]:

- High intensity in a wide spectral range permitting the use of narrow band pass monochromators and hence achieving high energy resolution x-ray absorption spectroscopy.
- High degree of collimation enabling spatially-resolved x-ray absorption spectroscopy experiments.
- Well-defined polarization, facilitating directional x-ray absorption spectroscopy studies of single crystals.
- Pulsed time structure of radiation emission enabling time resolved x-ray absorption spectroscopy experiments.

The performance parameters of the CAMD storage ring are described by Stockbauer et al. [43]. The monochromatization of the polychromatic (white) incident x-rays emitted by the CAMD bending magnet in Figure 8 is performed by a tunable double crystal monochromator (DCM). A computer with interfaces controls the angle of the double crystal monochromator, records the intensities measured in the ionization chambers I and I_0, and plots and stores the absorption $\mu \cdot d_t = \ln(I_0/I)$. A Kirkpatrick-Baez focusing system, as indicated in Figure 8, combined with a sample on movable translation stage enables spatially-resolved x-ray absorption spectroscopy studies. A detailed description of the double crystal monochromator, the microprobe end-station including the x-ray detectors and the translation stages, and the Kirkpatrick-Baez focusing system are presented hereafter.

3 The beamline

In order to be able to perform spatially-resolved x-ray absorption spectroscopy (XAS), it is necessary to provide monochromatic radiation in the microprobe end-station. Hence, the Laboratório Nacional de Luz Síncrotron (LNLS) double crystal monochromator was installed in the ANL/CAMD beamline. Due to its mechanical design and the ability to control its hardware, white radiation can also be supplied to the microprobe end-station. At first, the beamline layout and vacuum system will be presented in section 3.1, followed by the double crystal monochromators' vacuum system and the vacuum control and interlock system in section 3.2. Section 3.3 presents a brief introduction to x-ray monochromators and discusses in detail the energy resolution and the photon flux of the beamline and the LNLS double crystal monochromator. The modifications to the mechanical design of LNLS double crystal monochromator, which are favorable for experimental work in the low photon energy region, are also presented in section 3.3.

3.1 The beamline layout from the bending magnet to the beryllium window

Figure 9 presents the top and the side view of the mechanical layout of the ANL/CAMD microprobe beamline at CAMD. The ANL/CAMD beamline is installed at bending magnet 5 port A on the CAMD storage ring. The white x-ray beam leaves the dipole magnet vacuum chamber (DMC) of the storage ring, passes though a water-cooled copper aperture (AP), the photon shutter (PS), a gate valve (GV), the fast-closing valve (FV) and the Bremsstrahlung shutter (BS). The ultra-high vacuum (UHV) system of the storage ring at 10^{-10} torr extends through the shield wall (SH) and the beam travels through a 125 ∝m thick beryllium window (BEW), which is located 6.7 m from the source point. The beryllium window separates the UHV of the storage ring from the vacuum of beamline at 10^{-3} torr in the monochromator chamber. The maximum horizontal acceptance of the beamline is defined by the water-cooled copper aperture and is 2 mrad.

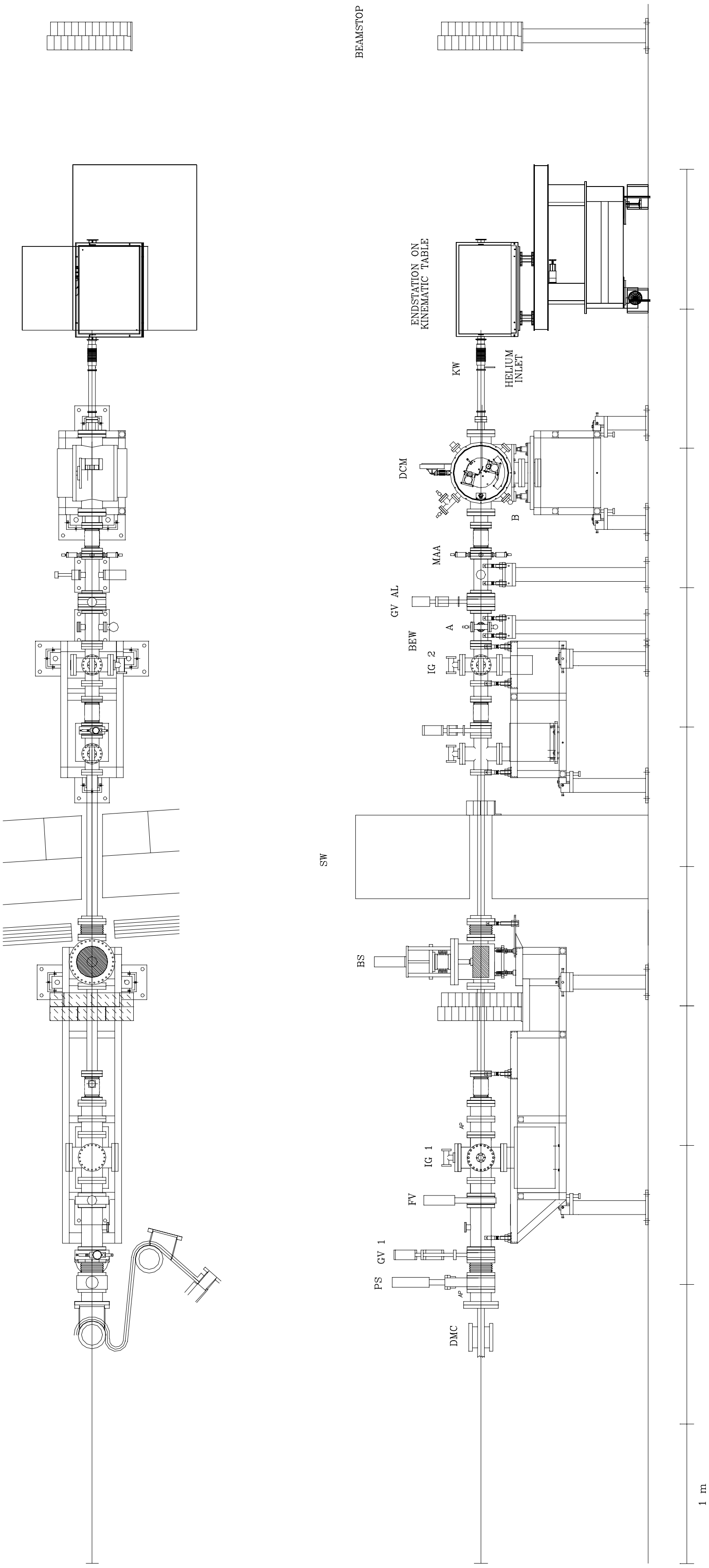

Figure 9. Mechanical layout of the ANL/CAMD microprobe beamline as top and side view.

3.2 The vacuum system of the double-crystal monochromator (DCM)

The vacuum system of the DCM is separated from the storage ring vacuum by the 125 µm beryllium window (BEW) and from the atmospheric pressure at the micro-probe end-station by a 50 µm or 12.5 µm kapton window (KW). The kapton window (KW) is mounted in a quick flange (QF50) and can be easily changed, according to the desired incident spectral range on the sample, with the thinner window used at lower monochromatic photon energies. The pressure in this section is limited to 10^{-3} torr due to the use of non-ultra-high vacuum compatible stepping motors inside the DCM vacuum chamber. A manual gate valve with a 150 µm aluminum window (GV AL) is located between the Be window (BEW) and the double crystal monochromator (DCM). By closing the aluminum window (GV AL), the DCM can be vented without exposing the Be window (BEW) to atmospheric pressure. In addition, the beamline can be operated with white or monochromatic beam without exposing the Be window to oxygen and causing potential oxidation. This is a very useful tool for alignment and adjustments of the DCM. A beam position monitor, consisting of a *DuPont* fluorescence screen[2] mounted on a pneumatic linear feed-through under 45° towards the incident beam and a *Burle* CCD[3] mounted on 2¾” conflat view port are installed on the 6” conflat nipple behind the gate valve with the Al window. Adjustable motorized slits (MAA) defining the white beam size are located upstream of the DCM.

Ion gauges (IG 1, IG 2) and *Convectron* gauges[4] (A, B) are installed at the indicated positions in Figure 9 and the pressures are monitored and displayed using a *Granville-Phillips* controller[5].

An experimental hutch, which is not shown in Figure 9, surrounds the beamline and the end-station, and is interlocked with the Bremsstrahlung shutter (BS). Shutters, such as the photon shutter (PS) and the Bremsstrahlung shutter (BS), gate valves and the pneumatic linear feed-through are remotely operated via an *Allen-Bradley* touch screen terminal[6] and a modular hardware system, consisting of a rack, power supply, central processing units (CPU) module and input/output (I/O) modules[7]. A search-and-secure procedure has to be executed before the shutters are enabled.

3.3 The double crystal monochromator

The double crystal monochromator that is used at the ANL/CAMD beamline was designed and built at the Laboratório Nacional de Luz Síncrotron (LNLS) at Campinas, Brazil [44]. It is a fixed exit double crystal monochromator, which utilizes one rotation (Theta) and mutually perpendicular independent translations (Trans 1, Trans 2) of the crystals in a Golovchenko configuration [45]. The design permits a maximum angular range of 8° to 60°. Currently, the DCM operates with Si(111) crystals, which based on the angular range and the

---

[2] Quanta III-T LG, DuPont, 1007 Market Street, Wilmington, DE 19898

[3] TC592-8 CCD Camera, 1/3", 580 TVL B/W with BLC, 24 V, 60 Hz; with 8 mm DD Lens, Burle, 2751 152nd Ave. NE, Redmond, WA 98052

[4] Series 275 *CONVECTRON*® Gauges, Granville-Phillips, 5675 Arapahoe Avenue, Boulder, CO 80303-1398

[5] 307 Vacuum Gauge Controller, Granville-Phillips, 5675 Arapahoe Avenue, Boulder, CO 80303-1398

[6] 2711-TC1 PanelView™, Touch Screen Terminal with color CRT (Cathode Ray Tube), Allen-Bradley, 1201 South Second Street, Milwaukee, WI 53204

[7] 1747 SLC™ 500 Fixed Hardware Style Programmable Controller, Allen-Bradley, 1201 South Second Street, Milwaukee, WI 53204

d-spacing of the Si(111) crystals 2d=6.271 Å, leads to a range of 2100 eV to 11900 eV in photon energy. To be able to provide monochromatic as well as white radiation, the first crystal (motion Trans 1) can be moved in and out of the white beam. This is indicated in Figure 10. The height offset between the white beam and the monochromatic beam was measured at the position of the *Huber* 4-jaw entrance slit of the Kirkpatrick-Baez focusing system to 20.45 mm.

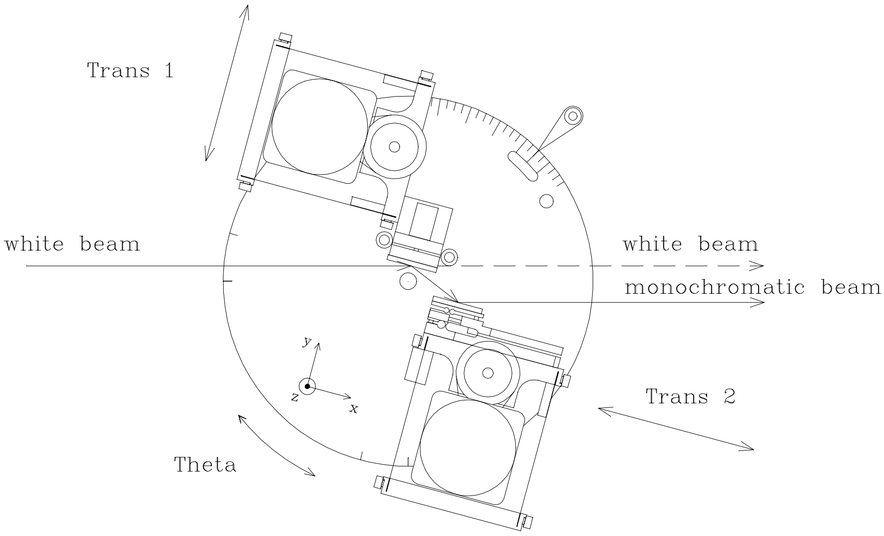

Figure 10. The Golovchenko configuration of the LNLS double crystal monochromator. The first Si(111) crystal can be translated in and out of the white incident beam providing the end-station with white (dashed line) and monochromatic (solid line) light. The height offset between the two beams is ~ 20 mm.

The LNLS double crystal monochromator, as it is shown in Figure 10, uses a double crystal reflection in a (+,-) configuration. This arrangement is also known as the non-dispersive parallel setting and is most commonly used in synchrotron radiation beamlines for XAS [46].

3.3.1 Short introduction to x-ray monochromators

To perform spatially-resolved spectroscopy, or x-ray absorption spectroscopy, a monochromatic x-ray beam is necessary. In the x-ray region, crystal monochromators are used to disperse the incident white synchrotron radiation. The Bragg equation describes the relation between the reflected wavelength λ and incident angle θ_B of the crystal towards the incoming white radiation. It can be written as

$$n\lambda = 2d \cdot \sin\theta_B, \qquad (5)$$

where n is an integer number, d is the d-spacing of the crystal. Eqn. (5) only takes into account the interaction of atoms with the incident radiation, but neglects scattering effects with neighboring atoms. The dynamical scattering theory on the other hand describes the reflectivity of perfect crystals and shows that, for a given wavelength λ, a crystal has a finite angular width, called the rocking curve width ω, in which reflection occurs.

In a symmetrical geometry, with the crystal planes parallel to the crystal surface, the rocking curve width can be calculated as

$$\omega = \frac{2}{\sin 2\theta_B} \frac{r_0 \lambda^2}{\pi V} C |F_h| e^{-M}, \tag{6}$$

with $r_0 = \frac{e^2}{mc^2}$. V is the unit-cell volume, λ is the reflected monochromatic wavelength, θ_B the Bragg angle, C the polarization factor which equals 1 or $|\cos(2\theta)|$ for s- or p-polarization, respectively. F_h is the crystal structure factor and e^{-M} is the Debye-Waller factor [47]. Figure 11 presents the rocking curves, calculated by the subroutine Bragg in *Shadow* [48] for the fundamental reflection of a Si(111) crystal at the photon energies of 2500 eV, 7500 eV, and 10000 eV, respectively. It can be seen that with decreasing photon energy the peak reflectivity is decreasing and the rocking curve width ω is increasing. In addition, the rocking curve center is shifting away from the Bragg angle. This behavior is as expected and can be compared to the results of Heald in [46].

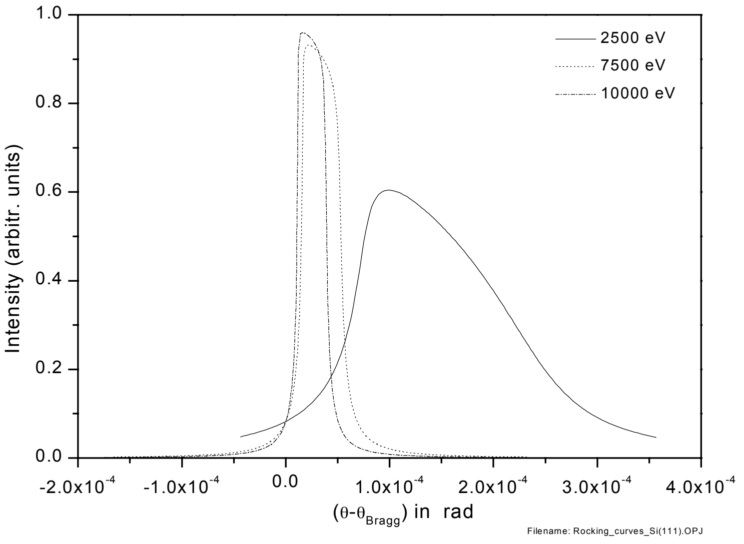

Figure 11. The rocking curves of a Si(111) crystal showing the fundamental reflection at the photon energies of 2500 eV, 7500 eV, and 10000 eV, respectively.

Detuning the crystal pairs is essential to avoid higher order contamination in the x-ray absorption spectra [49]. In the (+,-) configuration, this can be achieved by adjusting the crystal pair slightly non-parallel. Since higher order reflections are much narrower, they are more quickly suppressed than the fundamental reflection. Typically, optimum detuning results in a 50% loss of the fundamental intensity [46, 49]. So far, only the single crystal rocking curve has been presented in Eqn. (6) and illustrated in Figure 11. Neglecting the angular opening of the synchrotron radiation and assuming a Gaussian shape for the single rocking curve, it has been shown that the double crystal rocking width is at least $\sqrt{2}$ larger than single rocking curve width [50]. This value will be used in the section 3.3.2 to determine the energy resolution of the double crystal monochromator.

3.3.2 Energy resolution of the double crystal monochromator

A critical parameter in the ability to perform x-ray absorption spectroscopy is the energy resolution of the double crystal monochromator. The energy resolution is given by the differential form of the Bragg equation,

$$\frac{\Delta E}{E_{Photon}} = \frac{\Delta\lambda}{\lambda} = \Delta\theta \cot(\theta_B). \tag{7}$$

The angular spread of the reflected beam, $\Delta\theta$, is determined by the angular spread of the incident beam $\Delta\theta_{SR}$ and the intrinsic rocking curve width of the monochromator crystal $\Delta\theta_c$.

Assuming a Gaussian distribution, this yields

$$\frac{\Delta E}{E_{Photon}} = \sqrt{\Delta\theta_{SR}^2 + \Delta\theta_C^2}\cot(\theta_B). \tag{8}$$

Generally, the angular divergence of the electron beam $\sigma_{z'}$ and the angular intensity dependence of the synchrotron radiation emitted by a single electron σ_R are assumed to have Gaussian distribution. In this case, the vertical angular divergence of the photon beam $\sigma_{Z'}$ (please note capital Z) can be given [51] as

$$\sigma_{Z'} = \sqrt{\sigma_{z'}^2 + \sigma_R^2} \quad , \tag{9}$$

where $\sigma_{Z'}$ describes the divergence of the photon beam (the FWHM value $\Delta\theta_{SR} = 2.35 \cdot \sigma_{Z'}$), $\sigma_{z'}$ is the vertical divergence of the electron beam, and σ_R describes the angular intensity dependence of the synchrotron radiation from a single electron. The angular intensity dependence of the synchrotron radiation emitted by a single electron σ_R is well approximated for $\lambda > \lambda_c$ by [51]

$$\sigma_R(rad) = 0.565\left(\frac{1}{\gamma}\right)\left(\frac{\lambda}{\lambda_c}\right)^{0.425} . \tag{10}$$

The two other parameters used in Eqn. (10), γ and the critical wavelength λ_c, are defined as

$$\lambda_c(\text{Å}) = 5.59\frac{R(m)}{E^3(GeV)}, \tag{11}$$

and

$$\gamma = 1957 \cdot E(GeV). \tag{12}$$

The case of a CAMD bending magnet with a radius of curvature R=2.928 m and a ring energy of 1.3 GeV leads to a critical wavelength of λ_c=7.45 Å and γ=2544.1.

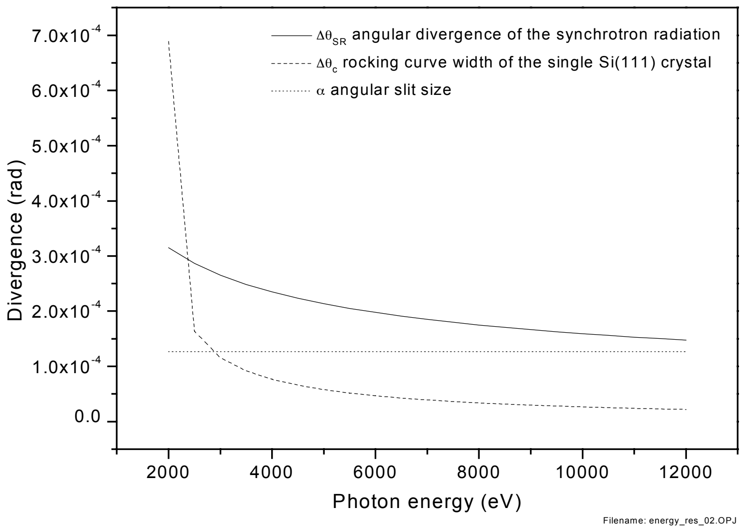

Figure 12. The angular spread of the incident beam $\Delta\theta_{SR}$ (solid line) and the intrinsic single crystal rocking curve width of the Si(111) monochromator crystal $\Delta\theta_c$ (dashed line) as a function of photon energy. Furthermore, the angular slit size (dotted line) of α=127 µrad, characteristic for the ANL/CAMD beamline based on source size, slit width and distance from the source, is also indicated.

Figure 12 presents the angular spread of the incident beam $\Delta\theta_{SR}$, the single crystal rocking curve for a Si(111) crystal, and an angular slit size of α=127 µrad. The angular slit size (FWHM) in radians is determined as

$$\alpha = \frac{2.35 \cdot \sigma_z + s}{L}, \tag{13}$$

where σ_z is the vertical source size with σ_z=187 µm, s is the vertical slit width with s=700 µm at a distance from the source L=9 m. Figure 12 shows clearly that the angular spread of the incident beam $\Delta\theta_{SR}$ is larger than the angular slit size. Hence, the angular slit width is used for $\Delta\theta_{SR}$ in Eqn. (8) and this leads to the energy resolution as

$$\frac{\Delta E}{E_{Photon}} = \sqrt{\left(\frac{2.35 \cdot \sigma_z + s}{L}\right)^2 + \left(\sqrt{2} \cdot \frac{2}{\sin 2\theta_B} \frac{r_e \lambda^2}{\pi V} C |F_h| e^{-M}\right)^2} \cdot \cot(\theta_B) \tag{14}$$

The energy resolution of the double crystal monochromator using 2 Si(111) single crystals and an entrance slit with s=700 µm at L=9 m over an energy range of 2000 eV to 12000 eV is shown in Figure 13.

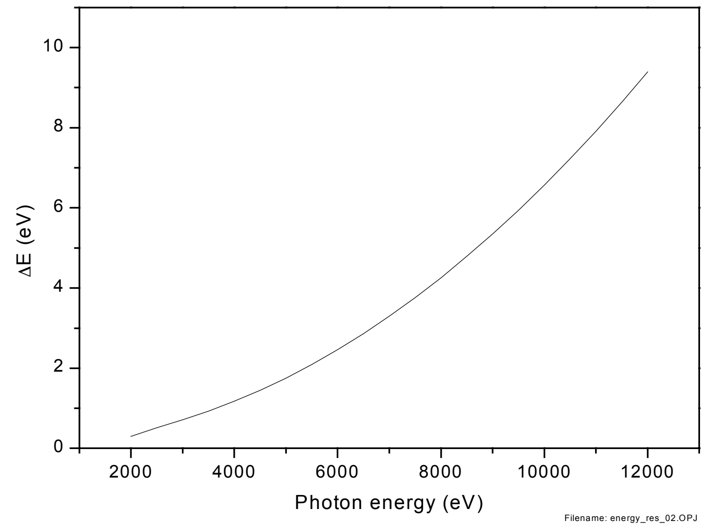

Figure 13. The energy resolution of the double crystal monochromator using Si(111) over the energy range of 2000 eV to 12000 eV. The curve was calculated using Eqn. (14).

3.3.3 Photon flux of the ANL/CAMD beamline

Photon flux measurements were performed at a ring energy of 1.3 GeV and an average ring current of ~ 100 mA. A 6” (15 cm) long ion chamber with air (N_2 78.1%, O_2 21%, C 0.03, Ar 0.94) as a fill gas was used as the x-ray detector. The ion chamber was mounted behind a 75 µm kapton window (KW), which is indicated in Figure 9. Due to space limitations, it was not possible to clamp the ion chamber directly to the kapton window (KW), leaving a ¾” (19 mm) long air gap before the monochromatic x-ray entered the ion chamber. The vertical slit width of the motorized adjustable aperture (MAA) located upstream of the monochromator (Figure 9) was set to 1 mm. During the experiment the double crystal monochromator was scanned in a photon energy range of 2700 eV to 11500 eV. Higher harmonics of the Si(111) crystals were detected up to 5000 eV and required detuning for harmonic rejection. At each photon energy, the ion chamber current I_{Ion} measured by a Keithley electrometer[8] and the ring current I_{Ring} were registered. Figure 14 presents the photon flux (dashed line) measured behind the Si(111) double crystal monochromator. The flux was obtained by applying the following equation

$$Flux\left[\frac{Photons}{s}\right]=\frac{I_{Ion}\left[\frac{Coulomb}{s}\right]\cdot 33.7\left[\frac{eV}{electron}\right]}{\left(1-e^{-\mu\cdot 15[cm]}\right)\cdot\left(1.602\cdot 10^{-19}\left[\frac{Coulomb}{electron}\right]\right)\cdot\left(Energy\left[\frac{eV}{Photon}\right]\right)},(15)$$

---

[8] 6512 programmable electrometer, Keithley Instruments Inc., 28775 Aurora Road, Cleveland, OH 44139

given by Brennan [52] to convert the measured ion chamber current I_{Ion} into incident number of photon per second. The energy loss per electron of 33.7 eV/e^- is specific for air and was also previously reported [52]. μ is the linear absorption coefficient of air and was reported by Henke et al. and Gullikson [53, 54]. $1.602*10^{-19}$ coulomb is the charge of a single electron. At this point it is necessary to mention that the values given in Figure 14, were corrected for the absorption of the 75 μm kapton window and for the ¾" air gap in front of the ion chamber. The flux discontinuity in the photon energy range of 3000 eV to 4000 eV is the result of the argon K absorption edge at 3205.9 eV [55].

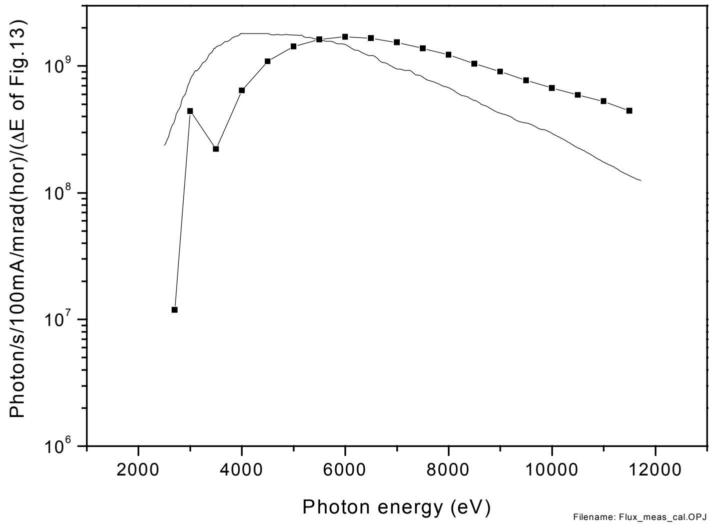

Figure 14. The measured spectral photon flux (dashed) behind the Si(111) double crystal monochromator. The solid line presents the calculated photon flux behind the Si(111) double crystal monochromator reported by Schilling et al. [56].

In addition, ray-tracing calculations were performed for the initial installation of the double crystal monochromator at the DCM beamline port 5B of the CAMD storage ring and published by Schilling et al. [56]. The data are also shown in Figure 14. At the time, the DCM beamline was very similar to the ANL/CAMD beamline. Therefore, it is appropriate to compare photon flux intensities given in Figure 14. It can be seen that the calculated and measured values of both curves are in good agreement.

3.3.4 Modifications of the double crystal monochromator for work in the low photon energy region

To be able to perform x-ray absorption spectroscopy at low photon energies such as the Si K-edge or the P K-edge, it is necessary to change monochromator crystals. Because the LNLS double crystal monochromator has an upper limit of rotation of 60° and is currently using Si(111) with 2d = 6.271 Å, the lowest photon energy attainable is about 2100 eV. This fact is shown in Figure 15. Changing monochromator crystals requires their re-alignment for parallelism.

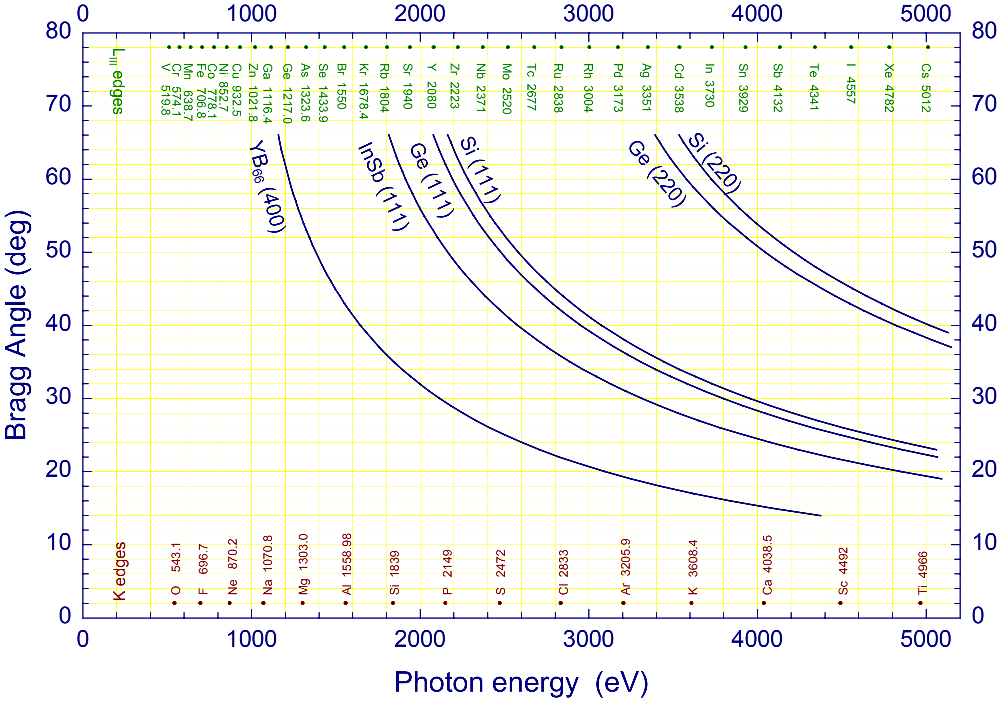

Figure 15. The low photon energy coverage of commonly used monochromator crystal for the angular range of the LNLS double crystal monochromator.

In order to be able to change and re-align crystals quickly and efficiently, the manually adjustable alignment micrometer screws that are used to adjust the parallelism of the crystals were motorized by two stepping motors (T1, T2). The motors are *MicroMo* 2-phase (bipolar) stepping motors with gear heads[9]. This modification eliminates the previously required venting of the DCM vacuum chamber for the following two alignment processes and thereby greatly accelerates and simplifies them. Changing the angle of the DCM by a large amount requires the re-alignment of the crystals' parallelism. This motion is realized by moving stepping motor T2 and rocking the second crystal around the z-axis in the indicated coordinate system (see Figure 16). Secondly, the alignment of the white and monochromatic beam need to be adjusted in the plane of the storage ring at the entrance slit of the end-station. This motion is executed by moving stepping motor T1 and tilting the first crystal around the x-axis. Although the angular resolution of the motorized alignment micrometer screws T2 is sufficiently small to execute rocking curve scans of the monochromator crystal, the initial solenoid/magnet device (SO) is still being used to perform this task and to detune for higher harmonics. It is located in the upper part of the second translation stage (Trans 2) and driven by a bipolar digital-to-analog converter (DAC) and a bipolar power supply.

---

[9] AM1524-A-0.25-12.5-07+15/8,141:1, MicroMo Electronics, Inc., 14881 Evergreen Avenue, Clearwater, FL 33762-3008

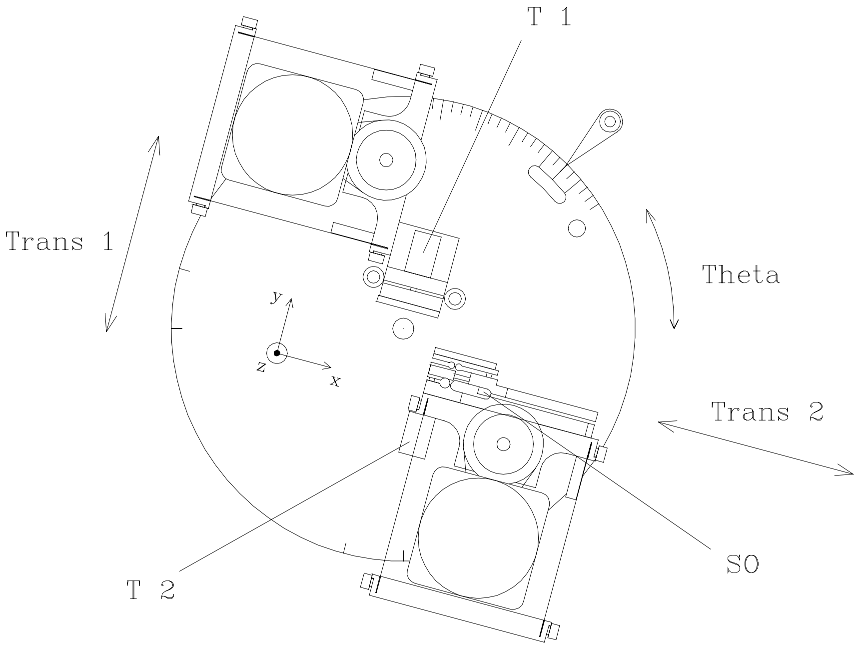

Figure 16. The motorized micrometer alignment screws T1 and T2 and the solenoid/magnet device SO.

4 The microprobe end station of the ANL/CAMD beamline

The main intention of this work is to design, build and commission a microprobe end-station, allowing the user to conduct spatially-resolved x-ray absorption and x-ray fluorescence experiments at lower photon energies (e.g. < 5000 eV). Based on the design of the DCM (refer to section 3.3, Figure 1), it is possible to change between white or monochromatic light. Therefore, the design of the end-station should accommodate this spectral change. The principal set-up is based on the design of beamline X-26C at the National Synchrotron Light Source (NSLS) reported by Rivers [57]. It was developed further during the course of this work, based on experience during the first x-ray microscopy experiments, which were conducted at the ANL/CAMD beamline [58].

Section 4.1 will introduce the physical setup of the end-station, which consists of 3 main functional units. Firstly, the kinematic table moves the entire microprobe end-station vertically when switching from white to monochromatic light and vice versa. Secondly, the helium enclosure with various vacuum fittings and polymer windows provides a controlled helium atmosphere, which eliminates air absorption at lower photon energies. Finally, the experimental hardware such as stages and detectors permits sample scanning and data acquisition. In section 4.2, the presentation of the modular electronic hardware based on CAMAC- and NIM crate system for the data acquisition is illustrated. At the end of section 4.2, the new *IDL* graphical user interface (GUI) for the beamline control and the data acquisition is presented. The Kirkpatrick-Baez focusing system, the essential optical part of the microprobe end-station, will be introduced in detail in chapter 5.

4.1 The physical setup

A side view of the microprobe end-station of the ANL/CAMD beamline is shown in Figure 17. The kinematic table is located inside the experimental hutch and positioned on damping feet (using sandbags in aluminum cubes). A 48” x 36” honeycomb breadboard[10] with maximum damping control is mounted via 3 motorized jacks to the steel frame of the table. In total, there are 6 stepping motors connected to the 3 jacks (3, 2, 1) to realize the 6 degrees of freedom (3 translations, pitch, yaw, and roll).

---

[10] Technical Manufacturing Cooperation, 15 Centennial Drive, Peabody, MA 01960

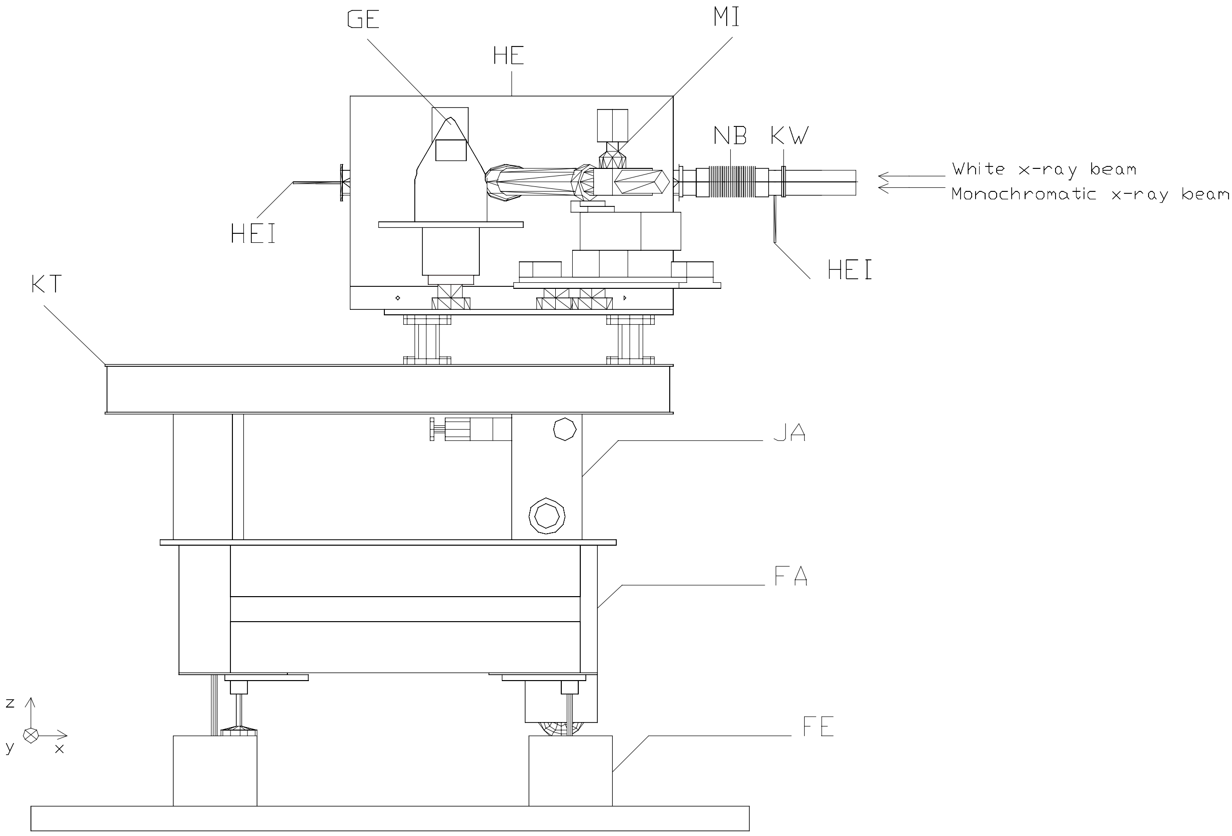

Figure 17. The side view of the ANL/CAMD end-station. The kinematic table (KT) consists of the damping feet (FE), a steel frame (FA) and 3 jacks with mounted stepping motors (JA). In addition, kapton window (KW), the neoprene bellow (NB), the two helium inlets (HEI), the K2 *Infinity* long-working distance microscope with the CCD camera (MI), the Ge-detector (GE), and the helium enclosure (HE) are shown.

The value of having the entire experiment on such as table is realized in correcting for the beam height offset when changing mode of operation from white light to monochromatic light. Upon translation of the first monochromator crystal into the beam, the beam is vertically offset by ~ 20 mm, as described in section 3.3 and shown in Figure 10. To account for this offset, one simply needs to translate the kinematic table in the z direction. Measurements of reproducibility were conducted by performing a 2-D scan of a characteristic sample using white and monochromatic light. Comparisons of the location of a particular feature in the white and monochromatic images of the sample have shown a good vertical positioning reproducibility of less than 200 µm. This allows a simple and fast switch of the set-up (10 min to 15 min) without a laborious re-alignment of the detectors, the focusing system, and the sample.

The absorption of air has a large impact when conducting measurements below 5000 eV. Assuming that the x-rays had to travel from kapton window to the sample stage (~ 50 cm) in air and considering that one absorption length of air at 2500 eV is ~ 3 cm, there would be essentially no intensity at the sample. Hence, to be able to conduct experiments at even lower photon energies such as ~ 2500 eV for the sulfur K-edge, a controlled helium atmosphere has to be introduced. Therefore, a helium enclosure (HE) was designed and built, containing the sample stage, the Kirkpatrick-Baez focusing system and the detectors. It is coupled to the beamline (at the kapton window (KW)) via two quick flanges (QF50), which are connected with a 2” diameter flexible neoprene bellows (NB). Thus, no breaking of the helium atmosphere while switching incident radiation is necessary. The two helium inlets (HEI) are marked in Figure 17 and permit purging of the helium enclosure (HE) with helium gas. The 27” x 19” x 18” helium enclosure is made of ¾” *Plexiglas*[11] sheets and holds a volume of ~ 120 l. With an inlet pressure of ~ 1 psi, it takes about 30 min to achieve a stable helium atmosphere, allowing measurements at low photon energies. Two circular entrance ports, which are located on the far side of the helium enclosure and which can not be seen in Figure 17, are used for access to the helium enclosure.

Furthermore, Figure 17 presents the integration of the long-working distance K2 *Infinity* microscope[12] (MI) and of the *Canberra* ultra-low energy germanium detector[13] (GE). The microscope is equipped with an *Infinity* CF-1 or CF-3 objective lens[14] and *Pelco* CCD camera[15]. It points under 45° to the incident beam through a *Plexiglas* view port, which is sealed off with a thin glass window. The image is displayed on a *JVC* video monitor[16] outside of the experimental hutch. It provides a field of view of 5 mm x 4 mm (horizontal x vertical) with an optical resolution of ~ 25 µm. Furthermore, the optical image can be acquired, using Pentium-II PC with PCI Bus frame grabber card[17]. The image is saved under *WindowsNT* in a *Windows* bit mapped format (*.bmp).

The 12” long snout of the *Canberra* Ge-detector enters the helium enclosure through a 2½” diameter hole, which is fitted with a 4” diameter *Plexiglas* flange. A 4” diameter neoprene bellows is connected to the flange. On the other end, the neoprene bellow is connected to a 4” diameter *Plexiglas* disk glued to an *A&N* 1” diameter quick coupling[18], which clamps down on the 1” diameter snout of the Ge-detector. Both instruments are mounted to sliding rails with vertically adjustable jacks, permitting a proximity- and vertical adjustment to the sample without disturbing the helium atmosphere in the enclosure.

A 3-dimensional view of the set-up inside the helium enclosure is presented in Figure 18. The incident x-ray beam (indicated by an arrow) passes through a motorized *Huber* 4-jaw entrance slit[19]. Here the incident beam, which illuminates the vertical and horizontal focusing mirror of the Kirkpatrick-Baez system (KBV, KBH), is defined. Usually, the vertical and horizontal slit widths are set to the acceptance of the KB-system. In the case of an incident angle $\theta_{inc}=7$ mrad with a mirror length of $l=100$ mm, this leads to a maximum slit width of 700 µm. After being focused, the beam travels through a 1” long ion chamber (IC) and impinges on the sample. The sample, with a typical size of 45 mm x 15 mm, is mounted to the sample holder (SH), which is located on the *Newport* motorized goniometric sample stage assembly[20]. The sample stage assembly is positioned under 45° to the incident beam. It consists of two translation stages (x[21], z[22]) and two rotation stages (phi[23], chi[24]). The resolution of the translation stages and the rotation stages is better than 1 µm and 0.003°, respectively.

---

[11] Plexiglas is registered trademark of the Rohm and Haas Company with the chemical name poly(methyl methacrylate) or PMMA.

[12] K2, Infinity Photo-Optical Company, 2530 Frontier Avenue, Boulder, CO 80301

[13] Model GUL01110P, Canberra Industries, Inc., 800 Research Parkway, Meriden, CT 06450

[14] CF-1, primary Magnification: 1.1 - 1.8 with a working distance: 12”-20”; CF-3 primary Magnification: 4-5.5 with a working distance: 4” - 6”, Infinity Photo-Optical Company, 2530 Frontier Avenue, Boulder, CO 80301

[15] PCHM 380-4X, Pelco, 300 W. Pontiac Way, Clovis, CA 93612-5699

[16] TM-122, Video Monitor, JVC Professional Products Company, 1700 Valley Road, Wayne, NJ 07470

[17] IV-400, MuTech Corporation, 85 Rangeway Road, Billerica, MA 01862

[18] 100-KM, vacuum quick coupling, A&N Corporation, 707 SW 19th Avenue, Williston, FL 32696

[19] Motorized cross slit screen 3013, Blake Industries, Inc., 660 Jerusalem Road, Scotch Plains, NJ 07076

[20] UTM25PE.1, MVN80, URM80PE, BGM50PE, Newport Corporation, 1791 Deere Avenue, Irvine, CA 92606

[21] UTM25PE.1, travel: 25 mm, resolution: 1 µm

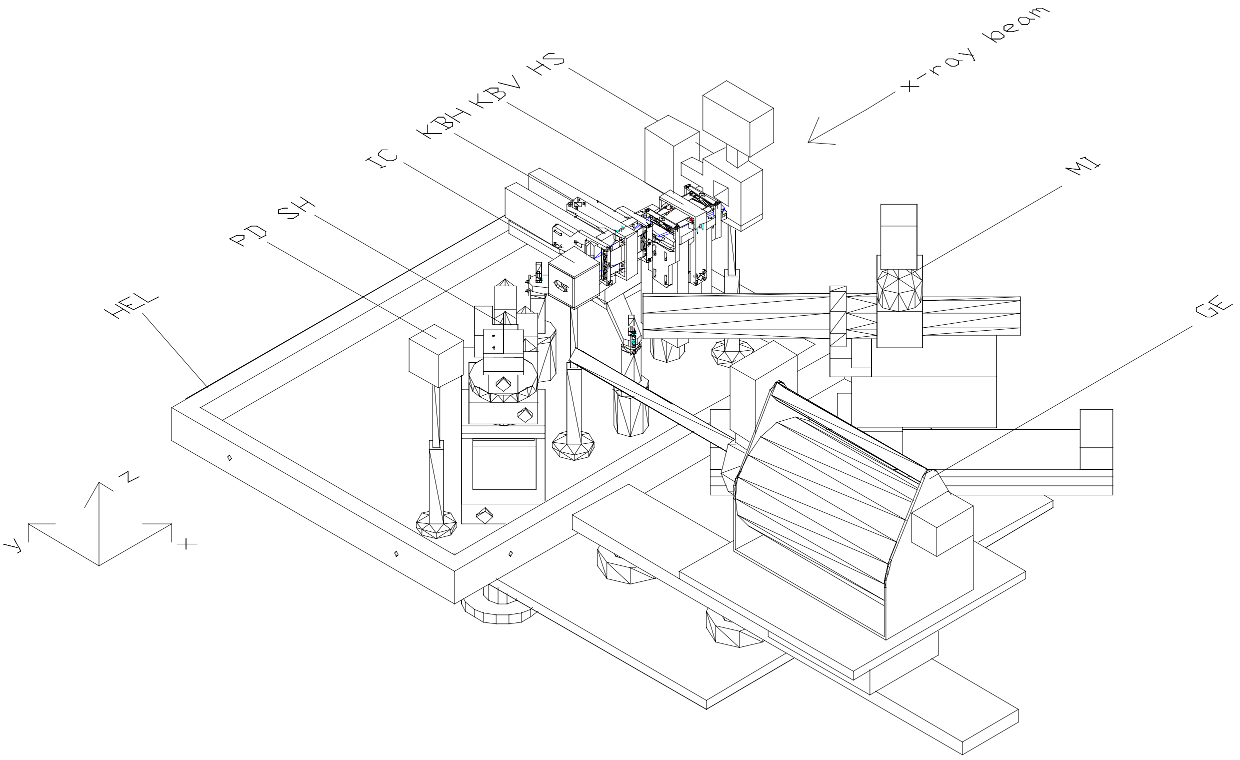

Figure 18. The experimental setup of the microprobe end-station. The experimental setup consists of the motorized *Huber* 4-jaw entrance slits (HS), the vertical and horizontal focusing mirror of the Kirkpatrick-Baez system (KBV, KBH), an ion chamber (IC), the *Newport* sample stage assembly with the sample holder (SH), and the *Hamamatsu* photo-diode (PD). The lower part of the helium enclosure (HEL), the K2 *Infinity* long working distance microscope (MI) and the Ge-detector (GE) are also labeled.

The transmitted beam can be detected with a *Hamamatsu* GaAsP photo-diode[25] (PD), which is located behind the sample holder (SH). The photo-diode has a quantum efficiency of ~ 350 for photon energies above 2000 eV. It is mounted into an aluminum housing and optically sealed off with 2 pieces of ~ 12.5 µm aluminized *Mylar*[26] film. This reduces the dark current to less than 1 pA. The set-up simultaneously allows the detection of characteristic fluorescence radiation being emitted by the sample. The energy-dispersive Ge-detector (GE) is positioned in the plane of the synchrotron storage ring 90° to the incident beam to minimize the scattered background [59].

---

[22] MVN80, travel: 12 mm, resolution: 0.5 µm

[23] URM80PE, travel: 360°, resolution: 0.003°, rotation moves the sample around the z-axis.

[24] BGM50PE, travel: ±45°, resolution: 0.002°, rotation moves the sample around the y-axis.

[25] Hamamatsu Cooperation, 360 Foothill Road, Box 6910, Bridgewater, NJ 08807-0910

[26] Mylar is a registered trademark held by its manufacturer DuPont with the chemical name polyethylene terephthalate, more commonly known as PET.

4.2 The instrumentation, the data acquisition and the software

The central instrumental elements of the microprobe end-station are a *Digital* Alpha DEC3000 workstation[27], a *DSP Technology* CAMAC[28] crate[29] with a *KineticSystems* SCSI controller[30] and a *Canberra* NIM[31] crate with a remote parallel interface[32] (RPI) and acquisition interface module[33] (AIM). The main components will be discussed in the following order. Firstly, the CAMAC motor controls and the CAMAC analog signal acquisition and processing, shown in Figure 19 and Figure 20, will be presented. Secondly, the NIM data acquisition, displayed in Figure 21, will be described. Finally, the new widget-based graphical user interface (GUI), which was written in *IDL*[34], will be presented [61].

The CAMAC crate houses 6 8-channel intelligent stepping motor controllers[35], which run 4 racks of 8-channel unipolar stepping motor (4-phase) drivers[36] and 2 racks of 8-channel bipolar stepping motor (2-phase) drivers[37]. Currently, 27 stepping motors are used in total. To actuate the solenoid/magnet device, which performs the fine parallel adjustment and the detuning of the crystals in the double crystal monochromator, a bipolar Digital-to-Analog Converter[38] (DAC) is used. The DAC drives a stand-alone *Kepco* bipolar power supply[39] with an output current of ±100 mA, which is applied to the solenoid/magnet device in the double crystal monochromator.

Data are acquired from detectors such as photo-diodes and the ion chambers and are handled by the CAMAC crate. *Keithley* electrometers[40] are connected to these detectors providing analog signals to a 4-channel Voltage-to-Frequency Converter[41]. The analog signals are converted into TTL (True Transistor Logic) output signals and fed into a 4-channel Quad-Scaler[42]. The scaler is usually gated with a real-time clock[43]. The data are then transferred to the *Digital* Alpha and stored. A schematic showing the analog data acquisition is shown in Figure 20.

---

[27] DEC3000, Compaq Computer Corporation, 20555 State Highway 249, Houston, TX 77070

[28] CAMAC is an international standard (with regards to electrical and physical specifications) of modularized electronics as defined by the ESONE (European Standards on Nuclear Electronics) [60].

[29] DSP Technology Inc., 48500 Kato Road, Fremont, CA 94538-7385

[30] Model 3929-Z1B, KineticSystem Corporation, 900 N. State Street, Lockport, IL 60441

[31] The NIM standard (DOE/ER-0457), originally an acronym for Nuclear Instrumentation Methods, was established in 1964 for the nuclear and high energy physics communities. The goal of NIM was to promote a system that allows for interchangeability of modules [60].

[32] Model 554, Canberra Industries, Inc., 800 Research Parkway, Meriden, CT 06450

[33] Model 556, Canberra Industries, Inc., 800 Research Parkway, Meriden, CT 06450

[34] Interactive Data Language (IDL), Research Systems, Inc. 2995 Wilderness Place, Boulder, CO 80301

[35] E500A, DSP Technology Inc., 48500 Kato Road, Fremont, CA 94538-7385

[36] Main crate model MDU-8 which 8 single board stepping motor drivers model MDB-6B, Advanced Control Systems Corporation, Old Mine Rock Way, Hingham, MA 02043

[37] Main crate model SPR9, which hosts 8 driver modules model SPD6U and 1 controller interface model SPC2, Advanced Control Systems Corporation, Old Mine Rock Way, Hingham, MA 02043 and one custom made bipolar driver

[38] DAC 645 with 12bit resolution, Hytec

[39] Model BOP20-10M, Kepco, Inc., 131-38 Sanford Avenue, Flushing, NY 11352

[40] 6512 programmable electrometer, Keithley Instruments Inc., 28775 Aurora Road, Cleveland, OH 44139

[41] 3569-L1A , KineticSystems Corp., 5305 Bay Lagoon Circle Orlando, FL 32819

[42] QS-450, DSP Technology Inc., 48500 Kato Road, Fremont, CA 94538-7385

[43] RTC-018, DSP Technology Inc., 48500 Kato Road, Fremont, CA 94538-7385

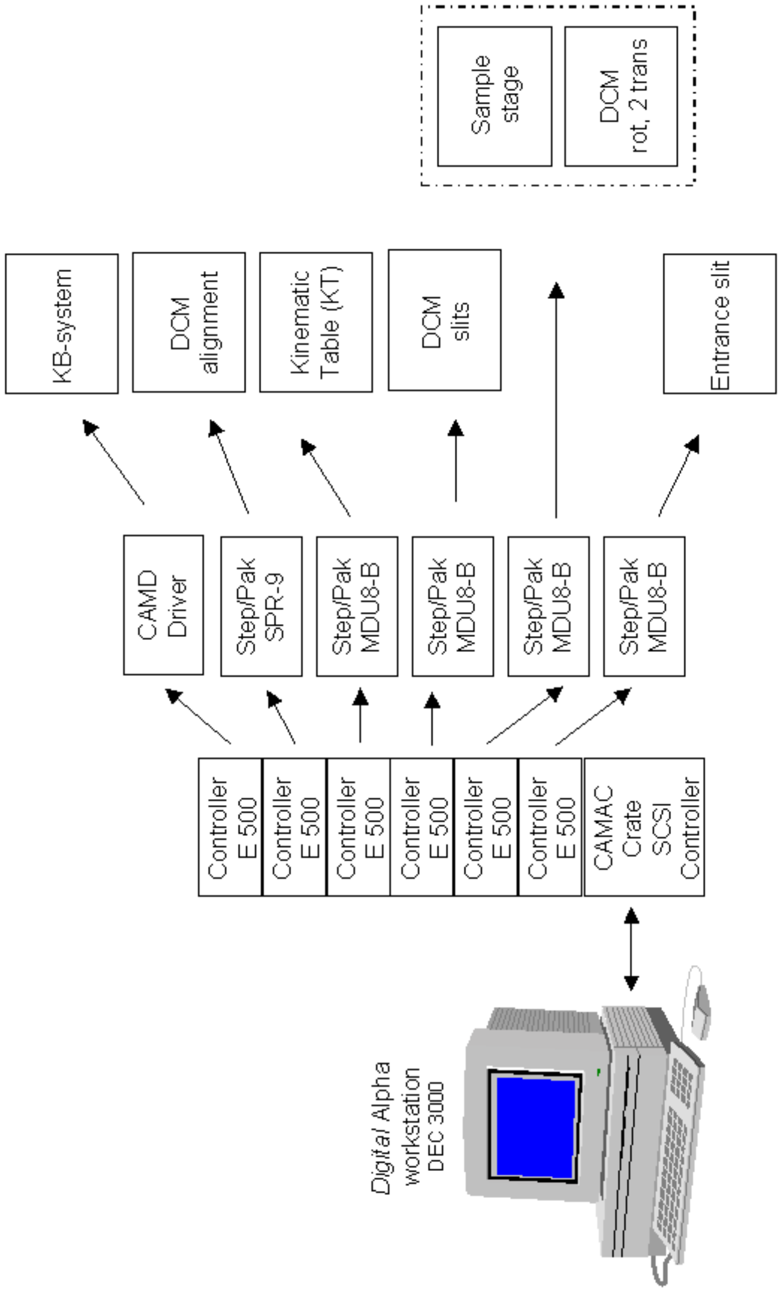

Figure 19. Schematic of the CAMAC stepping motor control of the microprobe end-station.

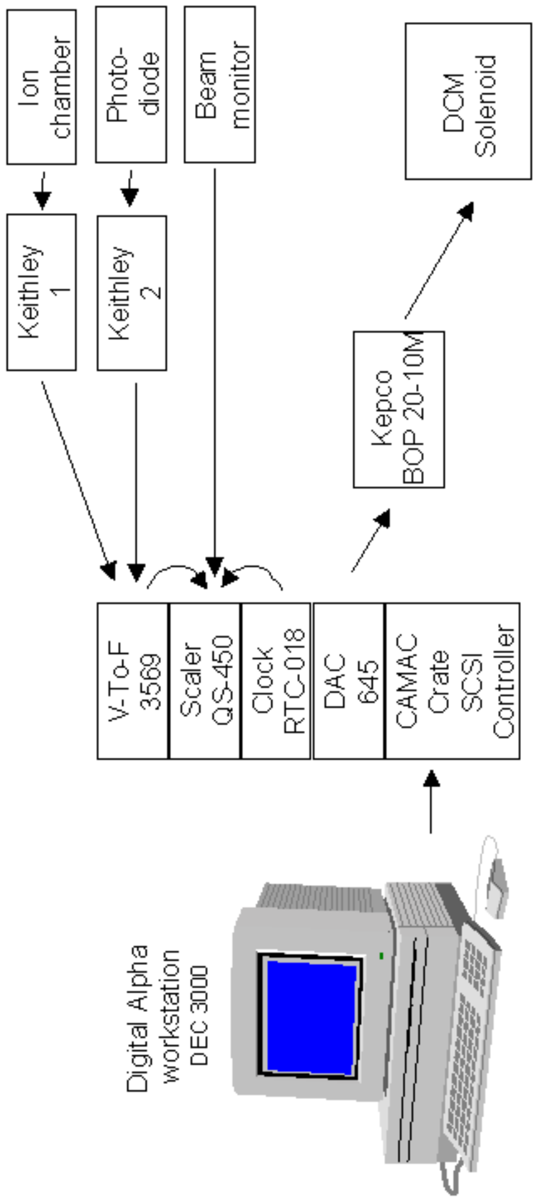

Figure 20. Schematic of the analog data acquisition. The control of the solenoid/magnet device in the double crystal monochromator is also shown.

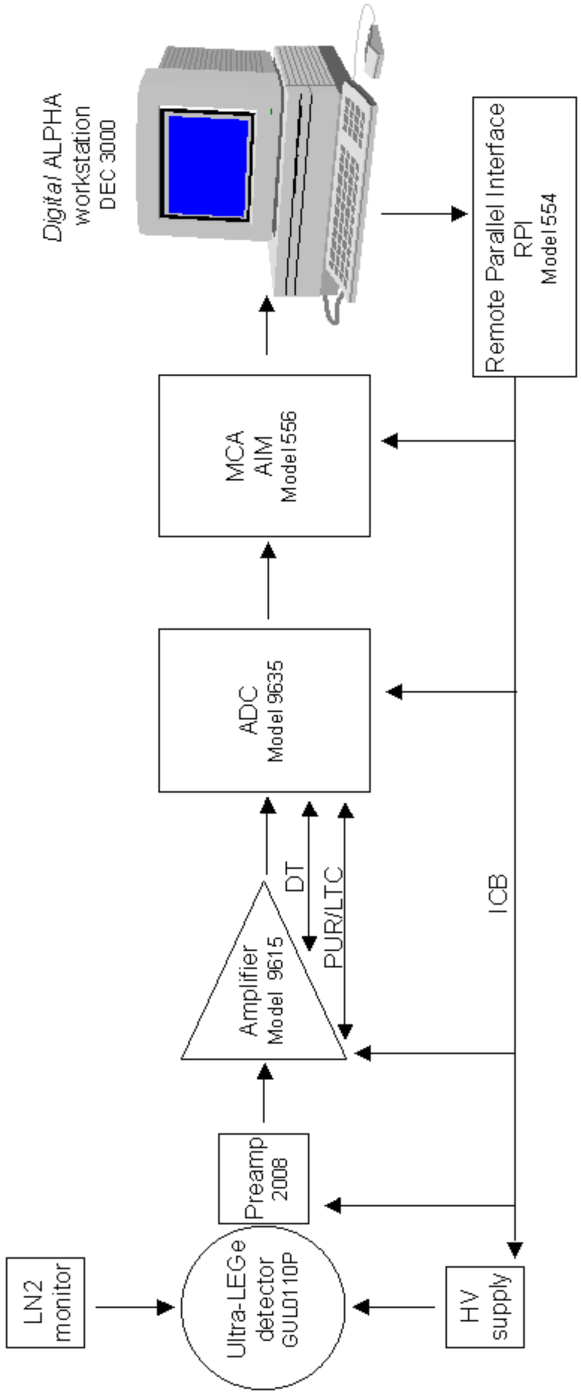

Figure 21. Schematic of the data acquisition using the energy-dispersive Ge-detector.

The data collected by the energy dispersive Ge-detector are processed by Canberra NIM crate. The schematic is shown in Figure 21. When a photon interacts with the germanium single crystal of the energy dispersive Ge-detector[44], a charge proportional to the photon energy is produced. The pulsed optical feedback amplifier[45] mounted on the detector converts the charge into a voltage pulse. This analog pulse is converted in the spectroscopy amplifier[46] into a near-Gaussian shaped pulse with its peak height proportional to the initial photon energy. An analog-to-digital converter[47] (ADC) generates equivalent binary number fed into the acquisition interface module[48] (AIM) module, which is a multi-channel analyzer (MCA). The MCA works in pulse height analysis mode (PHA), creating a histogram of frequency of occurrence (y-axis) versus pulse height (x-axis). Finally, the MCA spectrum is transferred with AIM's built-in Ethernet (LAN) interface to the *Digital* ALPHA. *Canberra's* spectroscopy software enables the user to display the entire MCA spectrum, save entire spectrum and/or save only regions-of-interest (ROI's).

A high voltage (HV) power supply module[49] is also located in the NIM crate and provides 500 V bias voltage for the Ge-detector. Via the remote parallel interface (RPI) and the instrument control bus (ICB), the user has software control from the *Digital* ALPHA over every module. A more detailed description can be found elsewhere [61].

The control software for ANL/CAMD beamline and the microprobe end-station is implemented in *IDL* (Interactive Data Language), a product of *Research Systems Incorporated*. *IDL* provides a comprehensive set of commands for the declaration and manipulation of data structures, as well as access to the local window manager for the production of a graphical user interface (GUI).

Initially, the control software presents a single window consisting of a text display of the current energy setting of the DCM and a menu bar with the following five headings: FILE, MONOCHROMATOR, SCAN, DATA and HARDWARE. In the following, a brief description of the operations accessed through each of the menu headings is given.

- Menu-heading FILE gives the user access to the *IDL* shell and also allows the user to end the beamline control session.
- Menu-heading MONOCHROMATOR provides the user with various routines to manipulate the double crystal monochromator such as positioning the monochromator to a specific photon energy, performing a rocking curve scan and running an optimization scan.
- Menu-heading SCAN provides set-up routines for 1- and 2-dimensional spatial scans and for XANES and EXAFS scans. An auto-focusing routine to focus the Kirkpatrick-Baez system can also be found here.
- Menu-heading ACQUISITION SETUP displays all acknowledged devices such as scalers, which have to be selected or deselected as active channels for the acquisition by clicking on checkboxes. The selected devices are plotted in real time during data acquisition.

---

[44] Model GUL01110P, ultra low energy germanium detector with a resolution of 150 eV (FWHM) at 5895 eV (Mn Kα)

[45] Model 2008, Canberra Industries, Inc., 800 Research Parkway, Meriden, CT 06450

[46] Model 9615, Canberra Industries, Inc., 800 Research Parkway, Meriden, CT 06450

[47] Model 9635, Canberra Industries, Inc., 800 Research Parkway, Meriden, CT 06450

[48] Model 556, Canberra Industries, Inc., 800 Research Parkway, Meriden, CT 06450

[49] Model 9641, Canberra Industries, Inc., 800 Research Parkway, Meriden, CT 06450

- Menu-heading HARDWARE gives the user direct access to some of the hardware employed at the ANL/CAMD beamline. Here, the main interest is to edit various parameters for the motor operation.

5 The Kirkpatrick-Baez (KB) focusing system

The choice of an achromatic Kirkpatrick-Baez focusing system was necessitated by two factors. The first involved being able to conduct spatially-resolved x-ray fluorescence mapping, as well as spatially-resolved x-ray absorption spectroscopy. Secondly, it was necessary to accept as much incident synchrotron radiation as possible in order to decrease measuring times. The Kirkpatrick-Baez focusing system is based on total external reflection of 2 mutually perpendicular concave curved cylindrical mirrors, which was first introduced by Kirkpatrick and Baez [62]. As part of a collaboration between GSECARS at the University of Chicago and CAMD at Louisiana State University, a Kirkpatrick-Baez focusing system was built. Its principle is based on forming elliptically curved cylindrical optical surfaces via dynamically bending float glass mirrors, which is a very cost effective solution [15, 63, 64].

Section 5.1 will present the theory of x-ray focusing using total external reflection off a dynamically bent x-ray mirror by forming an elliptical figure. Details such as the focusing properties of the ellipse, the critical angle under which total external reflection occurs, and the impact of the rms slope error and the rms surface roughness will be pointed out. Consequently, the principal two-parameter bender scheme and its mechanical design will be introduced.

Section 5.2 summarizes detailed ray-tracing calculations, which have been performed to simulate the performance of the optical system consisting of the CAMD bending magnet source, the beamline, and the Kirkpatrick-Baez focusing system. Moreover, this chapter will also offer an understanding of the impact of the rms slope error, illustrated by the results of the ray-tracing calculations.

The primary experimental results characterizing the focal spot sizes, the intensity distribution of the focal spot, as well as the photon flux at the point of the sample will be depicted in section 5.3. The resolution of the microprobe set-up acquiring data in fluorescence mode is presented by determining the modular transfer function. A brief summary of the overall performance, by comparing the values obtained by both geometric optics and ray-tracing calculations to the experimental values, is also given in section 5.3.

5.1 Theory of x-ray focusing and the Kirkpatrick-Baez focusing system

This chapter gives an introduction to achromatic x-ray point-to-point focusing using dynamically bent x-ray mirrors. Section 5.1.1 presents the surface equations of the ellipse and its unique focusing properties for point-to-point focusing. It is also pointed out that the rms slope error of a mirror degrades its theoretical performance and therefore, the performance has to experimentally qualified. Hence, slope error measurements have been conducted, which are presented in section 5.1.2. The principle that x-ray reflection off a mirror surface occurs solely under total external reflection is presented in section 5.1.3. Section 5.1.4 depicts briefly the principal scheme of the two-parameter bender being used in the Kirkpatrick-Baez focusing system, followed by a more detailed description of the resulting mechanical design. Finally in section 5.1.5, a qualitative model for the maximization of the focused photon flux is presented, which addresses the trade-off between the acceptance of the Kirkpatrick-Baez focusing system and the decrease in photon flux by the critical angle.

5.1.1 Theory of point to point focusing, surface equation of the ellipse and impact of the slope error

A mirror with an elliptical figure is the ideal focusing element because rays emitted from one point focus F_1 will be perfectly focused into the second point focus F_2. The geometry is shown schematically in Figure 22.

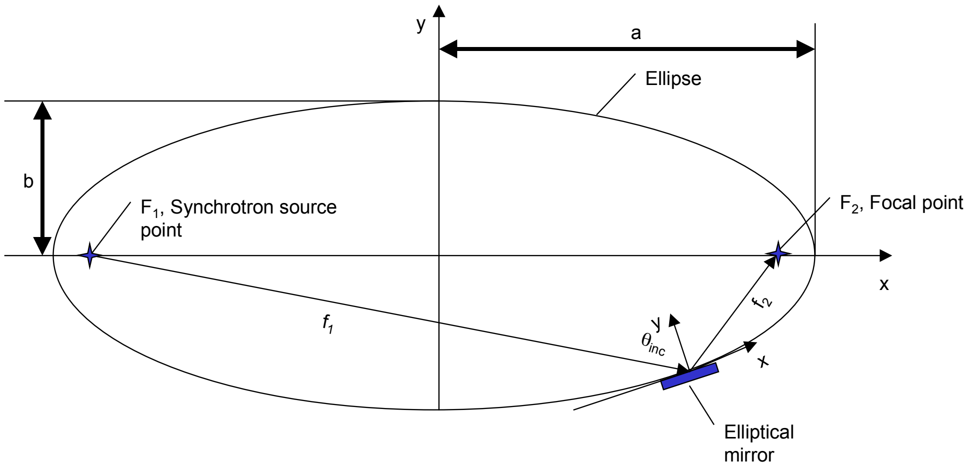

Figure 22. The geometry of the ellipse, which perfectly focuses the rays emitted in F_1 into the focal spot F_2. The elliptical focusing mirror is only a segment of the entire ellipse.

The equation of an ellipse as a function of the major and minor axis for a Cartesian coordinate system centered in the center of the ellipse, is given by

$$\frac{X^2}{a^2} + \frac{Y^2}{b^2} = 1 \tag{16}$$

The major axis a and minor axis b of the ellipse can be expressed in terms of the object and image distances f_1 and f_2 and the incidence angle θ_{inc} as

$$a = \frac{(f_1 + f_2)}{2}, \tag{17}$$

and

$$b = \sqrt{a^2(1 - e^2)}. \tag{18}$$

Please note that the major axis a depends only on f_1 and f_2 and stays therefore fixed in a given geometry, whereas the minor axis b will change depending on the incidence angle θ_{inc}. This can be seen in Eqn. (19) and will be also shown in the ray-tracing results that follow in section 5.2.

The parameter e is called the eccentricity [65, 66] and is given by the following equation

$$e = \frac{1}{2a}\sqrt{f_1^2 + f_2^2 - 2f_1 f_2 \cdot \cos(2\theta_{inc})}. \tag{19}$$

In analogy to the thin lens equation [67], the demagnification of the optical system is simply given by

$$M_D = \frac{f_1}{f_2}. \tag{20}$$

The object distance, f_1, gives the length from the source to the middle of the mirror. The image distance, f_2, is determined by the stretch of the mirror to the focal spot. In the current optical system of the CAMD/ANL microprobe beamline the horizontal and vertical demagnification are M_{DH}~61 (f_{1H}/f_{2H}=9.2m/0.15m) and M_{DV}~35 (f_{1V}/f_{2V}= 9.09m/0.26m), respectively. These result in a theoretical horizontal and vertical focal spot size of σ_{xF}=13.6 µm and σ_{zF}=5.3 µm, based on the horizontal and vertical source sizes of σ_x=831 µm and σ_z=187 µm [68].

Deviations from the ideal surface figure, commonly expressed as rms slope error of the mirror surface figure, lead to an oversized focal spot. There are several sources of slope error for high quality x-ray mirrors, including gravitational sag, heat load mainly from the white synchrotron radiation, and figure distortions due to incorrect dynamical bending. These add to the intrinsic figure error of the optical surface and create the integrated slope error budget σ_{Slope} of the mirror [69]. In order to take full advantage of the synchrotron source brightness, the integrated slope error budget σ_{Slope} has to be smaller than the vertical angular source size, viewed from the position of the mirror [63]. This can be expressed as

$$\sigma_{Slope} < \frac{\sigma_z}{f_1}, \tag{21}$$

where σ_z is the vertical source size.

This necessitated the determination of the intrinsic slope error of the float glass mirror blanks and hence, slope error measurements were conducted. These experiments are described in detailed in the next chapter and the results will be used in the ray-tracing experiments, which follow in section 5.2.

5.1.2 Measurements of the intrinsic slope error of float glass mirrors

A Long-Trace-Profilometer[50] (LTP II) was used to determine the slope error of float glass mirror blanks [70, 71]. The goal was to select mirror blanks which have an intrinsic slope error smaller than the minimum integrated slope error budget σ_{Slope} of the Kirkpatrick-Baez focusing system at the ANL/CAMD beamline (refer to Eqn. (21)). The minimum integrated slope error budget σ_{Slope} is determined by the vertical source size σ_z=187 µm and the distance between the source and the vertical focusing mirror f_{1V}=9.09 m to σ_{Slope}=20.3 µrad. Figure 23 presents a schematic of the optical system of the LTP II. Light from the laser diode (LD) is sent into the beam splitter (BS 1) and 2 prisms (SP, AP), so that 2 parallel, coherent beams emerge downward towards the surface of the float glass mirror (FGM). The beams are

---

[50] Long-Trace-Profiler II, Continental Optical Corporation, 15 Power Drive, Hauppauge, NY 11788

reflected from the FGM's surface and hit the beam splitter (BS 2), which directs the beams into the Fourier transform lens (FTL). The FTL projects the interference pattern of the beams, onto the linear photo-diode array detector (LPAD). In addition, an extra beam pair is produced in beam splitter 2 (BS 2). It will be reflected onto a reference mirror (RM) and directed through the beam splitter (BS 2) into the Fourier transform lens (FTL). In this way, a 2nd interference pattern is produced and is also detected in LPAD. The 2nd beam pair is used to correct the slope data of the FGM surface for laser beam instability and sag of the beam, on which the optical head (indicated by the dashed box around the main optical system) is moving along while measuring the FGM [72-74].

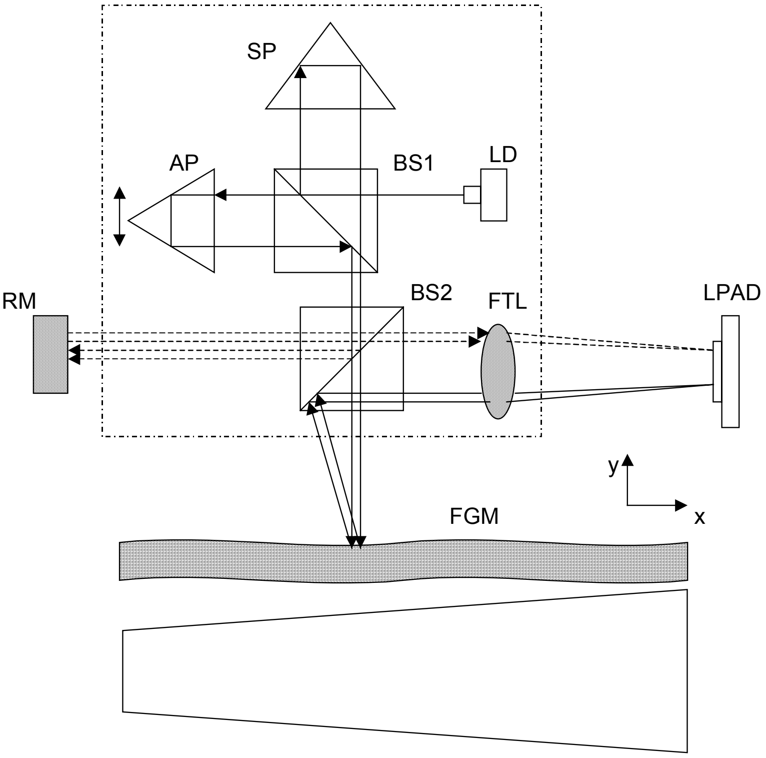

Figure 23. Schematic of the optical system of the Long-Trace-Profiler (LTP II) [70, 72] and the float glass mirror blank under test.

The slope error of 22 mirror blanks from *Abrisa Industrial Glass*[51] were measured along a 90 mm strip, starting the scan at the small end of each mirror and neglecting 5 mm at each end of the 100 mm long glass surface. The step size was 2 mm. Data were collected from both sides of the mirror blanks since the experiments showed that each mirror blank has a concave and a convex side. Based on the current geometry and the resulting large radii of curvature (~ 200 m), it is favorable to use the convex (negative sign) surface of the mirror. This curvature will be reversed during the focusing procedure by applying a bending moment at either side of the mirror.

The data analysis involved the following steps. The intensity data over trace position were converted into slope data over trace position. A 0th order polynomial, equivalent to the tilt of the mirror, was removed from the slope data and then converted into height data. At this point the sign and magnitude of the mirror curvature were recorded. Then, a 1st order polynomial was removed from the slope data, which is identical to the noted curvature. This is feasible, since it is possible to remove the 1st order slope via dynamical bending. This yields the final

---

[51] Abrisa Industrial Glass, Inc., 456 Fleet Avenue, Ventura, CA 93003

intrinsic slope of the float glass mirror, which cannot be removed by dynamically bending. The results showed that the intrinsic slope error ranged between 9.5 µrad and 70 µrad. 10 float glass mirrors were well below the minimum integrated slope error budget σ_{Slope}=20.3 µrad. Each mirror shows a convex and concave surface, but so far no correlation between surface sign and the float glass mirror side, which was in touch with the liquid tin during the manufacturing process, can be established. The best mirror with an intrinsic slope error of σ=9.5 µrad was installed as the vertical focusing mirror. The horizontal focusing mirror has an intrinsic slope error of σ=10.7 µrad. These two mirrors were used for the experiments being described from here on.

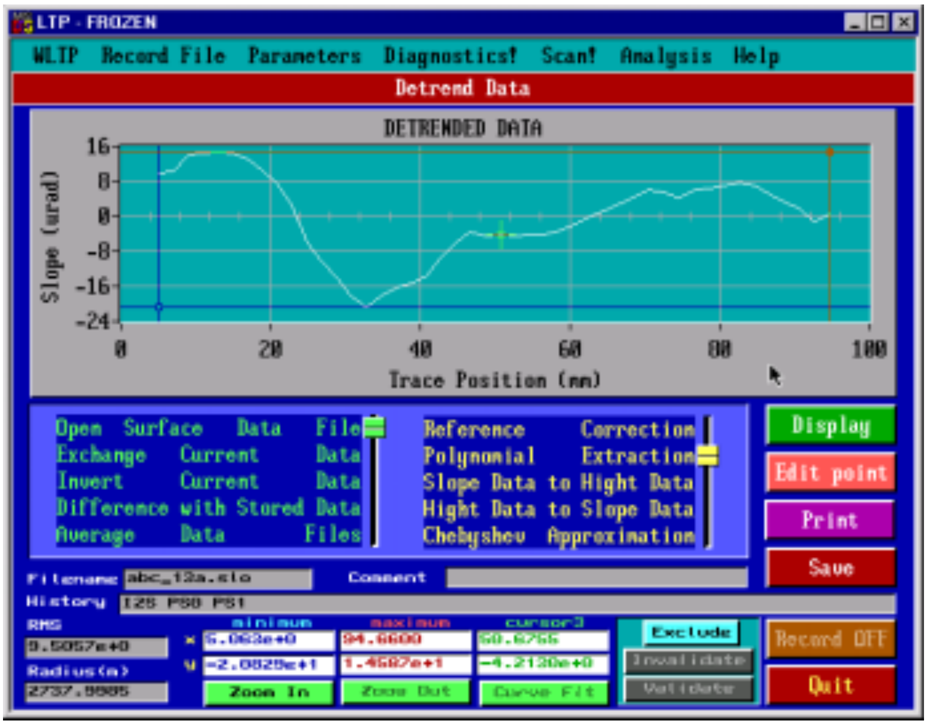

Filename abc_12a.slo
Comment
History I2S PS0 PS1
RMS 9.5057e+0
Radius(m) 2737.9985
x 5.063e+0 94.6600 50.6766
y -2.0825e+1 1.4587e+1 -4.2130e+0

Figure 24. The data analysis display of the LTP II for the vertical focusing mirror. 0th and 1st polynomials are removed to yield the intrinsic slope error σ=9.5 µrad, which can not be compensated for with dynamical bending.

5.1.3 Reflectivity of x-ray mirrors using total external reflection and the impact of surface roughness

X-ray mirrors take advantage of the phenomenon that under sufficiently small grazing angles, total external reflection occurs on a smooth, either crystalline or amorphous surface. This is shown in Figure 25 for the reflectivity of gold in the energy range between 1000 eV and 12000 eV for grazing angles of 0.5°, 1°, 2°, 3°, 4°, and 5°. For large angles the reflectivity is very low over the entire photon energy range. However, with decreasing grazing angles, the reflectivity increases and builds a high reflectivity plateau, which falls sharply at very high energy. This “cut off” becomes sharper with higher photon energy. Additional decrease of the reflectivity due to x-ray absorption is caused by the M absorption edges of gold in the energy range between 2200 eV and 3400 eV, which can be clearly seen in Figure 25 for angles of 0.5° and 1°.

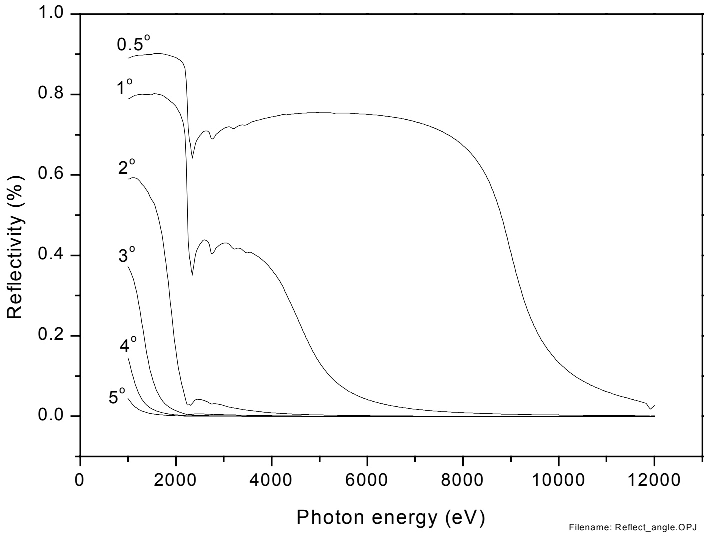

Figure 25. The reflectivity of gold for grazing angles of 0.5°, 1°, 2°, 3°, 4°, and 5°. and a rms surface roughness of 0 Å [53, 54].

The grazing angle, at which total external reflection starts to occur, is known as the critical angle θ_{crit}. It can be determined by Snell's law [67],

$$n_1 \cdot \sin\alpha_1 = n_2 \cdot \sin\alpha_2 , \qquad (22)$$

considering only the real part of the complex refractive index and assuming that the angle α_2=90° and hence that the refracted beam propagates in the surface of the reflecting material. Rewriting Eqn. (22) in terms of the grazing angle θ_{graz} yields

$$\cos\theta_{graz} = 1 - \delta . \qquad (23)$$

Expanding Eqn. (23) in a Taylor series leads to

$$\theta_{crit} \approx \sqrt{2 \cdot \delta} , \qquad (24)$$

where δ is the refractive index decrement. δ can be determined by the real part of the atomic scattering factor f_{1S} [75], using

$$\delta = \frac{r_0 \cdot \lambda^2}{\pi} \cdot \frac{N_A}{A_i} \cdot \rho_i \cdot f_{1S} . \qquad (25)$$

r_0 is the classical electron radius $r_0 = 2.818 \cdot 10^{-15}$ m, N_A is the Avogadro number $N_A = 6.023 \cdot 10^{23}$ mol^{-1}, A_i is the atomic weight in g/mol and ρ_i is the density of the element i in g/cm^3. f_{1S} is the real part of the atomic scattering factor, which is listed by Henke et al. [53] and is easily available from Gullikson [54]. This leads to

$$\theta_{crit} \approx \sqrt{2\cdot\frac{r_0}{\pi}\cdot\frac{N_A}{A_i}\cdot\rho_i\cdot f_{1S}}\cdot\lambda . \tag{26}$$

In Eqn. (25) it can be seen, that in order to increase the critical angle θ_{crit} for a given wavelength or photon energy, it is favorable to use high Z coating materials with large densities ρ.

The reflectivity of an x-ray mirror is influenced by the surface roughness of the mirror. In mathematical models, surface roughness is regarded as a spatial disturbance with a high frequency superimposed on the x-ray mirror surface, which results in scattering and hence decreases the reflectivity [76]. The reflectivity of a rough surface is well described using the approximation given by the Névot-Croce factor [77]. Figure 26 depicts the reflectivity of gold mirror surface without surface roughness and with surface roughness of 5 Å, 10 Å and 20 Å for a grazing angle of 0.401° (7 mrad) [53, 54].

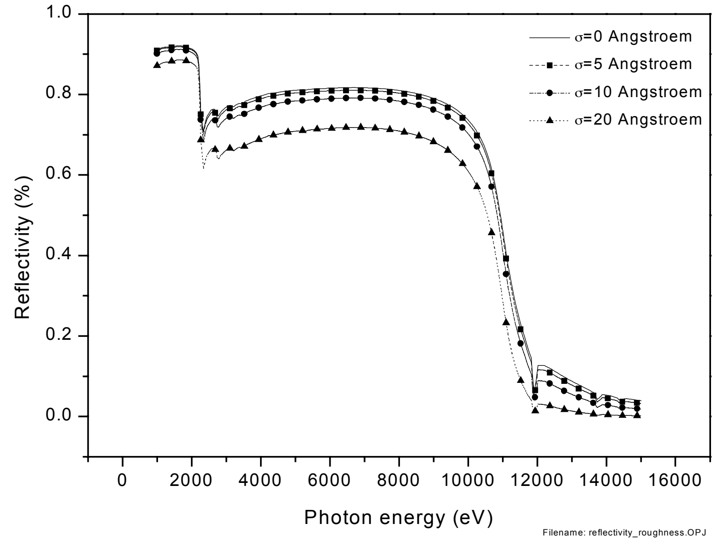

Figure 26. The reflectivity of a gold surface for a grazing angle angle θ_{graz} of 0.401° (7 mrad) and 0 Å surface roughness (solid line). In addition, surface roughness' of 5 Å (square), 10 Å (circle), and 20 Å (up triangle) was included.

Experimentally, surface roughness can be measured with a 1-dimensional topography scan, using an atomic force microscope or a profilometer. The Fourier transform of the data yields the 1-dimensional power spectral density (PSD) of the surface[52] [78] with the smallest and highest frequencies being defined by the step size and the scan length of the instrument. The

---

[52] Highly polished surfaces, such as x-ray mirror surfaces, have often fractal behavior, i.e. they are self-similar [78]. The description applying the power spectral density (PSD) is still meaningful, whereas the rms surface roughness σ and correlation length l is useless, unless one specifies the spatial frequency band pass to which the values refer [76].

surface roughness (σ^2_{Rough}) is obtained as the integral of the PSD. For a small surface roughness[53], the bi-directional reflectivity distribution function (BRDF) estimates the amount of light which is scattered into a small range of angles from the specular reflection [78]. Thus, the specular reflectivity decreases (refer to Figure 26) and the scattered light creates a halo around the focused specular beam, deteriorating the contrast of the image.

5.1.4 The Kirkpatrick-Baez focusing system

The Kirkpatrick-Baez mirror focusing system employs a two-parameter bender design for each mirror, which applies 2 independently adjustable vertical forces F_{F1} and F_{F2}. This design permits the control of the bending moment distribution over the entire mirror, allowing adjustment of the elliptical figure of the mirror, so that the mirror's Taylor series are matched, order by order, to the ideal ones [64]. Figure 27 presents a schematic of the mirror bender with two vertical forces. A surface normal translation is needed to accurately translate the mirror in and out of the x-ray beam during focusing. To adjust the grazing angle θ_{graz} in order to change the cut-off photon energy and the acceptance of the mirror, a rotation around the z-axis is also implemented in the design of the two-parameter bender. Altogether, 4 independently controllable motions are installed at each Kirkpatrick-Baez mirror bender.

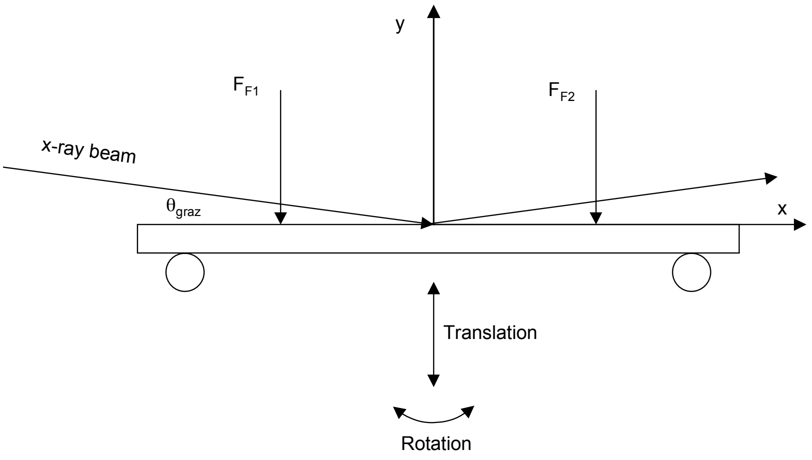

Figure 27. Schematic of the mirror bender with two independent vertical forces. The surface normal translation and rotation of the mirror are also depicted.

Subsequently, the mechanical design of the vertical bender, realizing the principle design as explained previously, is described as an example. Figure 28 presents a 3-D view of the Kirkpatrick-Baez focusing system as it is installed at the microprobe end-station at the ANL/CAMD beamline. Both focusing mirrors with their bending, translation, and rotation mechanisms are mounted on a tripod. This permits a height adjustment (z-axis) to the incident beam using 3 *Newport* fine adjustment screws[54].

---

[53] Small surface roughness: $\sigma_{\text{Rough}} \cdot q \ll 1$, with momentum transfer q from the boundary to the photon as $q = \frac{4\pi}{\lambda} n_1 \sin\theta$.

[54] AJS8-0.5, Newport Corporation, 1791 Deere Ave., Irvine, CA 92606

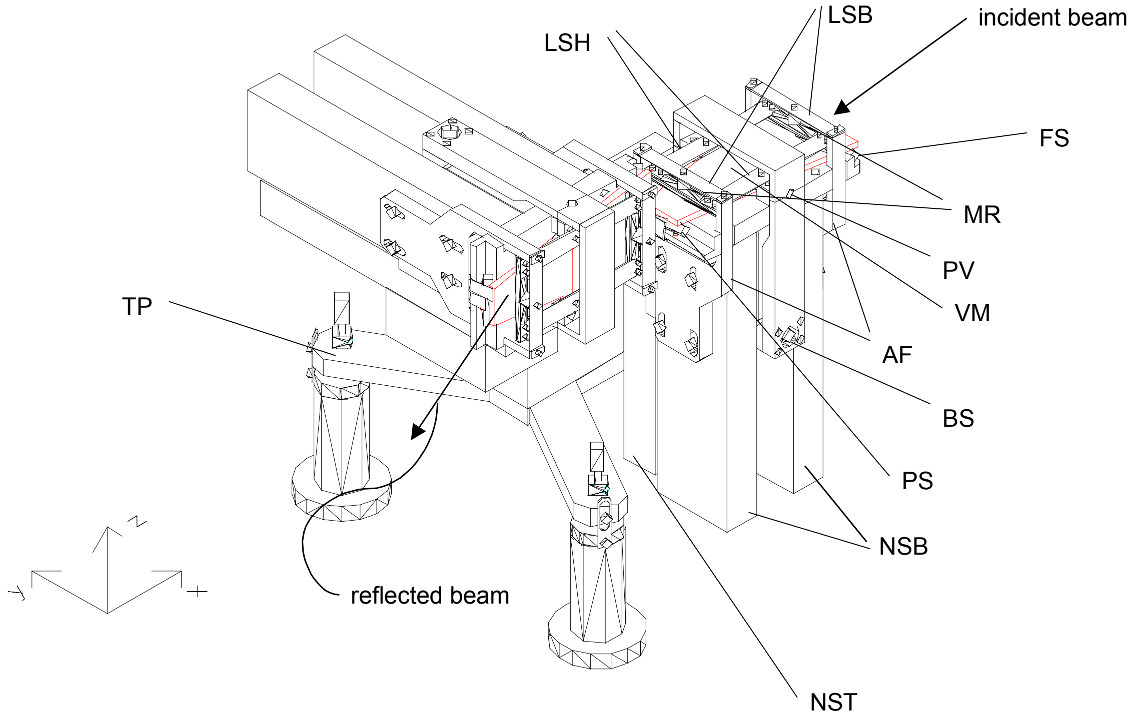

Figure 28. The vertical (right) and horizontal (left) mirror of the Kirkpatrick-Baez focusing system, which are positioned on a tripod.

The trapezoidal shaped float glass mirror (VM) has a length of 100 mm and a thickness of ~ 3 mm. The mirrors' widths at the larger and smaller end are 50 mm and 20 mm, respectively. A coating of 100 Å chromium and 400 Å gold with a width of ~ 10 mm stretches along the centerline. At its ends, the mirror is situated on 2 stainless steel rods (FS, PS). One of the rods is fixed (FS) and the other is located on a small dowel pin allowing it to pivot (PS). This permits the mirror to twist and relieve stress while the bending forces are applied. The bending forces are introduced with 2 *Newport* stepping motor translation stages[55] (NSB) with aluminum forks (AF) attached to their carriages. When the translation stages are actuated, the aluminum forks introduce bending forces to the mirror via copper leaf springs (LSB), load cell dummies (load cells can be added if desired) and movable rods (MR). The movable rods are held in place by leaf springs (LSH). The movable rods (MR) have a milled channel of 1.5 mm x 1 mm, which is located directly above the reflecting surface of the mirror. This allows the reflected beam to pass through the system, which is indicated in Figure 28 by an arrow. The *Newport* translation stages (NSB) are independently controlled, allowing the mirror to achieve the desired elliptic figure. In addition, the fine resolution of the translation stages, combined with the leaf springs' "gear reducer" mechanism, provide sufficient resolution to fine-tune the mirrors' shape to the elliptical shape. Tilting of the mirror to change the incident angle of the incident beam is realized by pivoting the mirror around the flex pivot[56] (PV). It utilizes a *MicroMo* stepping motor[57] rotating an eccentric camshaft, which is positioned below the mirror base plate and hence, tightly connected to the rotatable part of the bender mechanism. The eccentric cam is spring

---

[55] MFN08PP, Newport Corporation, 1791 Deere Ave., Irvine, CA 92606

[56] 3/16", 0.0473 Lb-IN/degree, Lucas Aerospace Power Transmission Corporation, 211-T. Seward Ave., P.O. Box 457, Utica, NY 13503

[57] AM1524-AO25-12.5-0.7+15/8,141:1, MicroMo Electronics, Inc., 14881 Evergreen Avenue, Clearwater, FL 33762-3008

loaded and pushed against a stationary bar. When actuating the *MicroMo* stepping motor, the cam pushes itself off the stationary push bar and tilts the mirror. The linearity and resolution of both tilt drives were measured using a micrometer screw. The results indicate a linear range of 12 mrad and a resolution of 35 μrad. In addition, a *Baumer Electric* precision limit switch[58] (BS) is installed in the system, which yields the "home" position (equal to 0° grazing angle) of the tilt drive. To execute the translation along the surface normal of the mirror, a *Newport* translation stage (NST) is installed. In the given coordinate system, the vertical focusing mirror can be moved along the z-axis and the horizontal focusing mirror along the y-axis. Further details on the performance of this system have been reported previously [15, 63].

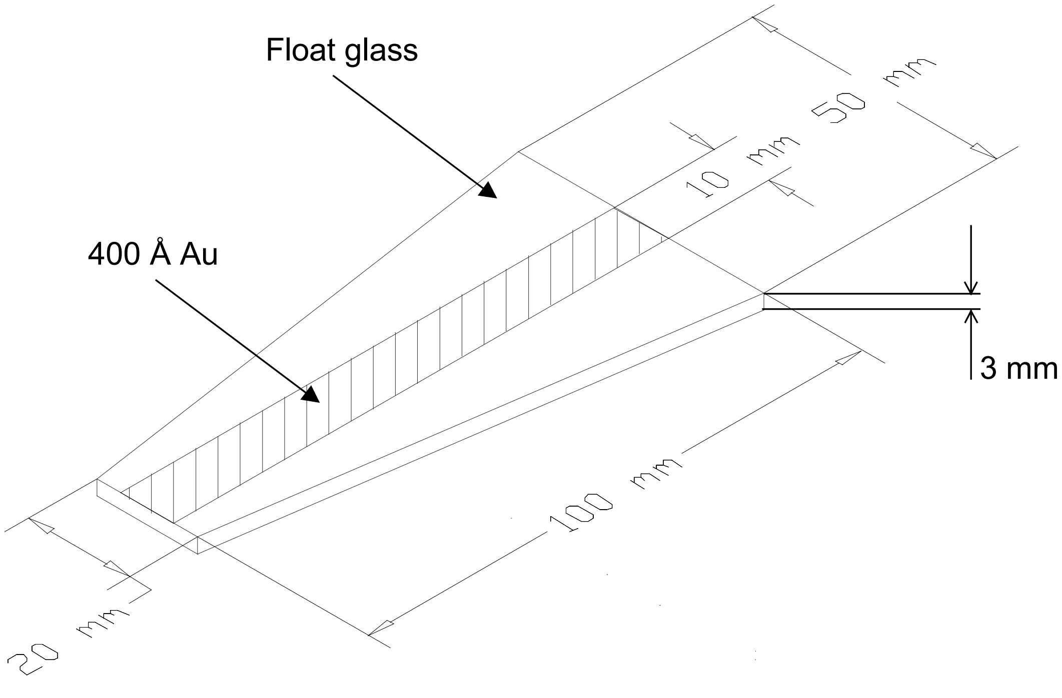

Figure 29. The dimension of the float glass mirror with a coating of 400 Å gold along the centerline.

5.1.5 Maximizing the focused photon flux on the sample

In this chapter, a simple qualitative model was designed, which addresses the issue of maximizing the incidence total photon flux on the sample. As the grazing angle is increased, the acceptance of the Kirkpatrick-Baez focusing system increases and the mirrors collect more incident radiation. Conversely, for a fixed photon energy as the grazing angle increases the reflectivity decreases. The latter is presented in Figure 30, in which the reflectivity of gold as a function of grazing angle for photon energies in the range of 2000 eV to 12000 eV is shown. In principle, there should be a trade off between maximizing the acceptance of the KB-system and having maximum reflectivity of the mirror coating material.

---

[58] Com H75/80, Baumer Electric, Ltd., 122 Spring Street, Southington, CT 06489

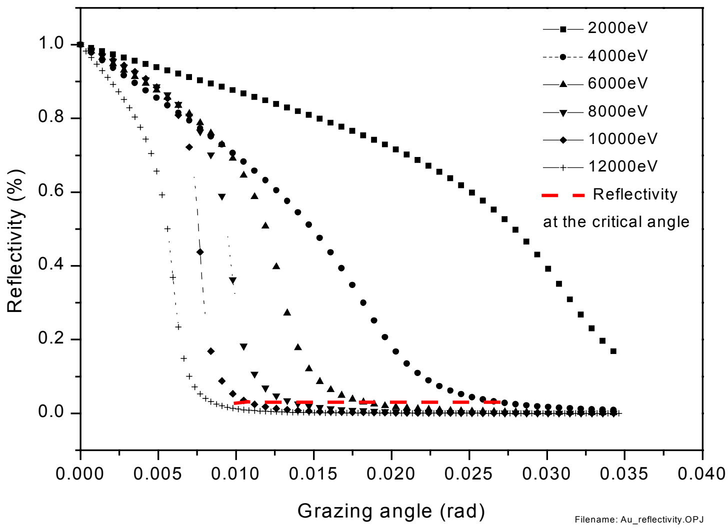

Figure 30. The reflectivity of gold as a function of grazing angle for photon energies of 2000 eV, 4000 eV, 6000 eV, 8000 eV, 10000 eV, and 12000 eV. The dashed line indicates the reflectivity at the critical angle, which is only ~ 3%.

The critical angle θ_{crit} for a given material can be expressed according to Eqn. (25). Figure 31 presents critical angle θ_{crit} of gold in the photon energy range of 1000 eV to 12000 eV. Of particular significance for the present work is the sharp decrease in critical angle over the photon energy range of interest for this experimental end-station (2000 eV to 5000 eV). This suggests that proper selection of the grazing angle θ_{graz} might have a significant effect on the photon flux.

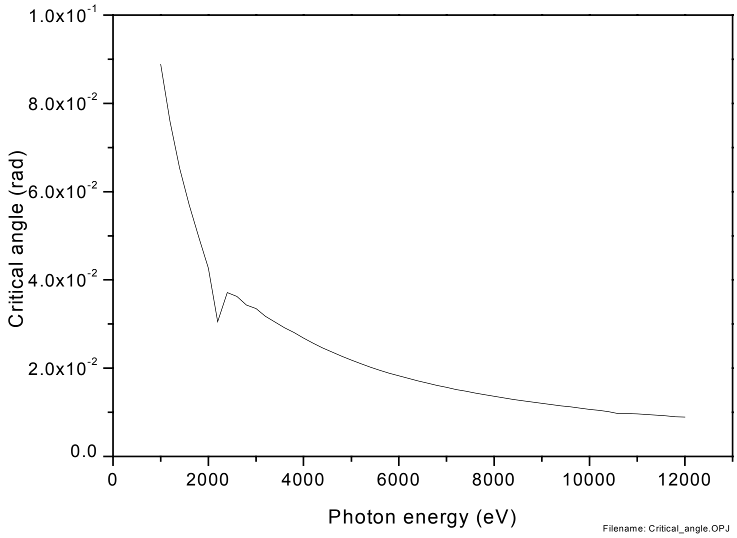

Figure 31. The critical angle for gold with a density ρ_{gold}=18.85 g/cm^3, calculated by Eqn. (26), as function of incident photon energy.

For the qualitative model, the acceptance of the Kirkpatrick-Baez system (horizontal and vertical mirror) was calculated and multiplied by the square of the reflectivity (to account for the double reflection) for the appropriate grazing angle. Hence, the photon flux at the sample is related to this product as

$$\text{photon flux} \propto \text{acceptance} \cdot \text{reflectivity}^2 . \tag{27}$$

In order to determine the acceptance, a total mirror length of l=100 mm for each KB-mirror and a range of grazing angles 0 mrad to 15 mrad were used. The reflectivity for gold for the corresponding incident photon energies can be found elsewhere [53]. The results are shown in Figure 32.

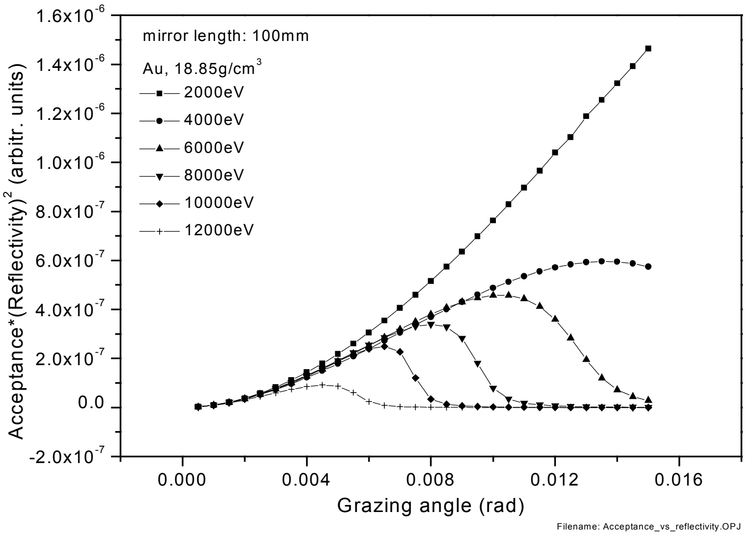

Figure 32. The product of the acceptance and the square of the reflectivity as a function of photon energy.

It can be observed that for a low photon energy such as 2000 eV (solid square), significant gains in total photon flux can be obtained by enlarging the grazing angle. In addition, a comparison of the location of the total peak fluxes in Figure 32 and the values for the critical angle in Figure 31 show clearly that the total peak fluxes are at a much smaller grazing angle than the critical angle. Therefore, it is feasible, depending on incident photon energy, to stay away from the critical angle by a factor of ~ 2. Moreover, intensity gains are achieved by working at lower photon energies. For instance, at 2000 eV the user gains a factor of ~ 6 in intensity compared to working at 10000 eV. This is a major advantage of the Kirkpatrick-Baez focusing system and makes working at lower photon energies so attractive.

5.2 Theoretical performance of the Kirkpatrick-Baez focusing system based on ray-tracing simulations

Detailed ray-tracing simulations using *Shadow* [48] to characterize the performance of the Kirkpatrick-Baez focusing system in the ANL/CAMD microprobe beamline are described in the following 2 sections. This theoretical data will be used to qualify and interpret the experimental data. At first in section 5.2.1 the appropriate bending magnet source is created, followed by the investigation of the focal spot size as a function of grazing angle on the focusing mirror. Section 5.2.2 addresses the effect of typical defects such as deviations from the ideal elliptical mirror figure on the focal spot size.

5.2.1 The CAMD source size and the focal spot sizes as a function of incidence angle

To simulate the appropriate CAMD bending magnet source, input parameters and procedures outlined by Morikawa [68] were used and interpolated for a ring energy of 1.3 GeV. The white source generated by *Shadow* with horizontal and vertical source sizes σ_x, σ_z of 831 μm and 187 μm, respectively, is shown in Cartesian coordinates in Figure 33.

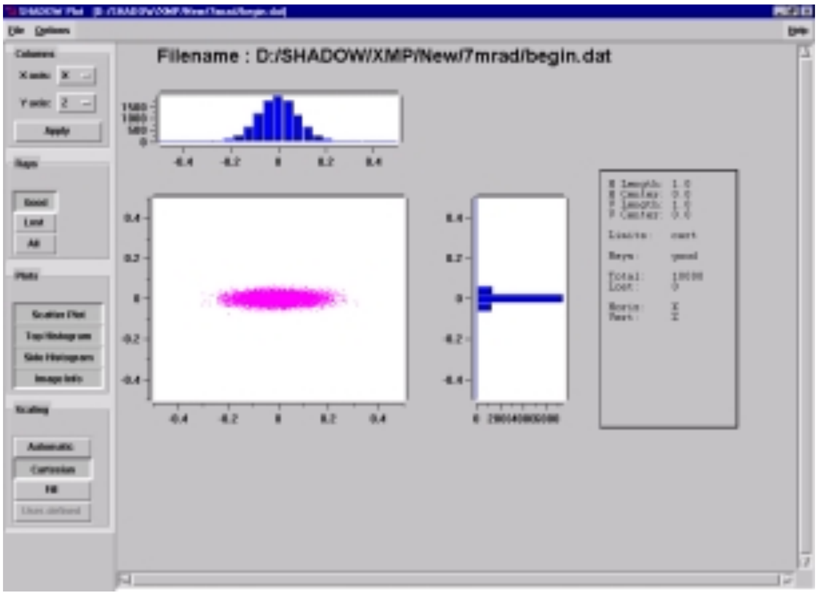
Filename : D:/SHADOW/XMP/New/7mrad/begin.dat

Figure 33. The white source at bending magnet 5A. The vertical and horizontal source sizes σ_x and σ_z are 831 μm and 187 μm, respectively.

Subsequently, the effect of various incidence angles on the horizontal and vertical focal spot size was simulated. The physical set-up of the beamline and the end-station in terms of source-mirror distances and mirror-focal point distances, mirror orientation angles and mirror incidence angles were also given to *Shadow*, allowing it to internally vary the geometrical parameters (a, b, and e) of the elliptical mirror. Table 1 shows the ray-tracing results.

Table 1. The focal spot sizes and the geometrical paramters of the elliptical horizontal and vertical focusing mirror.

Grazing angle (mrad)	Horizontal focus σ_x (µm)	Vertical focus σ_z (µm)	Horizontal mirror		Vertical mirror	
			Major axis a (cm)	Minor axis b (cm)	Major axis a (cm)	Minor axis b (cm)
1	-	-	-	-	-	-
3	11.8	5.4	470	0.35	470	0.46
5	13.1	4.9	470	0.59	470	0.77
7	13.4	5.2	470	0.82	470	1.08
9	12.7	4.9	470	1.06	470	1.39
11	12.5	4.9	470	1.29	470	1.69
13	12.1	5.0	470	1.53	470	2.00
15	12.2	5.0	470	1.77	470	2.31

As expected, the horizontal and vertical focal spot sizes as a function of angle are almost identical. The average horizontal and vertical focal spot sizes σ_{xF}, σ_{zF}, generated by *Shadow* are 12.5 µm and 5.0 µm, respectively. These results are in good agreement with the theoretical horizontal and vertical focal spot size σ_{xF}, σ_{zF} of 13.6 µm and 5.3 µm, based on CAMD source size and the horizontal and vertical demagnification of 61 and 35, respectively (refer to section 5.1.1). Minor deviations are due to statistical errors.

The major axis of both mirrors are fixed at 470 cm, since they are simply determined by the geometry of the optical set-up (refer to Eqn. (17)), whereas the minor axis b is linearly increasing with the increasing grazing angle (refer to Eqn. (18), (19)).

5.2.2 The focal spot sizes as a function of the measured slope errors

As pointed out in section 5.1.1, the rms slope error of the mirror, giving the deviation from the ideal elliptical mirror figure, leads to an increase of the theoretical achievable focal spot size. Hence, the intrinsic slope error of both mirrors, measured in section 5.1.2, was introduced into the ray-tracing calculations to quantitatively determine the impact on the focus. In order to be able to compare the quantitative theoretical ray-tracing results with the experimental performance, presented in section 5.3, a grazing angle for the vertical and the horizontal focusing mirror of 7 mrad was chosen.

Shadow requires as input values wavelength, amplitude and phase of the slope error, which can be taken directly from the slope error or after the integration of the slope error from the resulting height profile. The software of the Long-Trace-Profiler *WLTP 1.1* provides both data sets. The height data of the vertical and horizontal mirror, shown in Figure 34 and Figure

35 respectively, were used to extract wavelength, amplitude and phase as input values for *Shadow*.

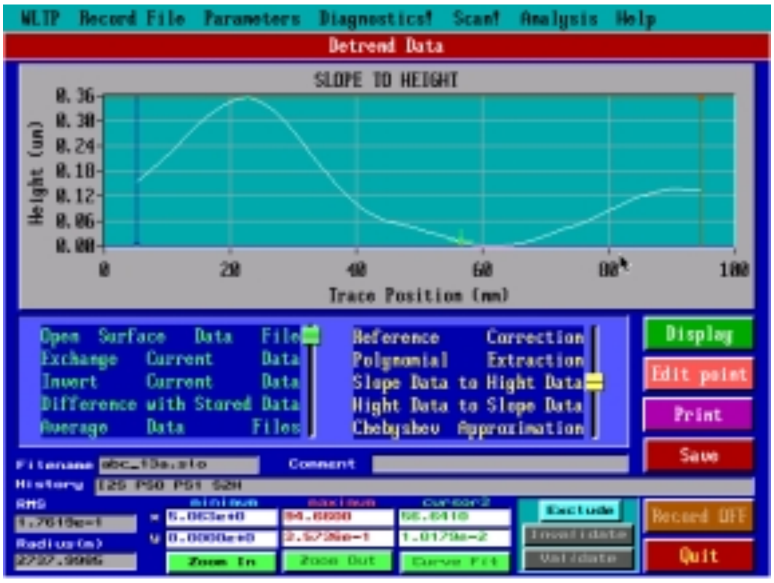

Figure 34. The height data versus trace position of the vertical focusing mirror with a rms slope error $\sigma_{\mathrm{Slope,v}} = 9.5\ \mu\mathrm{rad}$.

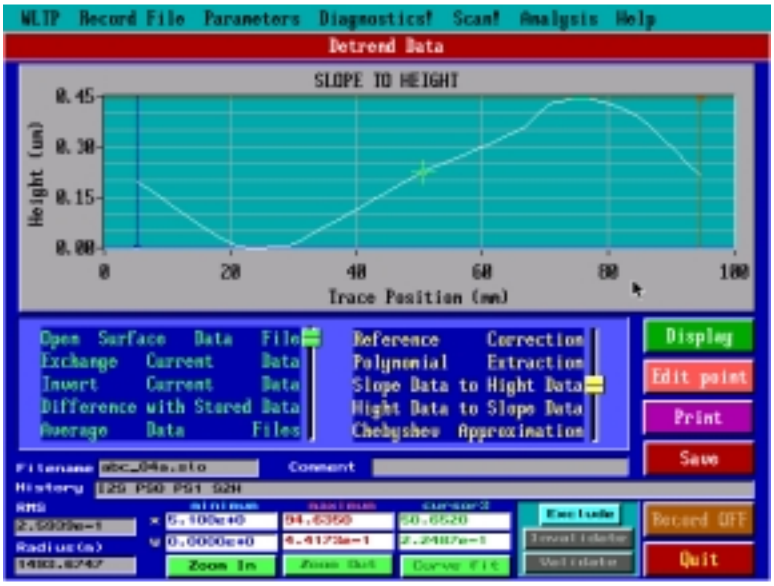

Figure 35. The height data versus trace position of the horizontal focusing mirror with a rms slope error $\sigma_{\mathrm{Slope,h}} = 10.7\ \mu\mathrm{rad}$

The amplitudes are easily established from Figure 34 and Figure 35 and result in 18 µm and 22.5 µm for the vertical and horizontal mirror, respectively. On the other hand, it was more difficult to determine the wavelength of the height data and therefore, a wavelength range between 5.0 cm and 11 cm was established and used as input values. The phase was set to 0 for all ray-tracing simulations.

Table 2. The vertical and horizontal focal spot sizes as a function of slope error wavelength. The theoretical horizontal and vertical focal spot sizes are σ_{xF}=5 µm and σ_{zF}=12.5 µm, respectively.

Wave-length λ_{Slope} (cm)	Horizontal focal spot size σ_{xF} (µm) with slope error from *Shadow*	Vertical focal spot size σ_{zF} (µm) with slope error from *Shadow*
5.0	14.7	9.9
5.5	14.5	9.3
6.0	14.3	8.5
6.5	14.1	7.9
7.0	13.9	7.5
7.5	13.8	7.2
8.0	13.7	7.0
8.5	13.7	6.8
9.0	13.6	6.7
9.5	13.6	6.6
10.0	13.6	6.5
10.5	13.6	6.4
11.0	13.5	6.3

The results of the ray-tracing simulations are shown in Table 2. The effect of the slope error wavelength on the vertical and horizontal mirror can be seen in column 2 and column 3, respectively. The values for the horizontal mirror are only slightly higher than those obtained by ray-tracing without including the slope error (σ_{xF}=12.5 µm). Thus, the slope error has most likely no effect on the horizontal focal spot size. However, looking at the vertical focal spot size σ_{zF}, the values are up to a factor of ~ 1.8 times larger than those disregarding the slope error (σ_{zF}=5.0 µm). Therefore, the slope error of the vertical mirror has to be considered as a critical parameter on the vertical focal spot size.

5.3 Experimental performance of the Kirkpatrick-Baez focusing system

This chapter will present some experimental results. The overall performance of the Kirkpatrick-Baez focusing system will be characterized by the experimental values, by the theoretical demagnification (section 5.1), and by the ray-tracing results (section 5.2).

The characterization of the horizontal and vertical focal spot size as well as the intensity distribution of the focal spot by acquiring data in transmission are depicted in section 5.3.1. This is followed by section 5.3.2 in which the modulation transfer functions are measured as a test of system resolution. Finally in section 5.3.3 the incident photon flux at the point of the sample in the low energy region will be shown.

5.3.1 The focal spot sizes in transmission

The Kirkpatrick-Baez focusing system was horizontally and vertically focused at a grazing angle of 7 mrad and the focal spot sizes were measured in transmission by performing knife-edge scans in the vertical and horizontal direction. 2 platinum foils with thickness' of 25 µm were therefore scanned across the focused white beam while acquiring the intensity of the transmitted white beam with a photo-diode.

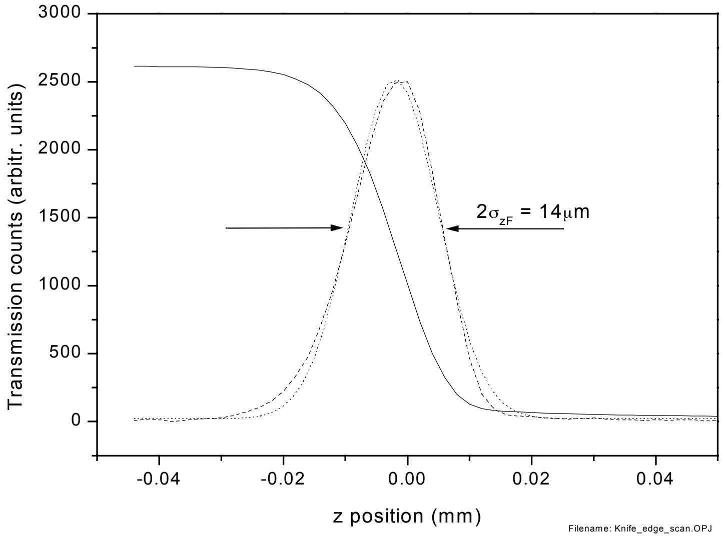

Figure 36. The vertical Pt knife-edge scan (solid line), its derivative (dashed line), and the Gaussian fit of the derivative (dotted line) yield the vertical focal spot size σ_{zF}=7 µm.

In Figure 36 the solid line represents the Pt knife-edge scan in the vertical direction. As the Pt knife-edge is moved into the beam, the intensity of the transmitted beam decreases and finally reaches zero as the knife-edge fully blocks the focused beam. The derivative yields the vertical intensity profile of the focal spot. Consequently, the derivative is fitted with a Gaussian and yields the vertical focal spot size σ_{zF} of 7 µm (16.5 µm FWHM).

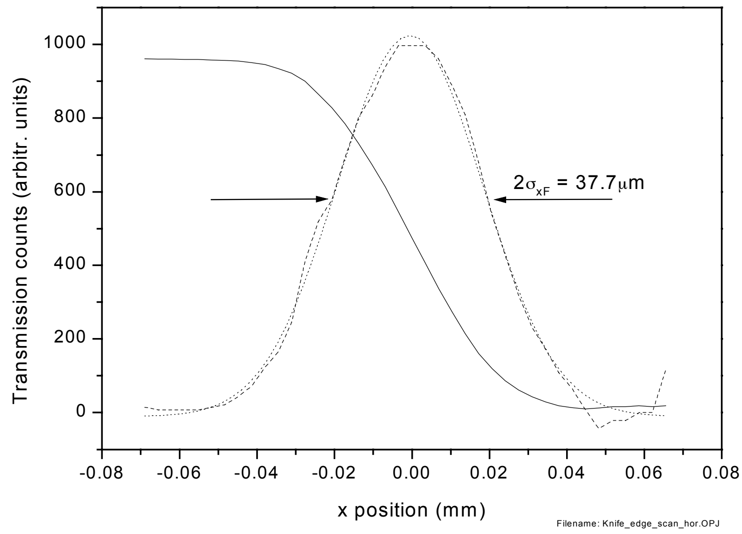

Figure 37. The horizontal Pt knife-edge scan (solid line), its derivative (dashed line), and the Gaussian fit of the derivative (dotted line) yield the horizontal focal spot size σ_{xF} of 18.8 μm.

In analogy to the vertical scan, the characterization of the horizontal focus was performed by scanning the Pt knife-edge in the horizontal direction across the focal spot. In the current experimental set-up (as can be seen in Figure 18 in section 4.1), the sample stage is positioned under 45° to the incident beam. Therefore, in order to determine the horizontal travel of the sample stage in the x-direction, a correction factor of sin(45°) was used. Figure 37 displays the corrected data of the horizontal knife-edge scan. The Gaussian fit of the derivative yields a horizontal spot size σ_{xF} of 18.8 μm (44.3 μm FWHM).

To be able to characterize the intensity distribution of the focus and hence identify possible surface roughness effects forming a halo around the focus, a 10 μm Pt pinhole was scanned in x- and z-direction through the focus. It was mounted on 50 μm kapton tape and attached to the sample stage and scanned in a 2-D scan (x, z) across the white focused beam. Once again, the transmitted white beam was measured using a photo-diode as a function of x, z. The translation ranges and the step sizes in x- and z-direction were 200μm, 2μm and 100μm, 2μm, respectively. The normalized transmitted intensity distribution of the focal spot, displayed as a surface plot and a contoured image are presented in Figure 38 and Figure 39, respectively.

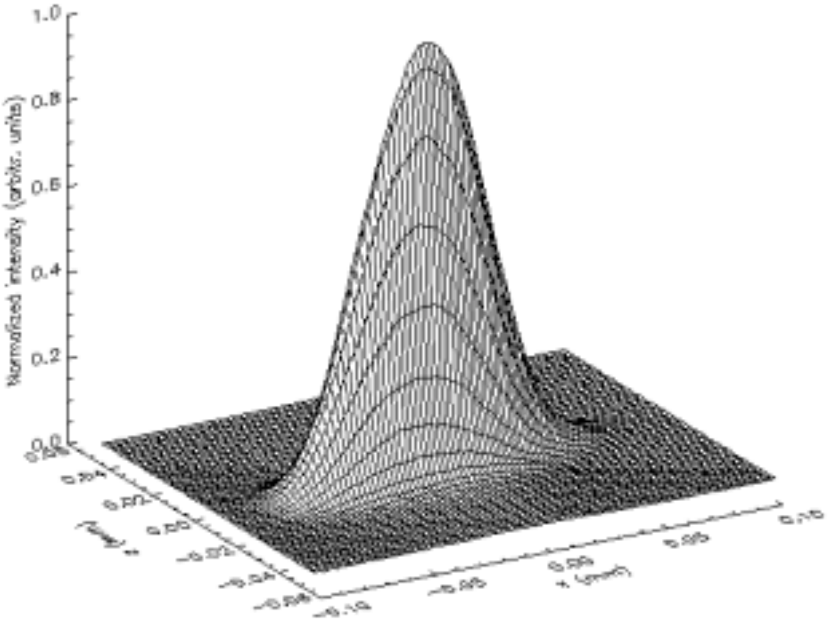

Figure 38. The normalized transmitted intensity distribution of the focal spot scanned with a 10 µm pinhole as surface plot. A smooth Gaussian distribution characterizes the focus and it can be clearly seen that there is no halo present.

The surface plot of the normalized intensity distribution of the focal spot in Figure 38 confirms that there is no halo around the focal spot. Hence, the surface roughness of the float glass mirrors is negligible.

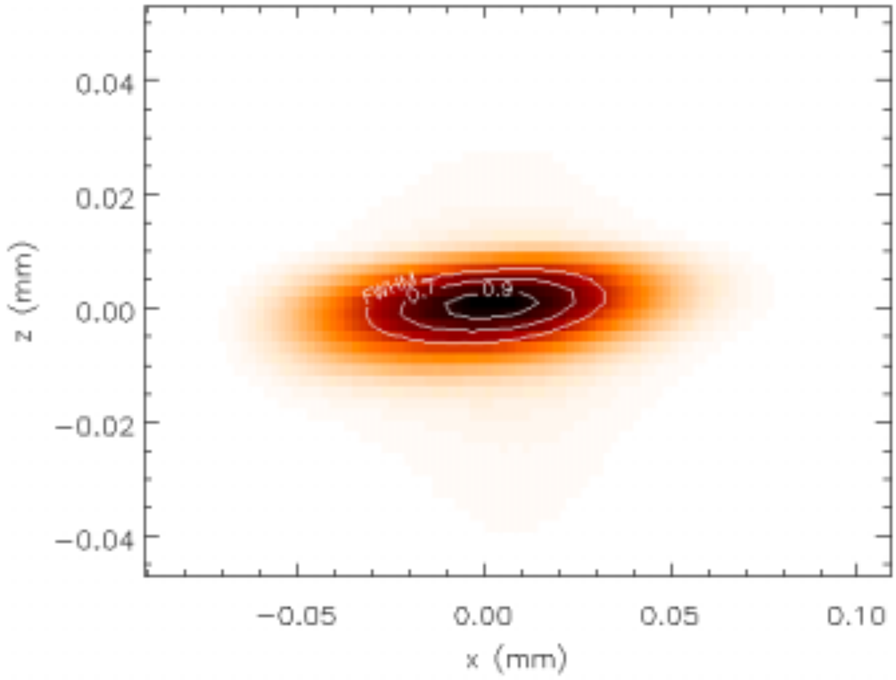

Figure 39. The normalized transmitted intensity distribution of the focal spot scanned with a 10 µm pinhole is presented as a contour plot. The 3 contour levels indicate 90%, 70%, and 50% (FWHM) transmitted intensity.

On the other hand, Figure 39 illustrates well the difference in size of the horizontal and vertical focal spot (σ_{xF}=18.8 µm, σ_{zF}=7 µm) determined by the horizontal (σ_z=831µm) and vertical (σ_z=187µm) CAMD source size (compare to Figure 33). Despite the fact that the anamorphosis[59] of the KB-system (M_{DH}=61, M_{DV}=35) is beneficial to the CAMD source size [62, 79], the focal spot is nevertheless ~ 2.6 times as large in the horizontal direction than it is in the vertical direction.

Table 3. Summary of the focal spot sizes based on source size and demagnification, ray-tracing results and the experimental results.

	Geometric Optics	Ray-tracing results without slope errors	Experimental results
Horizontal focal spot size are σ_{xF} (µm)	13.6	12.5	18.8
Vertical focal spot size are σ_{zF} (µm)	5.3	5.0	7.0

Table 3 presents a summary of the horizontal and vertical focal spot sizes obtained by geometric optics (column 2), by ray-tracing calculations (column 3) and by experimental results (column 4). The theoretical results in column 2 and 3 are in close agreement. However, it can be seen that the horizontal and the vertical experimental results have a deviation of ~ 50% from the theoretical values. Because of the fact that the horizontal and vertical experimental values are deviating, it is unlikely that the rms slope errors cause the extended focal spot sizes. Thus, it is presumed that the horizontal and vertical CAMD source sizes are actually larger than the interpolated theoretical source sizes (refer to section 5.2.1). Based on the fact that there is no halo present around the focal spot, it can be concluded that rms surface roughness is negligible and that overall float glass mirrors are performing very well in dynamically x-ray focusing in the CAMD/ANL microprobe beamline.

5.3.2 The resolution in fluorescence mode

In order to describe quantitatively the system resolution in fluorescence mode, it is necessary to determine the optical transfer function (OTF) by scanning an incoherently illuminated sinusoidal grating [80, 81]. The 1-dimensional spatial frequency-dependent optical transfer function (OTF) D(R) can be given as

$$D(R) = T(R) \cdot e^{i \cdot \theta(R)}, \tag{28}$$

where T(R) is the modulation transfer function (MTF) and Θ(R) is the phase transfer function (PTF) [80]. The latter represents the commensurate relative phase shift of the image

---

[59] Anamorphosis: a distorted optical image; producing an intentional distortion by unequal magnification along perpendicular axes of an image.

for the spatial frequency R compared to the position of image for the spatial frequency R=0. In a centered optical system, the PTF=0 [67]. This leads then to

$$D(R) = T(R). \tag{29}$$

The modulation transfer function is a measure of the reduction in modulation or contrast from object to image over the spatial frequency spectrum, in which the spatial frequency is defined as reciprocal value of the sinusoidal period length. The modulation transfer function T(R) is given by

$$T(R) \equiv \frac{I_{\max} - I_{\min}}{I_{\max} + I_{\min}}, \tag{30}$$

where $I_{\max}$ and $I_{\min}$ are the maximum and minimum intensities of the incoherently illuminated sinusoidal object. It is evident, that the T(R) is decreasing with increasing spatial frequency. The best achievable resolution of an optical system is determined by reciprocal spatial frequency at which T(R) is larger than 0. In the case that the spatial frequency R is equal to 0, then modulation transfer factor is set to 1.

The grating was produced at CAMD. Patterning a 5000 Å thick copper film on a 4” silicon wafer produced a line and space pattern with starting line widths of 5 µm, 7 µm, 9 µm up to 101 µm [82]. The Si wafer with the Cu grating was then cut to size. The white beam was focused at a grazing angle of 7 mrad. The focal spot sizes (σ_{xF}, σ_{zF}) were measured with knife-edge scans, as previously described in section 5.3.1, to 18.6 µm x 7.9 µm, respectively. Subsequently, the Cu grating was mounted horizontally on the sample stage and scanned vertically over its entire length in a step size of 1 µm through the focal spot while collecting the Cu K α fluorescence with the energy-dispersive Ge-detector for an integration time of 1 s. Then, the grating was vertically mounted and a similar scan was performed horizontally. In Figure 40 and Figure 41, the vertical and horizontal scans of the Cu grating are presented.

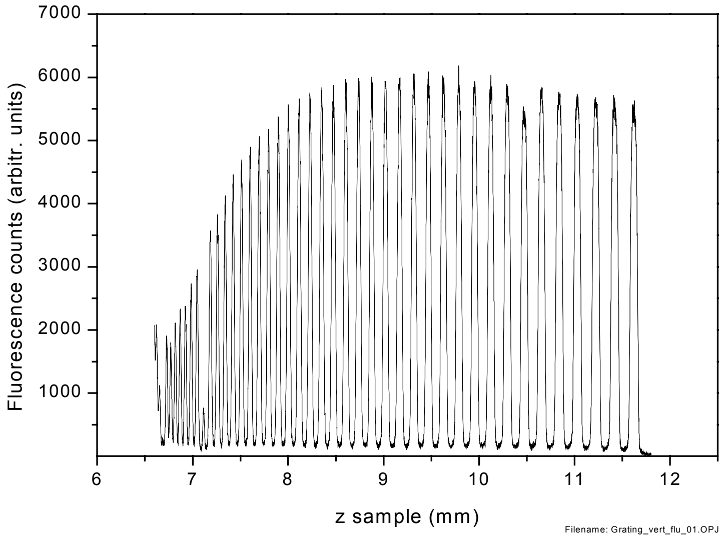

Figure 40. The Cu grating was scanned vertically through the focal spot collecting the Cu K α characteristic x-ray being emitted by the Cu lines of the grating.

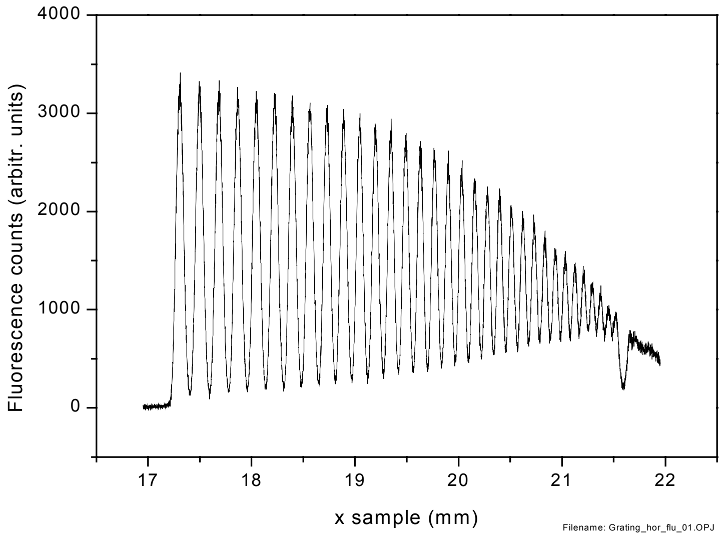

Figure 41. The horizontal scan of the Cu grating though the focal spot.

By comparing the raw peak-to-valley data as a function of position in Figure 40 and Figure 41, it can be seen that the vertical focus shown in Figure 40 has a better resolution than the horizontal focus in Figure 41. The low-count peaks, at z sample ~ 7.2 mm in Figure 40 and at x sample ~ 21.6 mm in Figure 41, are due to a flaw in the Cu grating. At this point, the grating line width is ~ 35 μm.

In order to establish the horizontal and vertical MTFs, the raw fluorescence intensity data from Figure 40 and Figure 41 were fitted with multiple Gaussian peaks. The maximum and minimum intensity to each peak was extracted and correlated to the appropriate Cu grating line width, creating the MTF T(R) according to Eqn. (30).

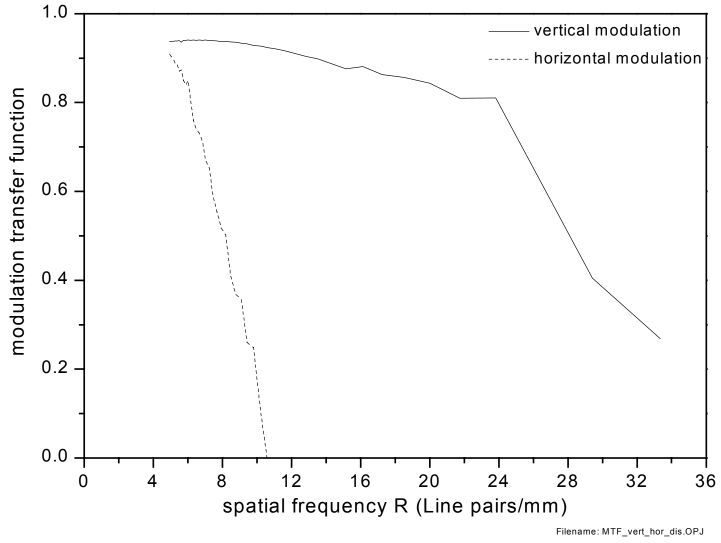

Figure 42. The modulation transfer function in fluorescence mode for the vertical (solid line) and horizontal (dashed line) Cu grating scans.

Figure 42 summarizes the results of the calculation of the vertical and horizontal modulation transfer function in fluorescence mode. The vertical modulation transfer function exhibits a low contrast of ~ 26% at a spatial frequency R of ~ 33 line pairs/mm (15 µm line width). But for 25 line pairs/mm, which is equal to 20 µm line width, a high contrast of ~ 73% has been achieved. In addition, it can be observed that the vertical MTF does not disappear, which is due to the fact that the Cu grating was only well defined to a line and space width of ~ 10 µm.

On the other hand, the horizontal MTF displays a poor contrast of ~ 10% at 10 line pairs/mm (49 µm line width). Overall, the horizontal and vertical modular transfer functions are in very good agreement with the full-width-half-maximum (FWHM) horizontal and vertical focal spot sizes (43.8 µm x 18.6 µm) established before the experiment.

5.3.3 Photon flux measurements

Finally, photon flux measurements were performed with the focused KB-system at an incident angle of 7 mrad. The ring energy was 1.3 GeV and the average ring current was ~ 100 mA. Prior to the data acquisition, harmonic rejection was performed by detuning the Si(111) crystals approximately 50% of the peak intensity of the rocking curve. The photon flux was measured with a *Hamamatsu* GaAsP photo-diode, which is optically sealed with 2 pieces of ~ 12.5 µm (1/2 mil) aluminized *Mylar* film and positioned behind the sample stage. There was no sample mounted. In this way, the incident photon flux on the sample in the energy region of 2500 eV to 5900 eV could be determined. A 12.5 µm kapton window was used to separate the high vacuum of the double crystal monochromator from the helium atmosphere in the end-station.

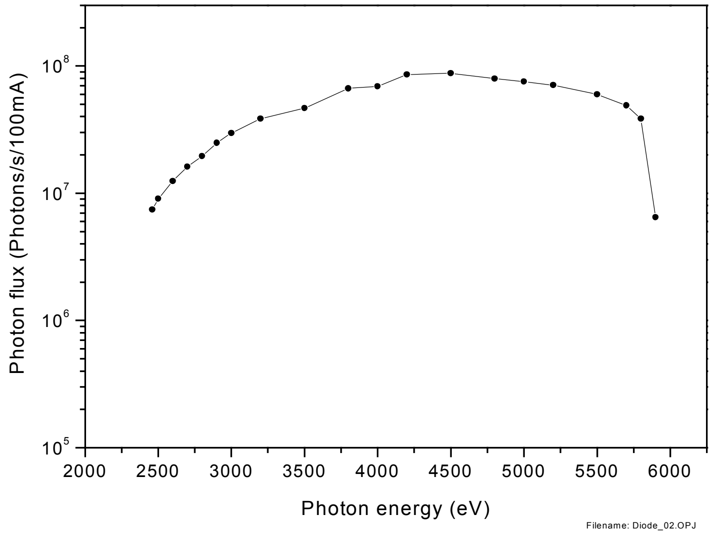

Figure 43. The focused photon flux at the sample position for the low photon energy range of 2500 eV to 6000 eV.

In Figure 43, the measured incident photon flux at the sample position is presented. Here, the spectral bandwidth is determined by the double crystal monochromator's bandpass (see section 3.3.2). The following equation,

$$Flux\left[\frac{Photons}{s\cdot 100mA}\right]=\frac{I_{Diode}\left[\frac{Coulomb}{s}\right]\Big/100mA}{1.602\cdot 10^{-19}\left[\frac{Coulomb}{electron}\right]\cdot QE\left(E_{Photon}\right)[\%]}, \tag{31}$$

was applied to obtain the photon flux per second per 100 mA. I_{Diode} is the diode current per 100 mA ring current in Coulomb per second and $QE(E_{Photon})$ is the quantum efficiency of the GaAsP photo-diode as a function of photon energy in %. The quantum efficiency was available up to 4000 eV [83] and beyond that, it was moderately approximated with 300%.

6 Experimental

In this chapter the sample preparation including the synthesis of the poly(hexadiene-1,3 sulfone) and the film preparation are presented. It is followed by a detailed description of the PHS exposure to white bending magnet radiation at beamline XRML3 at CAMD. Thereafter, the acquisition of the micro-spectroscopy and spectro-microscopy data at the sulfur K-edge (2472 eV) is described.

6.1 Poly(hexadiene-1,3 sulfone) synthesis and film preparation

The synthesis of the poly(hexadiene-1,3 sulfone), PHS, is based on a co-polymerization between SO_2 and 1,3-hexadiene and is described previously [5]. PHS films were produced with a 30% w/w solution[60] of the polymer in nitromethane. The solution was mixed for ~ 24 hr with a magnetic stirrer at room temperature. Approximately 5 ml of the solution was poured on the center of a 4” silicon wafer and spin-coated with the following parameters: ramp from 0 to 1500 rpm in 20 s, hold at 1500 rpm for 30 s. The solution was baked at 100° C for 15 min. After the baking process, the thickness of the sample on the Si wafer was measured by ellipsometry on a *Nanometrics* Model 210xp spectrophotometer[61] using a refractive index of 1.51. The thickness measured was to ~ 22 µm. To remove the film from the wafer, the wafer was placed onto a cool metal surface. As the Silicon wafer cools rapidly, it contracts and causes the film to lose adhesion and peel off.

6.2 Exposure process at the CAMD XRML3 beamline

The exposures were conducted at the XRLM3 beamline at the Center for Advanced Microstructures and Devices (CAMD) [84]. XRLM3 is a white light beamline accepting 5 mrad of radiation emitted from a bending magnet. The beamline is terminated by a 125 µm beryllium window, which separates the filter and exposure chamber from the beamline. The PHS films were cut into pieces of ~ 5 mm x ~ 3 mm, each sandwiched between 2 pieces of 8 µm kapton foil, and mounted into precision milled PMMA cubes. The entire assembly was inserted into an aligned modified wafer holder, so that the PHS films lie in the plane of the synchrotron radiation (x-y plane). The wafer holder was mounted on the scanning stage in the exposure chamber. The schematic exposure geometry without the modified wafer holder is shown Figure 44.

---

[60] w/w is the ratio of the weight of the polymer divided by the weight of the solvent.

[61] Nanometrics, Inc., 310 De Guigne Drive, Sunnyvale, CA 94086

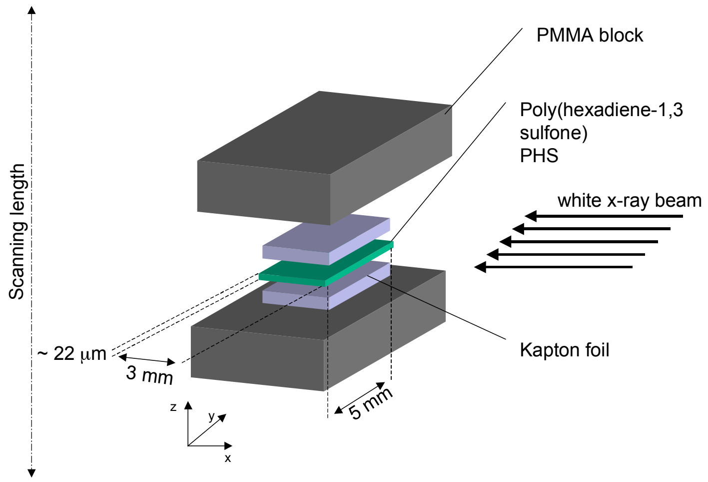

Figure 44. The geometry of the PHS exposures. The PHS film is sandwiched in between 2 8 µm kapton foils and mounted between 2 PMMA blocks.

To modify the top-to-bottom dose ratio of the exposures, aluminum filters with thickness' of 30 µm and 60 µm were mounted in the filter chamber and inserted before exposure. The exposure chamber was then evacuated and purged with helium to a pressure of ~ 100 torr. All sample exposures were conducted at a ring energy of 1.5 GeV. During the exposure the entire assembly holding the PHS film was continuously scanned in the vertical direction (z) through the white x-ray beam. The scanning length of the exposure was 1". The deposited doses for Al filter thickness of 30 µm and 60 µm are depicted in Figure 45.

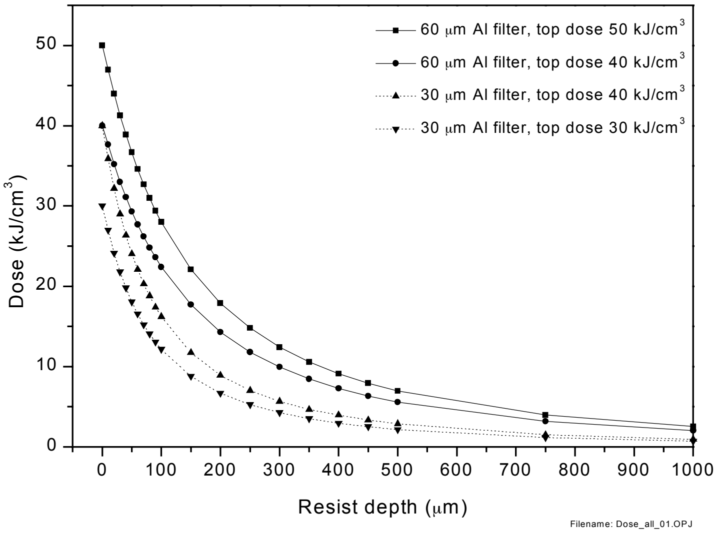

Figure 45. The calculated dose deposition as a function of depth in the range of 0 µm to 1000 µm.

6.3 Preparations for the microprobe measurements

After the exposures, the PHS films on 8 µm kapton (as mechanical support) are transferred on stainless steel sample holder frames and fixed with tape. The sample holder is mounted to the x-z-sample stage, so that the expected dose/depth profile is aligned with the z-axis (vertical) of the sample stage (refer to Figure 46).

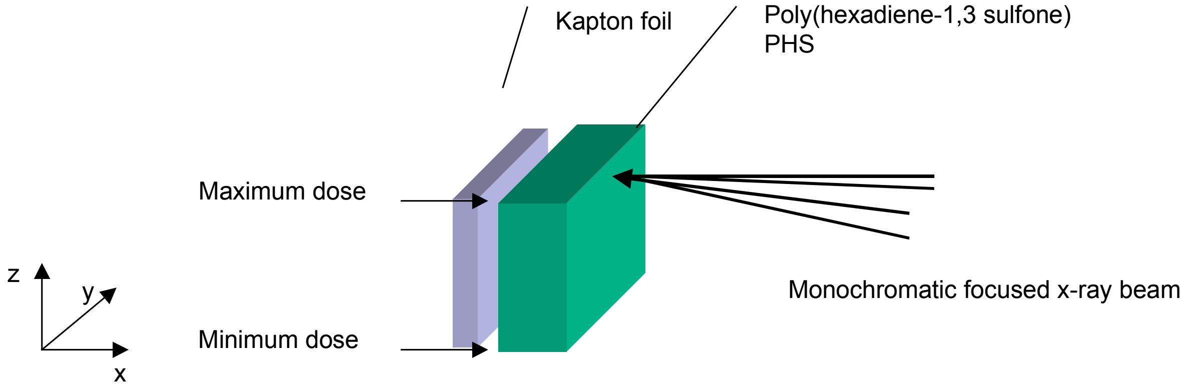

Figure 46. Schematic of the sample position on the x-z-sample stage in the microprobe setup. The XANES line scans were performed by scanning the PHS film on the 8 μm kapton along the z-axis. The fluorescence screen, the zinc sulfate ($ZnSO_4$), as well as the knife-edges are not indicated.

In addition to the PHS sample, a small piece of the *DuPont* fluorescence screen, a reference sample of zinc sulfate ($ZnSO_4$), and vertical and horizontal knife-edges are permanently mounted to the sample stage. After mounting the sample, the helium enclosure is closed and helium is flown for ~ 30 min until the intensity of the photo-diode rises and stabilizes. Prior to any data scan, the focal spot size and position are determined by performing vertical and horizontal knife-edge scans (as previously described in section 5.3.1). At this point, it should be mentioned that the focal spot size was well reproducible from one injection to another. Therefore, it was unnecessary to re-focus the mirrors during the experiments. However, the position of the focal spot changed frequently from one injection to the next (in particular in the horizontal), necessitating re-positioning of the sample.

6.4 Sulfur K-edge micro-spectroscopy/micro-XANES

The average focal spot size (FWHM) was ~ 45 μm (horizontal) x ~ 20 μm (vertical). Prior to the data acquisition, harmonic rejection was performed by detuning the Si(111) crystals approximately 50% of the peak intensity of the rocking curve. For the energy calibration of the DCM, the sharp white line of the zinc sulfate ($ZnSO_4$) was set to 2481.44 eV [9]. Micro x-ray absorption near-edge structure (micro-XANES) spectra were collected in transmission at the S K-edge at 2472 eV. They were acquired along a vertical line (z-axis line scan) collecting the transmitted intensity I with a photo-diode. For the measurement of the initial intensity I_0 an upstream ion chamber and the ring current were collected. For each sample, 3 micro-XANES line scans were performed with scanning lengths of 50 μm, 200 μm, and 1000 μm with step sizes of 5 μm, 10 μm, and 50 μm, respectively. The energy range of the XANES spectra was 2460 eV to 2520 eV with a step size of 0.2 eV and the integration time per pixel of 0.5 s. This leads to scanning times for micro-XANES line scans of 25 min to 50 min per scan. These numbers do not include any overhead, which is rather significant. The angular change to re-position the DCM from the end to the initial photon energy is ~ 1.8° and has to be done slowly in order not to lose motor steps or energy calibration. Typical total data acquisition times ranged between 1 hr and 2 hr per micro-XANES line scan. The *IDL* GUI control software allows the user to enter all the above given parameters and performs the

XANES line scan automatically. This convenient routine was added during the course of the experiments and eliminates possible operational errors by the user.

6.5 Sulfur K-edge spectro-microscopy

After the micro-XANES spectra of each PHS sample were acquired, the energetic peak location of the pre-edge peak was determined to 2472.5 eV and the spectro-microscopy image was collected. In addition, a spectro-microscopy image at 2515 eV, representing the background of the XANES spectrum, was collected for normalization purposes. The typical horizontal and vertical image size was 200 µm x 1000 µm with step size of 10 µm and 20 µm, respectively. The total acquisition time was ~ 1 hr.

7 Data analysis and discussion of the results

The chemical changes around the sulfur atom due to radiation-induced degradation are of high interest for the development of poly(hexadiene-1,3 sulfone) (PHS) as a potential x-ray resist. X-ray absorption near-edge structure (XANES) spectroscopy is able to identify various functional groups of sulfur created by radiation exposure. The functional groups can be identified based on the energy position and the intensity of the strong, well-resolved white lines in the S K-edge XANES spectra of reference compounds [10, 11, 35]. This procedure is commonly referred to as white line “fingerprinting”. Hence, reference compounds with different sulfur functional groups in various formal oxidation states (-2 to +6) were measured. These spectra provide a guide for the assignment of the spectral features in the sample spectrum based on the energetic positions of the sulfur white lines in the reference compounds. The reference compounds of methionine sulfide, methionine sulfoxide, unexposed poly(hexadiene-1,3 sulfone), and poly(sodium 4-styrenesulfonate) are shown in Figure 47.

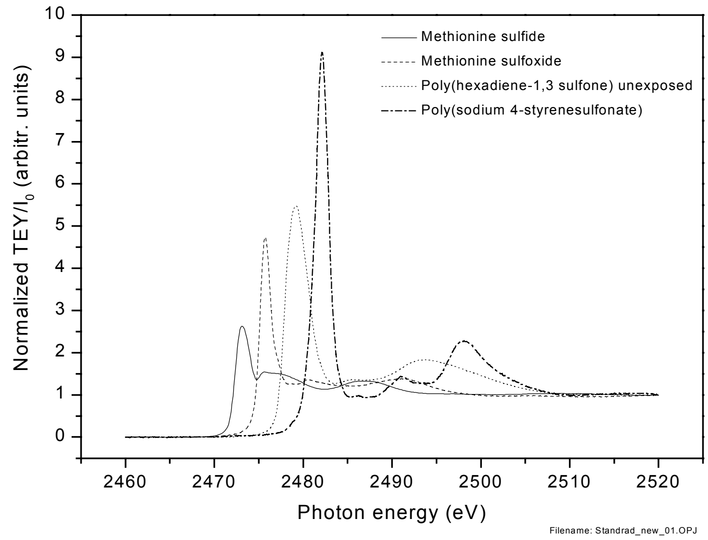

Figure 47. S K-edge x-ray absorption near-edge spectra of the reference compounds methionine sulfoxide, unexposed poly(hexadiene-1,3 sulfone), and poly(sodium 4-styrenesulfonate).

Figure 47 indicates clearly the energy shift as well as the intensity increase of the white line of the S K-edge XANES spectrum with increasing oxidation state of sulfur in the reference compounds. Here, the formal oxidation states of sulfur in methionine sulfide, methionine sulfoxide, unexposed poly(hexadiene-1,3 sulfone), and poly(sodium 4-styrenesulfonate) are -2, +2, +4, and +6, respectively. The chemical structures of the functional groups are presented in Figure 48.

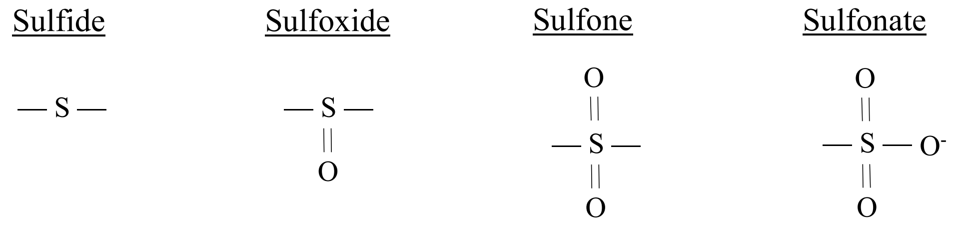

Figure 48. The structures of the functional groups of methionine sulfide, methionine sulfoxide, poly(hexadiene-1,3 sulfone) (PHS) and poly(sodium 4-styrenesulfonate).

The poly(hexadiene-1,3 sulfone) (PHS) samples had been exposed with different doses at the soft x-ray beamline XRLC1 and the hard x-ray beamline XRLM3, resulting in 2 different incident spectral exposure distributions. The S K-edge XANES spectra of the PHS samples were collected in total-electron-yield (TEY) [85], thereby only being surface sensitive. The spectra from the samples exposed at the soft x-ray beamline and the hard x-ray beamline are shown in Figure 49 and Figure 50, respectively.

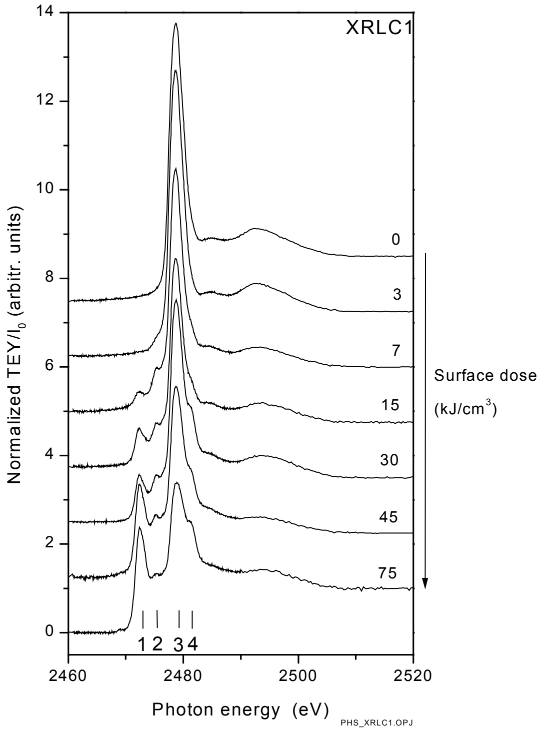

Figure 49. S K-edge XANES of PHS samples exposed at the soft x-ray lithography beamline XRLC1.

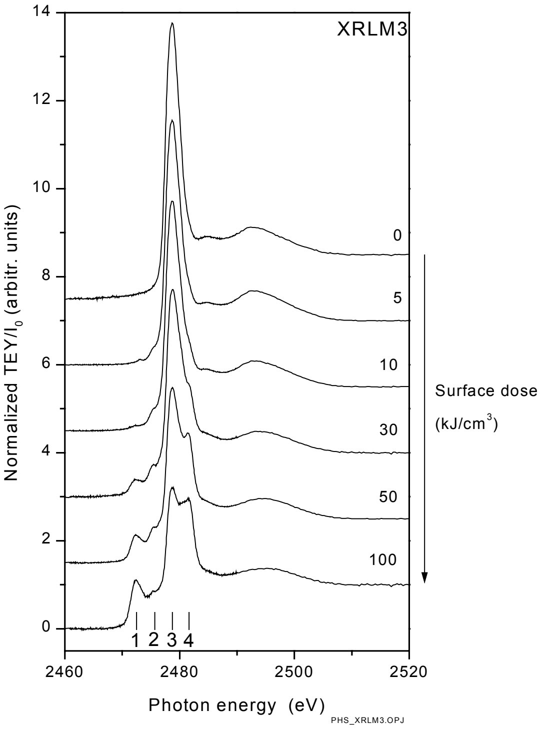

Figure 50. S K-edge XANES of PHS samples exposed at the hard x-ray micro-machining beamline XRLM3.

Each spectrum in Figure 49 and Figure 50 is labeled on the right hand side with its surface dose in kJ/cm^3, calculated for the energy absorbed in one absorption length of the polymer. Upon exposure strong changes occur in the sulfur environment. It can be observed that new dominant features appear in the spectra with increasing surface dose.

The main features in Figure 49 and Figure 50 are labeled 1 to 4. The energy positions of features 1 to 4, based on a calibration of the double crystal monochromator to the white line of zinc sulfate ($ZnS0_4$) at 2481.4 eV, are 2472.5 eV, 2475.5 eV, 2478.7 eV, and 2481.6 eV. Assignments to sulfur functional groups as well as characterization of the S-X bond type using the 1s→σ*(S-X) transition of peaks 1 to 4 will be made based on the reference compounds shown in Figure 47 and previously published literature [32, 86-88].

Peak number 1 at 2472.5 eV can be identified as representing the presence of an organic sulfide group as shown in Figure 47. Dezarnaud et al. as well as Hitchcock et al. attributed the white line in dimethyl sulfide to a 1s→σ*(S-C) transition, which can also be found at 2472.5 eV [87, 88].

In the same manner, peak number 2 at 2475.5 eV can be attributed to the presence of a sulfoxide group due to an identical energy position as the white line of methionine sulfoxide in Figure 47. Sze et al. located the white line of dimethyl sulfoxide at the same energy position [86]. Their determination of the S-X bond type showed that the 1s→σ*(S-X) transition has σ*(S-O) character as well as σ*(S-C) character.

Following peak number 3 at 2478.7 eV from the initial unexposed PHS sample in Figure 49 or Figure 50, it is conclusive that this is the sulfone peak. Hitchcock et al. determine the sulfone peak at the same energy position [32].

Peak number 4 located at 2481.6 eV indicates the presence of a more oxidized state of sulfur than the initial sulfone, which involves a main scission of a S-C bond. An organic sulfonate compound, poly(sodium 4-styrenesulfonate), was measured and produced a white line at 2481.7 eV. Hence, peak number 4 was attributed to the presence of sulfonate [14]. Table 4 gives a summary of the assignments with regard to the energy position, the sulfur functional group and the bond type of peaks 1 to 4.

Table 4. The peak identification of the radiation-induced functional groups in PHS.

Peak label	Energy position	Functional group	Bond type	Formal sulfur oxidation state	Ref.
1	2472.5	Sulfide	σ*(S-C)	-2	[88]
2	2475.5	Sulfoxide	σ*(S-C) or (σ*(S-O))	+2	[86]
3	2478.7	Sulfone (initial peak)	n.a.	+4	[32]
4	2481.6	Sulfonate	n.a.	+6	[14]

n.a. = not assigned

Beyond the fact that S K-edge XANES spectroscopy can provide the characterization of sulfur functional groups, S K-edge XANES has also been used as a non-destructive, quantitative tool for the determination of sulfur functional groups in organic and inorganic materials. In particular, the quantitative determination of major sulfur species in coal was reported extensively [10-12, 35-37]. The procedure consists of a nonlinear least squares fit, which uses linear combinations of normalized reference spectra to simulate the sample spectrum [13]. To perform the quantitative analysis, the software *WinXAS* was used [89]. It performs the nonlinear least squares fit of the sample S K-edge XANES spectrum according to

$$\mu_{\text{Sample}}\left(E_{\text{Photon}}\right) = \sum_{i} c_i \cdot \mu_{\text{Reference},i}\left(E_{\text{Photon}} + \Delta E_i\right) \tag{32}$$

where c_i is the fraction for the reference compound i and ΔE_i is the relative energy shift of the reference compound's XANES spectrum. The fitting range was set to 2460 eV to 2487.72 eV and the reference spectra shown in Figure 47 were used. Figure 51 and Figure 52 present examples of nonlinear least squares fits for 2 PHS sample spectra exposed with a surface dose of 30 kJ/cm^3. The sample spectra were previously shown in Figure 49 and Figure 50, respectively.

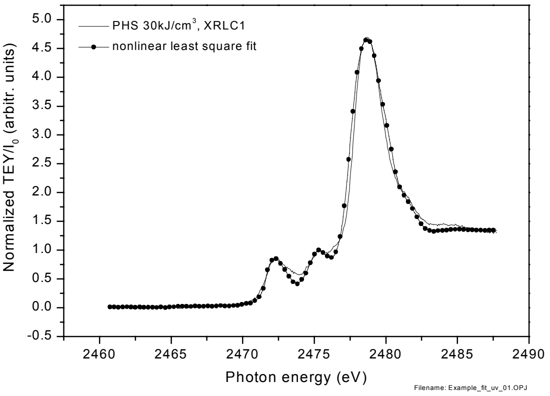

Figure 51. S K-edge XANES spectrum of a PHS sample exposed with a surface dose of 30 kJ/cm^3 at the XRLC1 beamline and the nonlinear least squares fit (circle) using the scaled reference compounds spectra.

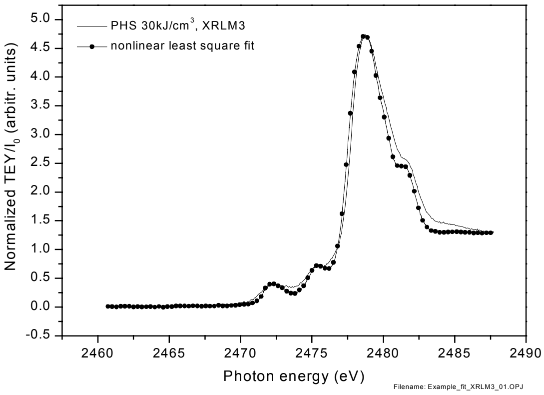

Figure 52. S K-edge XANES spectrum of a PHS sample exposed with a surface dose of 30 kJ/cm^3 at the XRLM3 beamline and the nonlinear least squares fit (circle) using the scaled reference compounds spectra.

Similarly, results by nonlinear least squares fitting were obtained for the remaining spectra in Figure 49 and Figure 50. The normalized fractions of the reference compounds methionine sulfide, methionine sulfoxide, poly(hexadiene-1,3 sulfone), and poly(sodium 4-styrenesulfonate) are shown as a function of surface dose in Figure 53 and Figure 54, indicating the radiation-induced production of the sulfur functional groups sulfide, sulfoxide, sulfone, and sulfonate, respectively. Figure 53 presents the fitting results for the PHS samples exposed at the soft ray beamline (XRLC1) and Figure 54 depicts the results obtained for PHS samples exposed at the hard x-ray beamline (XRLM3).

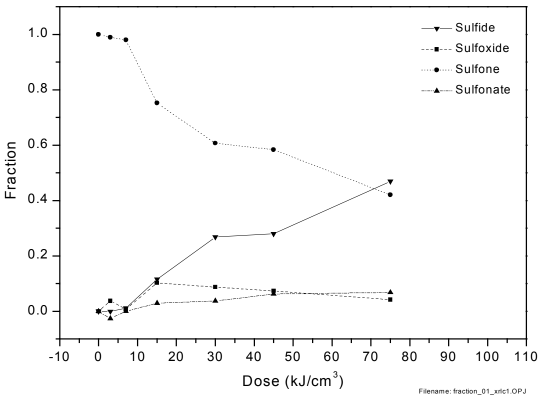

Figure 53. The radiation-induced production of sulfide, sulfoxide, sulfone, and sulfonate in fractions of total sulfur as function of surface dose. The PHS sample was exposed at the soft x-ray beamline (XRLC1).

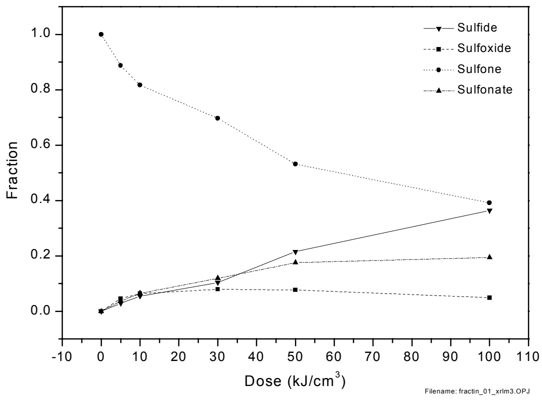

Figure 54. The radiation-induced production of sulfide, sulfoxide, sulfone, and sulfonate in fractions of total sulfur as function of surface dose. The PHS sample was exposed at the hard x-ray beamline (XRLM3).

It can be clearly observed in Figure 53 as well as in Figure 54 that there is a correlation between the surface dose deposited in the PHS sample and the fractional generation of radiation-induced sulfur functional groups, namely sulfide, sulfoxide, sulfone and sulfonate. However, the fractional generation of these sulfur species is not solely a function of the dose, but also depends on the incident spectral exposure distribution. This becomes apparent in Figure 55, in which the fractional radiation-induced production of the sulfide for the different incident spectral exposure distributions at XRLC1 and XRLM3 are depicted. The spectral exposure distributions of the soft x-ray beamline XRLC1 and the hard x-ray beamline XRLM3 are presented in Figure 56, indicating the position of the S K absorption edge at 2472 eV. It can be observed that most of the incident flux of the soft x-ray beamline XRLC1 is below the S K absorption edge, whereas in the case of the hard x-ray beamline XRLM3 most of the flux is above the S K absorption edge.

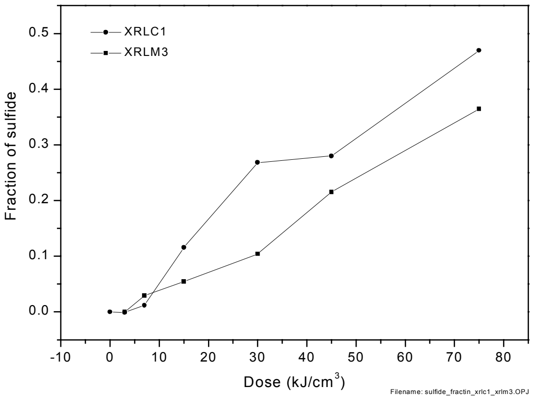

Figure 55. The fraction of sulfide as a function of surface dose in PHS for the soft x-ray exposure at XRLC1 (circle) and the hard x-ray exposure at XRLM3 (square).

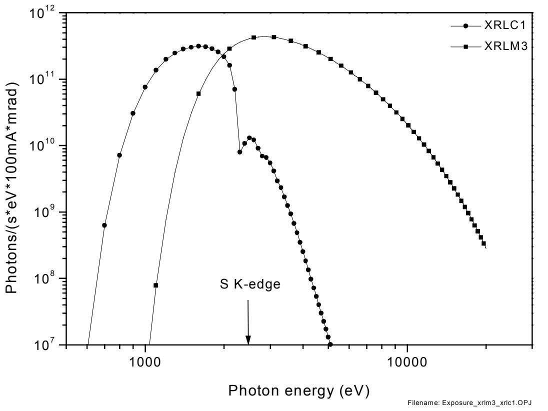

Figure 56. The incident spectral distributions of the soft x-ray beamline XRLC1 at 1.3 GeV (circle) and the hard x-ray beamline XRLM3 at 1.5 GeV (square), for which the PHS samples were exposed.

Thus, it can be concluded that the radiation-induced production of sulfur functional groups in PHS depends on the deposited dose as well as on the incident spectral distribution of the exposure.

For the application of PHS resist in deep x-ray lithography, it is necessary to gain an understanding of the radiation-induced degradation of the PHS and consequently, the production of the various sulfur species. The significance of the spectral incident photon flux will be emphasized through the fact that as the incident radiation penetrates through the PHS resists, the PHS itself acts as a filter and changes the incident spectral exposure distribution for subsequent layers. This effect is depicted in Figure 57.

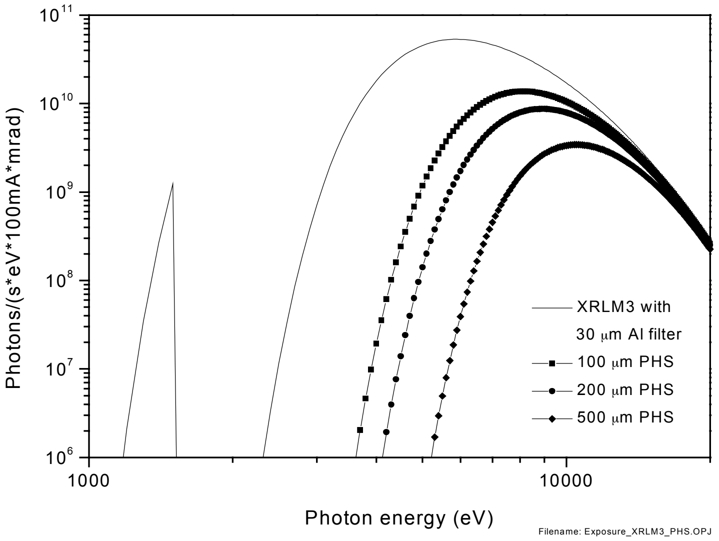

Figure 57. The effect of the energy dependent absorption of PHS, which leads to a change of the incident spectral distribution of exposure of subsequent PHS layers. The incident primary exposure spectrum of the XRLM3 beamline with a filter of 30 μm Al is shown, followed by the spectra in PHS at 100 μm, 200 μm, and 500 μm depth.

It can be seen in Figure 57 that as the radiation penetrates deeper in the PHS, the photon flux decreases and shifts to higher energy. Hence, the incident spectrum on the surface is very different from the spectrum at 500 μm depth. Consequently, the radiation-induced production of sulfur functional groups may change dramatically, necessitating the characterization of the changes in the sulfur functional groups as a function of PHS depth by spatially-resolved S K-edge XANES micro-spectroscopy.

To study the effect of different spectral exposure distributions on the PHS samples, filters with thickness' of 30 μm and 60 μm aluminum were used in the filter chamber during exposure. In each group the PHS samples were exposed with 2 different surface doses in the geometry shown in Figure 44 in section 6.2. The theoretical dose distribution as a function of depth was calculated using the program *CXrL* [90] and is shown in Figure 58 for all PHS samples.

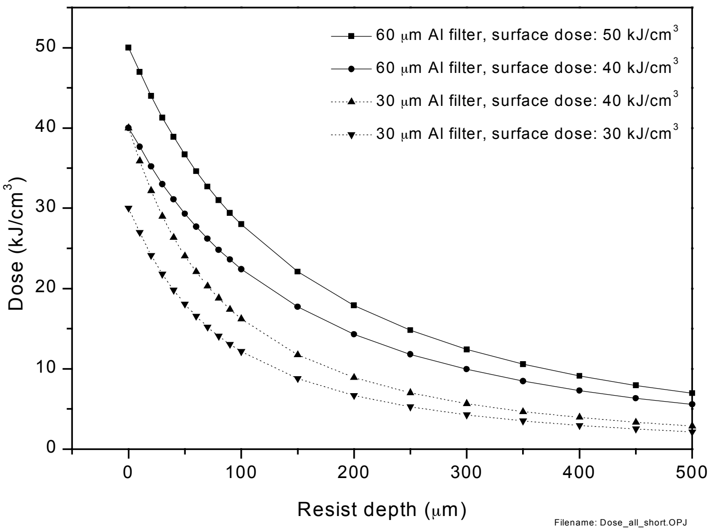

Figure 58. The calculated dose as a function of depth for the 2 PHS sample groups with Al filters of 60 μm (solid lines) and 30 μm (dotted lines). The surface doses are 50 kJ/cm^3 (square), 40 kJ/cm^3 (circle), 40 kJ/cm^3 (up triangle), and 30 kJ/cm^3 (down triangle).

The micro-spectroscopy data of the PHS samples are shown as surface plots in Figure 59, Figure 60, Figure 61, and Figure 62. The first sample group that was exposed with 50 kJ/cm^3 and 40 kJ/cm^3 using an 60 μm aluminum filter are presented in Figure 59, and Figure 60, respectively. The S K-edge XANES spectra were collected in the energy range of 2460 eV to 2520 eV. They are presented from just below the surfaces of the samples, which are indicated as 0 μm, to a depth of 550 μm. Once more, the first 3 absorption peaks, as previously labeled with 1, 2, and 3, can be identified as the presence of functional sulfide, sulfoxide, and sulfone groups, similarly to the initial identification, performed in Figure 49 and Figure 50. Peak number 4, representing the presence of a sulfonate functional group can hardly be observed.

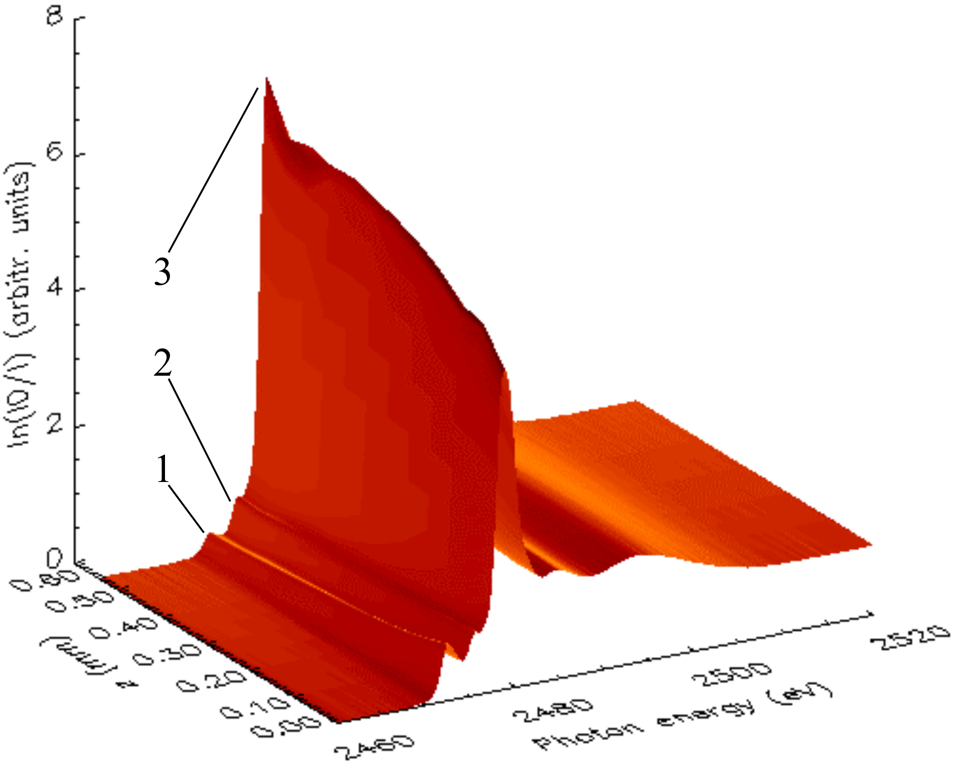

Figure 59. S K-edge micro-XANES spectrum of sample PHS_007, which was exposed with a surface dose of 50 kJ/cm^3 using a 60 µm aluminum filter.

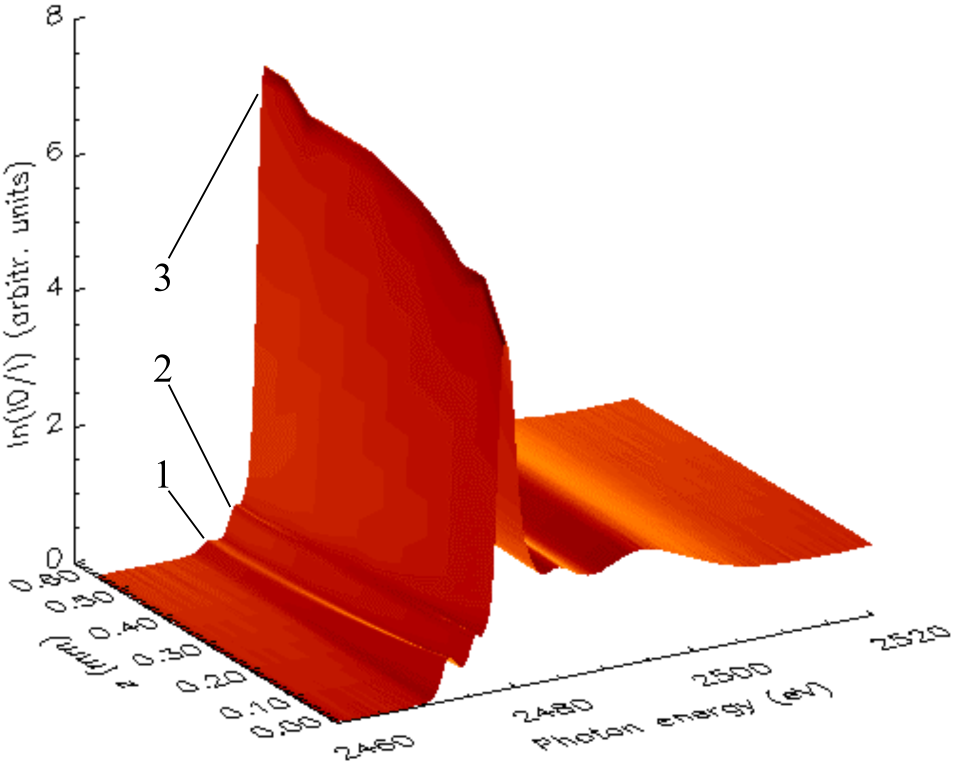

Figure 60. S K-edge micro-XANES spectrum of sample PHS_009, which was exposed with a surface dose of 40 kJ/cm^3 using a 60 µm aluminum filter.

Several qualitative observations can be established from the absorption peak heights of the sulfide, sulfoxide and sulfone functional groups in the S K-edge micro-XANES spectra in

Figure 59, and Figure 60. At first, the sulfide peak height decreases in both spectra with increasing depth and hence, decreasing dose (refer to Figure 58). Moreover, it can be seen that the sulfide peak height of the sample, having been exposed with a surface dose of 50 kJ/cm^3, is larger over the entire depth profile than the sample with a surface exposure of 40 kJ/cm^3. This agrees well with the general trend, shown in Figure 53 and Figure 55. The sulfone peak on the other hand increases with increasing depth or diminishing dose and also follows the previously shown general trends. The sulfoxide peak in both spectra seems to remain constant over the entire depth profile.

In Figure 61 and Figure 62, the S K-edge micro-XANES spectra of the second sample group using a 30 µm aluminum filter during exposure are presented. The spectra are presented in a spatial range of 0 µm, which is the surface, to 150 µm. This change of depth scale indicates the change to a softer exposure spectrum and the reduction of the surface doses to 40 kJ/cm^3 and 30 kJ/cm^3, respectively. In general, similar trends of the peaks representing the functional groups in Figure 61 and Figure 62 compared to the samples shown in Figure 59 and Figure 60 can be observed. The sulfide peaks, labeled 1, decrease with increasing depth or decreasing dose, whereas the sulfone peaks, labeled 3, increase. The sulfoxide peak, labeled 2, remains approximately constant over the entire depth range.

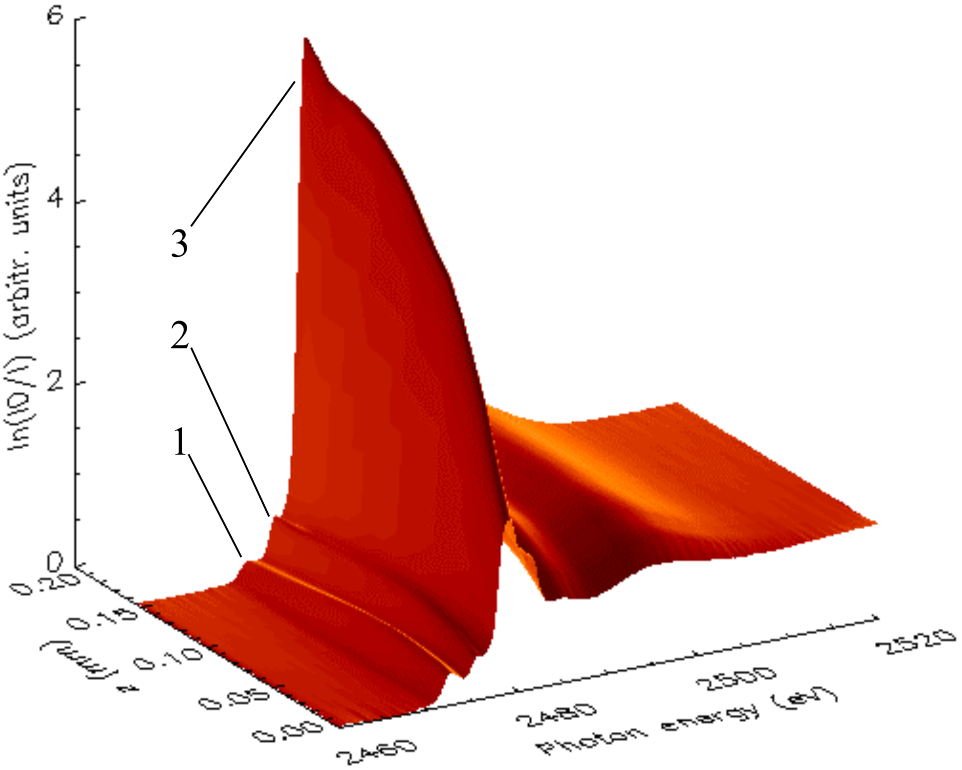

Figure 61. S K-edge micro-XANES spectrum of sample PHS_011, which was exposed with a surface dose of 40 kJ/cm^3 using a 30 µm aluminum filter.

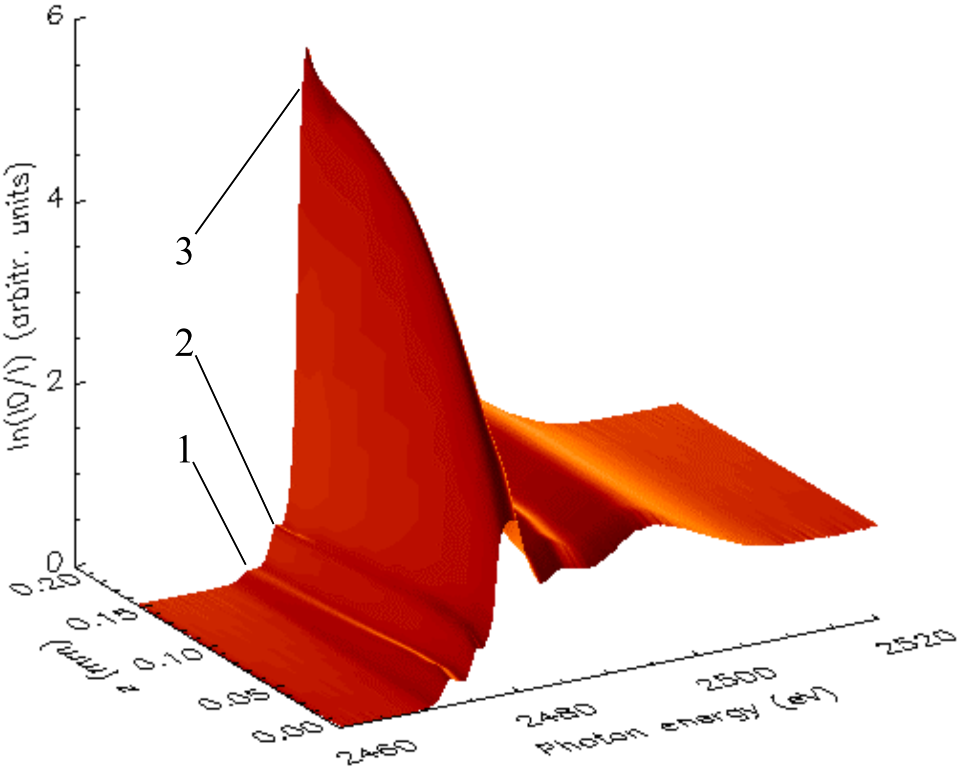

Figure 62. S K-edge micro-XANES spectrum of sample PHS_010, which was exposed with a surface dose of 30 kJ/cm^3 using a 30 µm aluminum filter.

Consequently, quantitative nonlinear least squares fitting of the S K-edge micro-XANES spectra was performed. As previously described, the data are fitted according to Eqn. (31) by using the reference compounds methionine sulfide, methionine sulfoxide, unexposed poly(hexadiene-1,3 sulfone), and poly(sodium 4-styrenesulfonate), respectively. Figure 63 and Figure 64 present a PHS sample (30 µm Al filter, 40 kJ/cm^3) as an example for the fractional distribution of sulfide, sulfoxide, sulfone and sulfonate as a function of depth and dose, respectively.

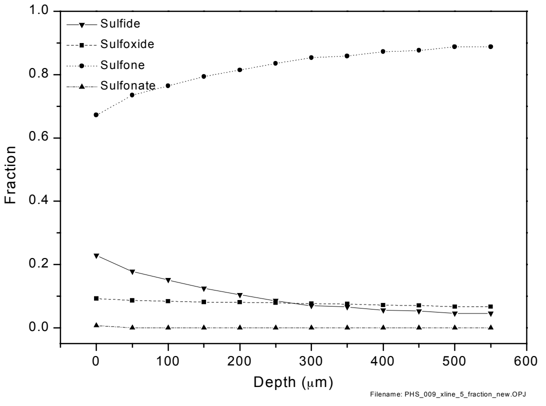

Figure 63. The fractions of sulfide (down triangle), sulfoxide (square), sulfone (circle), and sulfonate (up triangle) as a function of depth for a PHS sample with 30 µm Al filter and 40 kJ/cm^3.

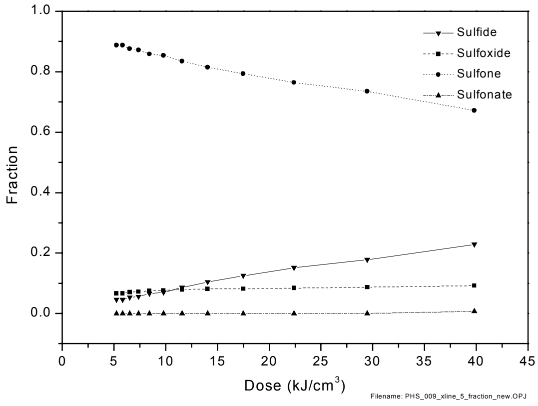

Figure 64. The fractions of sulfide (down triangle), sulfoxide (square), sulfone (circle), and sulfonate (up triangle) as a function of dose for a PHS sample with 30 µm Al filter and 40 kJ/cm^3.

The fractional distribution of the sulfide, sulfoxide and sulfone functional groups as a function of dose (refer to Figure 64) follows the general trend of the surface exposure data very closely (refer to Figure 54). The radiation-induced generation of sulfide is maximal at the surface of PHS, at which the highest dose is deposited. It decreases with increasing depth and decreasing dose, respectively. The behavior of the sulfone functional group is opposite to the sulfide. It is minimal at the surface due to a radiation-induced reduction to sulfide. It increases with increasing depth or diminishing dose. Thus, it is solely sulfone when reaching a depth at which only unexposed poly(hexadiene-1,3 sulfone) (PHS) is present. Interestingly, it seems that the sulfoxide reaches a type of equilibrium during radiation exposure in PHS, showing a constant fractional amount of ~ 10% independent of dose or spectral exposure distribution.

One would expect from the surface data in Figure 54 that the sulfonate peak would begin to appear in Figure 64 at a deposited dose of ~ 10 kJ/cm^3. This is not the case. In fact, the radiation-induced generation of sulfonate in PHS occurs only at the surface. This can be well observed in the high-resolution data shown in Figure 65. Here, the sulfonate peak, marked 4, is dominant at the surface, whereas the peaks of sulfide, sulfoxide and sulfone, labeled 1, 2, and 3, are suppressed. Within the initial 50 µm to 100 µm of the PHS sample, the sulfonate usually disappears entirely. This surface effect may be caused by oxidation during the exposure due to remaining oxygen in the exposure chamber. A more plausible explanation may be the surface oxidation of PHS after the exposure during sample preparation and measurement. Further work is needed to study this effect. Moreover, this surface oxidation effect of PHS shows clearly the value of the spatially-resolved S K-edge micro-XANES experiments, since standard XANES techniques are either surface or bulk sensitive, but can not provide both types of information.

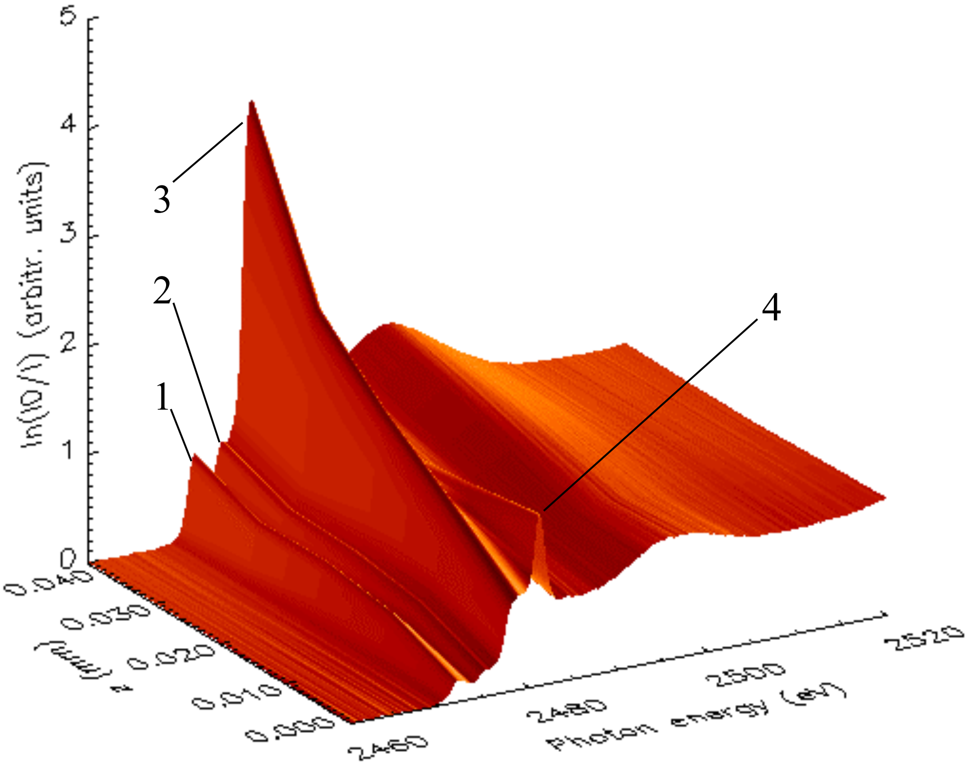

Figure 65. S K-edge micro-XANES spectra of a PHS sample very close to the PHS surface. The data were collected in a range of 40 µm with high-resolution (10µm). The strong presence of the sulfonate at the PHS surface can be seen, indicating the surface oxidation.

To be able to judge the influence of the deposited dose as well as of the incident spectral exposure distribution on the radiation-induced degradation process of PHS, the generation of the sulfide functional group was used as an example. Hence, the fractional distribution of sulfide in all samples is presented as function of depth in Figure 66.

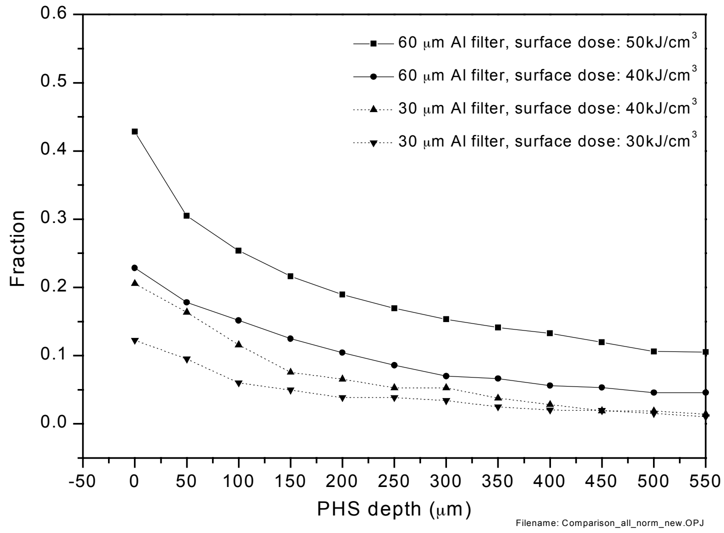

Figure 66. The fractional distribution of the sulfide in PHS as a function of depth for the 2 PHS sample groups with Al filters of 60 μm (solid lines) and 30 μm (dotted lines). The surface doses are 50 kJ/cm^3 (square), 40 kJ/cm^3 (circle), 40 kJ/cm^3 (up triangle), and 30 kJ/cm^3 (down triangle).

Two major trends can be established from Figure 66. First, a higher surface dose on the PHS sample, which coincides with being closer to the PHS surface, generates a larger amount of sulfide. This is the case for both samples in each group. As an example the sample group using a 60 μm aluminum filter is considered. In the PHS sample with a surface dose of 50 kJ/cm^3, on average ~ 103% more sulfide is generated compared to the sample, which was exposed with a surface dose of 40 kJ/cm^3. Secondly, the effect of the spectral exposure distribution on radiation-induced sulfide generation can also be observed in Figure 66. By looking at the slope of the sample group data sets (30 μm and 60 μm aluminum filter) and excluding the surface region, which is governed by the exponential decrease of dose, it can be noticed that the harder exposure distribution (60 μm aluminum filter) creates higher amounts of sulfide at larger depth. This effect can be particularly well observed for the samples with equal surface dose (40 kJ/cm^3) but different spectral exposure distributions.

Finally, it should be shown that it is possible to qualitatively image the spatial fractional distribution of the sulfide peak in the PHS by performing x-ray spectro-microscopy. In this technique, 2-D spatial images of the PHS sample are collected, in which the incident photon energy of the double crystal monochromator is set to the energy position of sulfide peak at 2472.5 eV and at the background at 2515 eV. The spatial change in absorption due to the change of the sulfide peak height is used as a contrast mechanism. As an example, the qualitative sulfide spectro-microscopy image of the PHS sample, which had been exposed with a 60 μm aluminum filter and a surface dose of 50 kJ/cm^3, is shown in Figure 67. The spatial range is 200 μm x 1000 μm (horizontal x vertical), in which the vertical axis z shows the depth profile and the deposited dose.

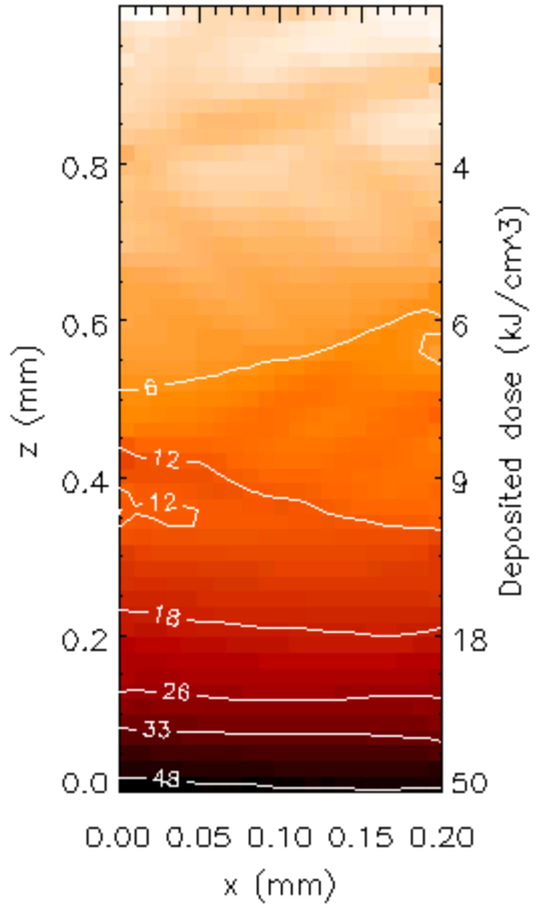

Figure 67. 2-D map of the PHS sample, which was exposed using 60 µm aluminum filter and a surface dose of 50 kJ/cm^3. The fractional distribution of sulfide is used to visualize the dose-depth distribution. Iso-dose lines are labeled with the deposited dose in kJ/cm^3 in the contour plot.

As a brief summary on the data analysis and the discussion in this chapter, the following facts can be established. It is possible to identify the sulfur functional groups, which are created by radiation-induced degradation of poly(hexadiene-1,3 sulfone) (PHS) by S K-edge XANES “fingerprinting”. The fingerprinting technique uses spectra of reference compounds and identifies the features in the sample spectrum based on energy shift and white line intensity. The comparison of the S K-edge XANES of PHS to reference spectra indicates that the sulfide, sulfoxide, and sulfonate are generated during radiation exposure.

The study of the surface samples indicated that there is correlation between the surface dose deposited in the PHS sample and the fractional generation of radiation-induced sulfur functional groups, namely sulfide, sulfoxide, sulfone and sulfonate. Furthermore, an effect of the incident spectral exposure distribution on the generated sulfur species could also be seen.

Spatially-resolved S K-edge XANES micro-spectroscopy was performed on poly(hexadiene-1,3 sulfone) (PHS) samples. The spectra were quantitatively analyzed by performing nonlinear least squares fits using reference spectra. The results indicate that the radiation-induced degradation and generation of the sulfide, sulfoxide, and sulfone is a function of depth and so implicitly a function of the deposited dose as seen in the surface samples. The spectral exposure distribution also has an impact on the generation of the sulfur functional groups. In general, it can be pointed out that the combination of a hard incident exposure distribution and a high surface dose generates a large amount of sulfide and conversely a small amount of sulfone.

Furthermore, it needs to be emphasized that micro-spectroscopy is able to acquire S K-edge XANES data from the surface of the PHS as well as the bulk. By applying micro-spectroscopy on the PHS samples it was established that the radiation-induced generation of sulfonate is limited to the surface region and can be associated with an surface oxidation effect. Below this surface region (< 50 µm), there is little generation of sulfonate, even at high dose levels. This observation could not be made without the ability to perform spatially-resolved XANES measurements.

8 Summary

The main intent of this work was to perform a spatially-resolved study of the radiation-induced degradation of poly(hexadiene-1,3 sulfone) (PHS) at the sulfur K absorption edge (2472 eV) using monochromatic radiation to perform x-ray absorption near structure (XANES) spectroscopy. In addition, it was necessary to provide the ability to conduct spatially-resolved x-ray fluorescence mapping using white synchrotron radiation. These two factors led to the current design and installation of the CAMD/ANL beamline and the microprobe end-station. The installation and qualification of hardware and software included the following key items:

- The Laboratório Nacional de Luz Síncrotron (LNLS) double crystal monochromator was successfully installed in the CAMD/ANL beamline, which provides monochromatic radiation at lower photon energies to perform x-ray absorption near-edge structure (XANES) spectroscopy. Due to its mechanical design, it is also possible to provide white synchrotron radiation to the microprobe end-station. In addition, some mechanical modifications were implemented, which enable the user to easily change monochromator crystals as well as perform alignment procedures remotely, which is often a necessity at low photon energies.
- An achromatic Kirkpatrick-Baez mirror focusing system that is able to focus white as well as monochromatic radiation and that allows working at large grazing angles (up to 15 mrad) was built and successfully installed in the microprobe end-station.
- A kinematic table was implemented in the set-up. It vertically moves the entire microprobe end-station when switching from white to monochromatic light. Experimental tests demonstrated a good vertical reproducibility of ~ 200 μm.
- A helium enclosure containing the entire end-station with the Kirkpatrick-Baez focusing system, the sample stage and the x-ray detectors was built and successfully implemented. When the enclosure is purged with helium, x-ray absorption near-edge structure (XANES) spectroscopy can be conducted in transmission or fluorescence at lower photon energies (e.g. at the sulfur K-edge XANES spectroscopy at 2472 eV).
- A new graphical user interface (GUI) for the beamline control and the data acquisition was written and implemented.

First experimental results on the performance of the Kirkpatrick-Baez focusing system combined with detailed ray-tracing calculations considering the CAMD bending magnet source size, the beamline, and measured slope errors of the x-ray mirrors led to the following conclusions.

- The horizontal and vertical focal spot size σ_{xF}, σ_{zF} obtained by performing knife-edge scans are 18.8 μm and 7.0 μm, respectively.
- It was established that neither the measured slope errors nor the roughness of the x-ray mirrors has a significant effect on the experimental focal spot size. Hence, inexpensive float glass mirrors proved to be very effective in the CAMD/ANL beamline and microprobe end-station.
- It was, however, shown that the experimental horizontal and vertical focal spot size deviate about ~ 50% from the theoretical values, suggesting that the horizontal and

vertical bending magnet source sizes are actually larger than the interpolated theoretical source sizes.

- The measured focused photon flux within the spectral bandwidth as determined by the double crystal monochromator at the sample position in the low photon energy range of 2500 eV to 6000 eV was established to ~ $1*10^8$ photons per second per 100 mA.

The successful implementation of the hardware and software at the CAMD/ANL beamline provided the ability to perform x-ray spectro-microscopy in the low energy region. This permitted the extent of the initial surface sensitive study of radiation-induced degradation of poly(hexadiene-1,3 sulfone) to spatially investigate the generation of sulfur functional groups in PHS as a function of depth. From the S K-edge XANES micro-spectroscopy experiments and the subsequent quantitative data analysis performing nonlinear least squares fits, the following results can be summarized:

- Using S K-edge XANES fingerprinting, the radiation-induced degradation and generation of sulfur functional groups, namely sulfide, sulfoxide, sulfone, and sulfonate were established.
- The quantitative analysis of surface sensitive S K-edge XANES spectra showed a qualitative correlation between the fractional generation of the sulfide, sulfoxide, sulfone, and sulfonate and the deposited dose as well as the incident spectral exposure distribution.
- The quantitative analysis of the spatially-resolved S K-edge XANES micro-spectroscopy data showed a correlation between the fractional distribution of sulfide, sulfoxide, and sulfone and the depth in poly(hexadiene-1,3 sulfone) (PHS). This trend was related with the deposited dose as a function of depth and thus is in good agreement with the surface data. The impact of the harder incident spectral exposure distribution was associated with a larger amount of radiation-induced generation of sulfide.
- It was shown that the radiation-induced production of highly oxidized sulfur species, namely sulfonate in poly(hexadiene-1,3 sulfone) is limited to the surface region and can be associated with an surface oxidation effect. Below this surface region (< 50 μm), there is little generation of sulfonate, even at high dose levels. It needs to be emphasized that this observation could not be made without the ability to perform spatially-resolved XANES measurements, which is able to provide S K-edge XANES data from the surface as well as the bulk.

To the author's knowledge, this is the first reported work on spatially-resolved micro-spectroscopy in the energy region of 2000 eV to 4000 eV, presenting the example of S K-edge micro-XANES on a potential x-ray resist, poly(hexadiene-1,3 sulfone).

Appendix

List of Figures

List of Tables

List of Symbols

α	the angular slit size (FWHM)
α_1	the angle of incidence in Snell's law
α_2	the angle of refraction in Snell's law
a	the major axis of the ellipse
A_i	the atomic weight of the element i in units of ^{12}C
A_{Slope}	the amplitude of the slope error in µm for the input in *Shadow*
β	the absorption index decrement or extinction coefficient
b	the minor axis of the ellipse
c	the speed of light, $c=2.998\cdot10^8$ m/s
c_i	the fraction of reference compound i in the S K-edge XANES spectrum
C	the polarization factor
C(Z)	Victoreen parameter
δ	the refractive index decrement
d	d-spacing of the crystal
d_i	the interatomic distance in a material
d_t	thickness of the sample
D(R)	the optical transfer function (OTF)
D(Z)	Victoreen parameter
e	the eccentricity of the ellipse, distance between the center to either focal point
$e^{-M\cdot k^2}$	the Debye-Waller factor
ΔE	the energy resolution of the double crystal monochromator
ΔE_i	the relative energy shift of the reference compound's XANES spectrum
E_{Photon}	the photon energy of the monochromatic x-ray beam in eV
E	the energy of the storage ring in GeV
Φ_{ij}	the phase shift
f_1	the distance from the source to the center of the mirror
f_2	the distance from the center mirror to the focal point
f_{1H}	the distance from the source to the center of the horizontal mirror
f_{2H}	the distance from the center of the horizontal mirror to the focal point
f_{1V}	the distance from the source to the center of the vertical mirror
f_{2V}	the distance from the center of the vertical mirror to the focal point
f_{1S}	the real part of the atomic scattering factor
F_1	the source point
F_{1F}	the force F_{1F} to apply the first bending moment to the KB-mirror
F_2	the focal point
F_{2F}	the force F_{2F} to apply the second bending moment to the KB-mirror
F_h	crystal structure factor

$F_j(k)$	the backscattering amplitude
γ	gamma of the CAMD storage ring, γ=2544.1 at 1.3GeV
i	complex number with $i^2 = -1$
I_0	the initial intensity of the incident monochromatic x-ray beam
I	the transmitted intensity of the monochromatic x-ray beam
I_{Diode}	the photo-diode current in A
I_{Ion}	the ion chamber current in A
I_{Ring}	the storage ring current in mA
λ	the wavelength of the incident monochromatic x-ray beam
λ_c	the critical wavelength of the CAMD storage ring, λ_c=7.45 Å at 1.3GeV
λ_e	the wavelength of the ejected photoelectron
λ_j	the electron mean free path
λ_{Slope}	the wavelength of the slope error ripple in cm for the input in *Shadow*
l	the length of the KB-mirror, l=100 mm
L	the distance from the source to the slit
μ	the linear absorption coefficient
$\mu_{Reference,i}$	the S K-edge XANES spectrum of the reference compound i for the nonlinear least squares fit
μ_{Sample}	the S K-edge XANES spectrum of the sample for the nonlinear least squares fit
M	the modulation
M_D	the demagnification
M_{DH}	the demagnification of the horizontal mirror, $M_{DH}=f_{1H}/f_{2H}\sim 61$
M_{DV}	the demagnification of the vertical mirror, $M_{DV}=f_{1V}/f_{2V}\sim 35$
n	an integer number
n_1	the refractive index of air
n_2	the refractive index of the material, of which total external reflection occurs
N_A	the Avogadro number, $N_A=6.023\cdot 10^{23}$ mol^{-1}
N_j	the number of atoms in the *j*th shell
π	pi with 3.142
$\Delta\theta$	the angular spread of the reflected x-ray beam
$\Delta\theta_c$	the intrinsic rocking curve width (FWHM) of the monochromator crystal
θ_B	the Bragg angle in degree
θ_{crit}	the critical angle, defined as the angle, at which total external reflection occurs
θ_{graz}	the grazing angle, defined as the angle between the mirror surface and the incident beam
θ_{inc}	the incident angle, defined as the angle between the incident beam and the surface normal of the mirror
θ_{SR}	the angular spread of the incident synchrotron beam
$\theta(R)$	the phase transfer function (PTF)
QE	the quantum efficiency of the photo-diode in %
ρ_i	the density of the element i in g/cm^3

r_0	the classical electron radius, $r_0 = e^2/(mc^2) = 2.818\cdot10^{-15}$ m
r_j	the distance to the *j*th shell
R(m)	the CAMD bending magnet radius in m, R=2.928m
σ_e	the Klein-Nishina scattering coefficient
σ_R	the rms angular divergence of the synchrotron light emitted by a single electron
σ_{Rough}	the rms surface roughness
σ_{Slope}	the integrated rms slope error budget
$\sigma_{Slope,h}$	the rms slope error of the horizontal mirror
$\sigma_{Slope,v}$	the rms slope error of the vertical mirror
σ_x	the CAMD horizontal source size (rms)
σ_z	the CAMD vertical source size (rms)
$\sigma_{z'}$	the CAMD angular divergence of the vertical source size (rms)
$\sigma_{Z'}$	the CAMD vertical photon beam divergence (rms)
σ_{xF}	the rms horizontal focal point size
σ_{zF}	the rms vertical focal point size
s	the vertical entrance slit width
$S_i(k)$	the amplitude reduction factor due to many-body effects at the central atom
τ	the photoionization cross section or photoelectric cross section
T(R)	the modulation transfer function (MTF)
V	the unit-cell volume of the crystal
V_F	interatomic potential at the Fermi level
ω	the single crystal rocking curve width (FWHM)

References

[1] J. A. Moore, J. O. Choi, “Degradation of Poly(methyl methacrylate) Deep UV, X-Ray, Electron Beam, and Proton-Beam Irradiation,” in *American Chemical Society Symposium Series: Radiation Effects on Polymers,* Vol. 475, edited by R. L. Clough, S. W. Shalaby, American Chemical Society, Washington D.C., (1991).

[2] B. W. Yates, D. M. Shinozaki, A. Kumar, W. J. Meath, “The Absorption Coefficient Spectrum of Poly(methyl methacrylate) in the Soft X-Ray Region,” Journal of Polymer Science: Part B: Polymer Physics **30**, 185, (1992).

[3] O. Wollersheim, H. Zumaqué, J. Hormes, J. Langen, P. Hoessel, L. Häussling, G. Hoffmann, “Radiation chemistry of poly(lactides) as a new polymer resists for the LIGA process,” Journal of Micromechanics and Microengineering **4**, 83, (1994).

[4] O. Wollersheim, H. Zumaqué, J. Hormes, D. Kadereit, J. Langen, L. Häussling, P. Hoessel, G. Hoffmann, “Quantitative studies of the radiation chemical behaviour of PMMA and poly(lactides),” Nuclear Instruments and Methods in Physics Research B **97**, 273, (1995).

[5] J. Davies, “Synthesis of UV/X-Ray Sensitive Polymers and Their applications as Resists,” Ph.D. Thesis, Louisiana State University, (1996).

[6] R. Chauvistré, “Röntgenabsorptionsspektroskopie an der Schwefel K-Kante als Methode zur Strukturaufklärung von vulkanisiertem Kautschuk,” Ph.D. Thesis, University Bonn, (1992).

[7] T. A. Smith, J. G. DeWitt, B. Hedman, K. O. Hodgson, “Sulfur and Chlorine K-Edge Absorption Spectroscopic Studies of Photographic Materials,” Journal of the American Chemical Society **116**, 3836, (1994).

[8] A. Rompel, R. M. Cinco, M. J. Latimer, A. E. McDermott, R. D. Guiles, A. Quintanilha, R. M. Krauss, K. Sauer, V. K. Yachandra, M. P. Klein, “Sulfur K-edge x-ray absorption spectroscopy: A spectroscopic tool to examine the redox state of S-containing metabolites in vivo,” Proceedings of the National Academy of Science of the United States of America **95** (11), 6122, (1998).

[9] R. Chauvistré, J. Hormes, E. Hartmann, N. Etzenbach, R. Hosch, J. Hahn, “Sulfur K-shell photoabsorption spectroscopy of the sulfanes R- Sn-R, n=2-4,” Chemical Physics **223** (2-3), 293, (1997).

[10] G. S. Waldo, R. M. K. Carlson, J. M. Moldowan, K. E. Peters, J. E. Penner-Hahn, “Sulfur speciation in heavy petroleums: Information from X-ray absorption near-edge structure,” Geochimica et Cosmochimica Acta **55** (3), 801, (1991).

[11] M. L. Gorbaty, G. N. George, S. R. Kelemen, “Direct determination and quantification of sulfur forms in heavy petroleum and coal. Sulfur K-edge x-ray absorption and x-ray photoelectron spectroscopic approaches,” in *American Chemical Society Symposium Series: Coal Science II,* Vol. 461, pp. 127, edited by H. H. Schobert, K. D. Bartle, L. J. Lynch, American Chemical Society, Washington D.C., (1991).

[12] G. P. Huffman, N. Shah, F. E. Huggins, L. M. Stock, K. Chatterjee, J. J. Kilbane, M. M. Chou, D. H. Buchanan, “Sulfur speciation of desulfurized coals by XANES spectroscopy,” Fuel **74** (4), 549, (1995).

[13] M. A. Vairavamurthy, D. Maletic, S. Wang, B. Manowitz, T. Eglinton, T. Lyons, “Characterization of sulfur-containing functional groups in sedimentary humic substances by x-ray absorption near-edge structure spectroscopy,” Energy & Fuels **11** (3), 546, (1997).

[14] H. Modrow, G. Calderon, W. H. Daly, G. G. B. d. Souza, R. C. Tittsworth, N. Mölders, P. J. Schilling, “Radiation-induced degradation of polydiene sulfones as obtained by sulfur K-edge XANES,” to be published in Journal of Synchrotron Radiation, (1998).

[15] P. J. Eng, M. Newville, M. L. Rivers, S. R. Sutton, “Dynamically Figured Kirkpatrick-Baez X-Ray Micro-Focusing Optics,” to be published in SPIE, (1998).

[16] Z. Cai, W. Yun, S. T. Pratt, R. M. Miller, E. Gluskin, D. B. Hunter, A. G. Jarstfer, K. M. Kemmer, B. Lai, H. R. Lee, D. G. Legnini, W. Rodrigues, C. I. Smith, “X-ray imaging & microspectroscopy of mycorrhizal fungus-plant symbiosis,” Advanced Photon Source Research **1** (1), 15, (1998).

[17] D. H. Bilderback, “Overview talk on glass capillary optics,” presented at the first international developers workshop on glass capillary optics for x-ray microbeam applications, Ithaca/New York, (1996).

[18] I. Snigireva, A. Souvorov, A. Snigirev, “Bragg-Fresnel Optics for High-Energy X-Ray Microscopy Techniques at the ESRF,” in *X-Ray Microscopy and Spectromicroscopy,* edited by J. Thieme, G. Schmahl, D. Rudolph, et al., Springer, Berlin, (1998).

[19] J. Maser, C. Jacobsen, J. Kirz, A. Osanna, S. Spector, S. Wang, J. Warnking, “Development of a Cryo Scanning Transmission x-ray microscope at NSLS,” in *X-Ray Microscopy and Spectromicroscopy,* edited by J. Thieme, G. Schmahl, D. Rudolph, et al., Springer, Berlin, (1998).

[20] J. A. Victoreen, “Probable x-ray mass absorption coefficients for wave-lengths shorter than the K critical absorption wave-length,” Journal of Applied Physics **14** (2), 95, (1943).

[21] J. A. Victoreen, “The absorption of incident quanta by atoms as defined by the mass photoelectric absorption coefficient and the mass scattering coefficient,” Journal of Applied Physics **19** (9), 855, (1948).

[22] R. Chauvistré, J. Hormes, “Structural analysis of sulfur in rubber by x-ray near-edge absorption spectroscopy (XANES),” Kautschuk & Gummi Kunststoffe **45** (10), 808, (1992).

[23] W. Kossel, “Zum Bau der Röntgenspektren,” Zeitschrift für Physik **1**, 119, (1920).

[24] R. d. L. Kronig, “Zur Theorie der Feinstruktur in den Röntgenabsorptionsspektren,” Zeitschrift für Physik **70**, 317, (1931).

[25] C. R. Natoli, in *EXAFS and Near-edge Structure III,* pp. 38, edited by K. O. Hodgson, Springer, New York, (1984).

[26] D. E. Sayers, E. A. Stern, F. W. Lytle, “New technique for investigating noncrystalline structures: Fourier Analysis of extended x-ray-absorption fine structure,” Physical Review Letters **27** (18), 1204, (1971).

[27] E. A. Stern, “Theory of extended x-ray absorption fine structure,” Physical Review B **10** (8), 3027, (1974).

[28] F. W. Lytle, D. E. Sayers, E. A. Stern, "The history and modern practice of EXAFS spectroscopy," in *Advances in X-ray spectroscopy,* pp. 267, edited by C. Bonnelle, C. Mande, Pergamon Press, Oxford, (1982).

[29] G. E. Brown, G. Calas, G. A. Waychunas, J. Petiau, "X-ray absorption spectroscopy and its applications in mineralogy and geochemistry," in *Spectroscopic Methods in Mineralogy and Geology,* Vol. 18, pp. 431, edited by F. R. Hawthrone, Mineralogical Society of America, Washington D.C., (1988).

[30] P. A. Lee, J. B. Pendry, "Theory of x-ray absorption fine structure," Physical Review B **11** (8), 2795, (1975).

[31] J. Wong, "Extended x-ray absorption fine structure: a modern structural tool in materials science," Materials Science and Engineering **80**, 107, (1986).

[32] A. P. Hitchcock, M. Tronc, "Ionization current detection of soft x-ray photoabsorption: sulfur and chlorine K-shell spectra of SO_2F_2FCl and SO_2Cl_2," Chemical Physics **121**, 265, (1988).

[33] N. Kosugi, "Theory and analysis of XANES: MO approach," in *X-ray absorption fine structure for catalysts and surfaces,* Vol. 2, pp. 60, edited by Y. Iwasawa, World Scientific, Tokyo, (1996).

[34] T. Fujikawa, "Theory and analysis of XANES: Multiple scattering approach," in *X-ray absorption fine structure for catalysts and surfaces,* Vol. 2, pp. 77, edited by Y. Iwasawa, World Scientific, Tokyo, (1996).

[35] C. L. Spiro, J. Wong, F. W. Lytle, R. B. Greegor, D. H. Maylotte, S. H. Lamson, "X-ray spectroscopic investigation of sulfur sites in coal: Organic sulfur identification," Science **226**, 48, (1984).

[36] M. M. Taghiei, F. E. Huggins, N. Shah, G. P. Huffman, "In Situ X-Ray Absorption Fine Structure Spectroscopy Investigation of Sulfur Functional Groups in Coal during Pyrolysis and Oxidation," Energy & Fuels **6** (3), 293, (1992).

[37] W. H. Calkins, R. J. Torres-Ordonez, B. Jung, "Comparison of pyrolytic and x-ray spectroscopic methods for determining organic sulfur species in coal," Energy & Fuels **6** (4), 411, (1992).

[38] X. Q. Yang, K. H. Xue, H. S. Lee, J. McBreen, T. A. Skotheim, F. Lu, "X-ray absorption studies of organosulfide redox polymeric electrodes," Physical Review B **45** (10), 5733, (1992).

[39] T. A. Skotheim, X. Q. Yang, K. H. Xue, H. S. Lee, J. McBreen, F. Lu, "X-ray absorption studies on organo-disulfide redox cathodes," Electrochimica Acta **37** (9), 1635, (1992).

[40] A. Vairavamurthy, W. Q. Zhou, T. Eglinton, B. Manowitz, "Sulfonates: A novel class of organic sulfur compounds in marine sediments," Geochimica et Cosmochinica Acta **58** (21), 4681, (1994).

[41] F. R. Elder, R. V. Langmuir, H. D. Pollock, "Radiation from Electrons Accelerated in a Synchrotron," Physical Review **74** (1), 52, (1948).

[42] E. E. Koch, D. E. Eastman, Y. Farge, "Synchrotron radiation - a powerful tool in science," in *Handbook on Synchrotron Radiation,* Vol. 1a, edited by E. E. Koch, North-Holland Publishing Company, New York, (1983).

[43] R. L. Stockbauer, P. Ajmera, E. D. Poliakoff, B. C. Craft, V. Saile, “A new synchrotron light source at Louisiana State University's Center for Advanced Microstructures and Devices,” Nuclear Instruments and Methods in Physics Research A **291**, 505, (1990).

[44] M. C. Corrêa, H. Tolentino, A. Craievich, C. Cusatis, “A two-crystal monochromator for the UVX ring of LNLS,” Review of Scientific Instruments **63** (1), 896, (1992).

[45] J. A. Golovchenko, R. A. Levesque, P. L. Cowan, “X-ray monochromator system for the use with synchrotron radiation sources,” Review of Scientific Instruments **52** (4), 509, (1981).

[46] S. M. Heald, “EXAFS with synchrotron radiation,” in *X-Ray Absorption Principles, Applications, Techniques of EXAFS, SEXAFS and XANES,* pp. 144, edited by D. C. Koninsberger, R. Prins, John Wiley & Sons, New York, (1988).

[47] T. Masushita, H. Hashizume, “X-ray Monochromators,” in *Handbook on Synchrotron Radiation,* Vol. 1a, pp. 261, edited by E. E. Koch, North-Holland Publishing Company, New York, (1983).

[48] C. Welnak, G. J. Chen, F. Cerrina, “SHADOW: a synchrotron radiation and X-ray optics simulation tool,” Nuclear Instruments and Methods in Physics Research A **347**, 344, (1994).

[49] D. Mills, V. Pollock, “Stabilizing feedback system for synchrotron radiation monochromators,” Review of Scientific Instruments **51** (12), 1664, (1980).

[50] Z. Hussain, E. Umbach, D. A. Shirley, J. Stöhr, J. Feldhaus, “Performance and application of a double crystal monochromator in the energy region 800eV<hν<4500eV,” Nuclear Instruments & Methods in Physics Research A **195**, 119, (1982).

[51] S. Krinsky, M. L. Perlman, R. E. Watson, “Characteristics of Synchrotron Radiation and of its Sources,” in *Handbook of Synchrotron Radiation,* Vol. 1a, pp. 127, edited by E. E. Koch, North-Holland Publishing Company, New York, (1983).

[52] S. Brennan, personal communication, (1998).

[53] B. L. Henke, E. M. Gullikson, J. C. Davis, “X-ray interactions: photoabsorption, scattering, transmission, and reflection at E=50-30000 eV, Z=1-92,” Atomic Data and Nuclear Data Tables **54** (2), 181, (1993).

[54] E. M. Gullikson, "X-ray Interactions with Matter," world wide web at http://www-cxro.lbl.gov/optical_constants/, (1998).

[55] G. P. Williams, “Electron Binding Energies,” in *X-ray Data Booklet,* edited by J. Kirz, D. T. Attwood, B. L. Henke, et al., Lawrence Berkley Laboratory, Berkley, (1986).

[56] P. Schilling, E. Morikawa, H. Tolentino, E. Tamura, R. L. Kurtz, C. Cusatis, “Installation and operation of the LNLS double-crystal monochromator at CAMD,” Review of Scientific Instruments **66** (2), 2214, (1995).

[57] M. L. Rivers, “X-Ray Fluorescence Imaging with Synchrotron Radiation,” in *X-Ray Microscopy II,* pp. 233, edited by D. A. Sayre, M. Howells, J. Kirz, et al., Springer, New York, (1987).

[58] N. Mölders, P. Schilling, A. Moewes, M. C. Petri, L. Leibowitz, H. O. Moser, “Development of a Hard X-Ray Microprobe at CAMD,” in *X-Ray Microscopy and*

Spectromicroscopy, edited by J. Thieme, G. Schmahl, D. Rudolph, et al., Springer, Berlin, (1998).

[59] C. J. Sparks, “Synchrotron Radiation Research,” in *Synchrotron Radiation Research,* pp. 459, edited by H. Winick, S. Doniach, Plenum Press, New York, (1980).

[60] LeCroy-Corporation, "Modular Standards," world wide web at http://www.lecroy.com/lrs/, (1998).

[61] J. M. Schoonmaker, N. Mölders, “Instrumental set-up and data acquisition at the ANL/CAMD beamline,” to be published in the Center for Advanced Microstructures and Devices (CAMD), Baton Rouge, (1998).

[62] P. Kirkpatrick, A. Baez, “Formation of Optical Images by X-Rays,” Journal of the Optical Society of America **38** (9), 766, (1948).

[63] B. X. Yang, M. L. Rivers, W. Schildkamp, P. J. Eng, “GeoCARS microfocusing Kirkpatrick-Baez mirror bender development,” Review of Scientific Instruments **66** (2), 2278, (1995).

[64] B. X. Yang, "On Forming High Precision, Curved Optical Surfaces via Elastic Bending," internal report at GSECARS/University of Chicago, Chicago (1993).

[65] J. B. West, H. A. Padmore, “Optical Engineering,” in *Handbook on Synchrotron Radiation,* Vol. 2, pp. 21, edited by G. V. Marr, North-Holland Publishing Company, New York, (1987).

[66] U. Jarecki, H. J. Schulz, “Mathematics,” in *Dubble,* edited by W. Beitz, K. H. Küttner, Springer, Berlin, (1987).

[67] E. Hecht, A. Zajac, *Optics*, 2 ed., Addison-Wesley Publishing Company, Reading, (1990).

[68] E. Morikawa, "CAMD Synchrotron Light Source by SHADOW," internal report at the Center for Advanced Microstructures and Devices (CAMD), Baton Rouge (1989).

[69] P. J. Eng, "Request for Quotes for an Internally Cooled Silicon 900 mm Long Vertical Focusing Mirror: Focusing X-Rays from the Advanced Photon Source Undulator "A"," internal report at GSECARS/University of Chicago, Chicago (1996).

[70] P. Z. Takacs, S. Qian, Patent of the United States of America, No. 4884697, (1989).

[71] P. Z. Takacs, S. K. Feng, E. L. Church, S. Qian, W. Liu, “Long trace profile measurements on cylindrical aspheres,” presented at the Advances in Fabrication and Metrology for Optics and Large Optics, (1989).

[72] S. C. Irick, W. R. McKinney, D. L. J. Lunt, P. Z. Takacs, “Using a straightness reference in obtaining more accurate surface profiles from a long trace profiler,” Review of Scientific Instruments **63** (1), 1436, (1992).

[73] S. C. Irick, “Determining surface profile from sequential interference patterns from a long trace profiler,” Review of Scientific Instruments **63** (1), 1432, (1992).

[74] P. Z. Takacs, C. J. Bresloff, “Significant improvements in long trace profiler measurements performance,” presented at the Optics for High-Brightness Synchrotron Radiation Beamlines II, Denver, (1996).

[75] B. L. Henke, “Scattering factors and mass absorption coefficients,” in *X-ray Data Booklet,* pp. 2.28, edited by J. Kirz, D. T. Attwood, B. L. Henke, et al., Lawrence Berkley Laboratory, Berkley, (1986).

[76] D. L. Windt, W. K. Waskiewicz, J. E. Griffith, “Surface finish requirements for soft x-ray mirrors,” Applied Optics **33**, 2025, (1994).

[77] L. Névot, P. Croce, “Charactérisation des surfaces par réflexion rasante de rayons X. Application à l'étude du polissage de quelques verres silicates,” Revue de Physique Appliquée **15**, 761, (1980).

[78] E. Spiller, *Soft X-Ray Optics*, 1 ed., SPIE Optical Engineering Press, Bellingham, (1994).

[79] P. Kirkpatrick, A. Baez, A. Newell, “Geometrical optics of grazing incidence reflectors,” Physical Review **73**, 535, (1948).

[80] H. Ebert, *Physikalisches Taschenbuch*, 5th ed., Vieweg, Braunschweig, (1978).

[81] D. Kühlke, *Optik: Grundlagen und Anwendungen*, 1 ed., Verlag Harri Deutsch, Frankfurt/Main, (1998).

[82] H. Manohara, personal communication, (1998).

[83] A. Moewes, personal communication, (1998).

[84] Y. Vladimirsky, K. Morris, J. M. Klopf, O. Vladimirsky, V. Saile, “X-ray Micro-Lithography Exposure System for High Aspect Ratio Micromachining,” presented at the Microlithography and Metrology in Micromachining, Austin, (1995).

[85] G. Tourillon, E. Dartyge, A. Fontaine, M. Lemonnier, F. Bartol, “Electron yield x-ray absorption spectroscopy at atmospheric pressure,” Physics Letters A **121** (5), 251, (1987).

[86] K. H. Sze, C. E. Brion, M. Tronc, S. Bodeur, A. P. Hitchcock, “Inner and valence shell excitation of dimethyl sulfoxide by electron energy loss and photoabsorption spectroscopies,” Chemical Physics **121**, 279, (1988).

[87] A. P. Hitchcock, S. Bodeur, M. Tronc, “Sulfur and chlorine K-shell spectra of gases,” Physica B **158**, 257, (1989).

[88] C. Dezarnaud, M. Tronc, A. P. Hitchcock, “Inner shell spectroscopy of the carbon-sulfur bond,” Chemical Physics **142**, 455, (1990).

[89] T. Ressler, "WinXAS 97," (1997).

[90] M. Khan, F. Cerrina, "CXrL Toolset User Guide," internal report at the University of Wisconsin, Madison (1996).